A matter of brightness: table-top X-ray generation inside waveguides and X-ray holography with single free-electron laser pulses

DISSERTATION

for the award of the degree
”Doctor rerum naturalium” (Dr. rer. nat.)
of the Georg-August University Göttingen
within the doctoral program
Prophys
of the Georg-August University School of Science (GAUSS)

submitted by

Malte Julian Udo Vaßholz

from Mettingen

Göttingen, 2021

Thesis Committee

Prof. Dr. Tim Salditt, Institute for X-Ray Physics, Georg-August University, Göttingen

Prof. Dr. Claus Ropers, IV. Institute of Physics, Georg-August University, Göttingen

Members of the Examination Board

First Reviewer: **Prof. Dr. Tim Salditt**, Institute for X-Ray Physics, Georg-August University, Göttingen

Second Reviewer: **Prof. Dr. Claus Ropers**, IV. Institute of Physics, Georg-August University, Göttingen

Further members of the Examination Board

apl. Prof. Dr. Alexander Egner, Institut für Nanophotonik, Göttingen

Prof. Dr. Hans Christian Hofsäss, II. Institute of Physics, Georg-August University, Göttingen

Dr. Robert Mettin, III. Institute of Physics, Georg-August University, Göttingen

Prof. Dr. Andreas Tilgner, Institute for Geophysics, Georg-August University, Göttingen

Date of the oral examination: 26.03.2021

Contents

Introduction

1

In 1895 Wilhelm Conrad Röntgen made the discovery of X-rays [Rön49] for which he was later awarded with the first Nobel prize. It is fascinating that the major fields of application for the ”new kind of radiation” developed almost immediately after his discovery. X-rays were first used for radiography in medical applications [Wil03] and a couple of years later also in radiotherapy [Pus02; Sen03]. About a decade later first experiments showed the diffraction of X-rays by a crystal [FKL13]. Radiography, radiotherapy and X-ray diffraction are nowadays still the major applications of X-rays. It is thus absolutely astonishing that it took less than 20 years after Röntgen’s discovery that these fields have been developed.

The strength of X-rays in these applications is manifold. In X-ray diffraction from crystals, the short wavelength λ, i.e. the high photon energy E_{ph}, of hard X-rays[1] allows for atomic resolution. In radiography, the weak interaction of X-rays with matter is crucial as it allows to penetrate through thick objects. One important number in this context is the complex refractive index $n = 1 - \delta + i\beta$. For hard X-rays n deviates only very slightly from unity. For example, for graphite and 12 keV X-rays the decrement δ, describing refraction, is on the order of 10^{-6}, and the imaginary part β, describing absorption, is on the order of 10^{-9} [Sch+11]. Concerning the weak refraction, Röntgen reported already in his first letter that he could not observe any refraction by prisms made of different materials [Rön49].

While this property of the refractive index benefits radiography, it simultaneously imposes a difficulty on the fabrication of high-quality refractive, diffractive or reflective X-ray optics[2]. Reflective optics, for example, can only be operated in grazing incidence below the critical angle, which is on the order of a few milliradians. As a consequence, the lack of high-quality optics impedes the design of resonators with low losses.

With high-quality resonators being the heart of (optical) lasers, the lack of X-ray resonators has severe implications for the design of X-ray lasers and thus for the generation of coherent X-rays. In addition, the ratio of the Einstein coefficients for stimulated

---

[1] We define hard X-rays to be roughly in the range of $E_{\mathrm{ph}} = 5\,\mathrm{keV}$ to 300 keV. In the following X-rays will be used synonymously with hard X-rays, if not stated otherwise.

[2] See [Pag06] for an overview on X-ray optics.

emission B_{21} and spontaneous emission A_{21} scales with $B_{21}/A_{21} \propto E_{\mathrm{ph}}^{-3}$ [HW13]. The design of X-ray lasers in analogy to optical lasers is thus not only hampered by the lack of high-quality resonators, but additionally by the scaling of the Einstein coefficients impeding population inversion in a laser medium. For this reasons, the coherent generation of hard X-rays with table-top sources is very limited. Applications requiring high coherence are restricted to large-facility sources like synchrotrons or X-ray free-electron lasers (XFEL).

In the soft X-ray and extreme-ultraviolet (EUV) regime, plasma lasers [Wan+08; Dep+15; God+09; Roc99] and especially the process of high-order harmonic generation (HHG) [McP+87; LSK91; Bar+02] allowed the generation of coherent radiation in the laboratory. HHG sources, for example, recently enabled imaging experiments [Kfi+17] with comparable quality to previous work at soft X-ray beamlines of synchrotrons and XFELs [Wan+12; Sch+13; Wil+17].

In contrast to the improvements in the soft X-ray regime, the concept of generating hard X-ray radiation in the laboratory has not changed much since Röntgens discovery. Table-top hard X-ray sources emit characteristic radiation and bremsstrahlung after electron impact onto an anode[3] into 4π sr. As approximately 99 % of the electron beam power is dissipated in heat inside the anode, the achievable brightness (i.e. photons (ph) per solid angle and per source area [ph mrad^{-2} mm^{-2}]) of X-ray tubes is limited by the heating of the anode [Dys90; Beh16]. In comparison to static anodes, X-ray tubes with rotating anodes [Beh16] or liquid-metal-jet anodes [HOH03; Ote+08] dissipate the heat in a larger fraction of anode material leading to a substantial brightness improvement.

With the improvement in coherence due to the advent of synchrotron radiation, X-ray radiography developed from plain shadowgraphy to a phase-sensitive coherent imaging technique [Jac+90; Sch+95; Clo+96; Mia+99]. A major advantage of phase-sensitive imaging is the fact that especially for materials composed of elements with low atomic number, such as soft tissue, the refraction is about a factor of 1000 higher than the absorption [Sch+11]. A lensless implementation of X-ray phase-contrast imaging is X-ray nearfield holography or synonymously propagation-based phase contrast imaging [Sni+95; Clo+96; Lag+97]. The basis for this technique is the invention of holography by Dennis Gabor [Gab48; GB49]. In X-ray nearfield holography the phase information is encoded in the intensity by free-space propagation.

Most objects under investigation in, e.g., biology or medicine exhibit complex three-dimensional (3d) structures. X-ray tomography enables the reconstruction of volu-

---

[3] X-ray anodes are commonly made of metal.

metric information from a series of projections under different angles [KS01; MW14] and thus allows to obtain 3d information. In phase-contrast tomography the contrast advantage of phase-contrast imaging is combined with the capabilities of 3d imaging [Mom+96; Clo+99].

The quality of the hologram in X-ray nearfield holography depends on the coherence of the illumination, as we will further elaborate in section 1.1.2. The recent brightness improvements of μ-focus X-ray tubes and the resulting increase in spatial coherence[4] advanced X-ray propagation-based phase contrast imaging and tomography with table-top X-ray tubes and micrometer resolution [Bar+13; Bus+18; Töp+18]. Higher resolution, however, requires synchrotron or XFEL radiation with high brightness [Bar+15a; Sch+15; Ced+17; Töp+18]. Even though synchrotrons provide beams with high partial coherence and high brightness, for holography with highest resolution (sub-100 nanometer), the lateral coherence needs to be further enhanced by optics. X-ray waveguides are a powerful tool to create a diffraction limited source spot with high numerical aperture and high spatial coherence [Pfe+02; Sal+15b]. To this end, the synchrotron beam is coupled into an X-ray waveguide, acting as a spatial coherence filter. With this technique resolutions below 25 nm have been obtained in X-ray holography [Bar+15b]. X-ray waveguides exist as one-dimensional (1d) planar structures [SS74] or two-dimensional (2d) channel waveguides [Pfe+02; Neu+14] and have a typical dimension of the guiding core on the order of 50 nm. While this sequential approach of first generating the X-rays and then filtering the spatially coherent part works well with synchrotron radiation with high brightness, a too large fraction of the radiation is discarded for X-ray tubes with low brightness. For this reason X-ray waveguides are largely irrelevant for laboratory sources today. One of the few examples for a combination of a 2d waveguide with a laboratory X-ray tube is the work of Fella et al., who used two crossed rather large waveguides (200 nm diameter) in combination with a liquid-metal-jet source. Using this approach, the authors could acquire phase-contrast images with acquisition times of ∼7.5 min and a couple of micrometers resolution [Fel+15]. For X-ray tomography requiring the acquisition of roughly 1000 projections, this would scale to a total acquisition time of more than 5 days.

In chapter 2 we demonstrate a novel approach circumventing the sequential approach of X-ray generation and coherence filtering by generating X-rays directly inside an X-ray waveguide with a table-top electron gun. To this end we have designed an X-ray anode forming a planar X-ray waveguide, which we bombard with an electron beam. The

---

[4] With spatial coherence we refer to lateral spatial coherence.

electrons generate bremsstrahlung and characteristic radiation which are both directly coupled into waveguide modes. The emitted radiation has a high degree of spatial coherence. We discuss how the electron beam power can be increased to reach an estimated brightness of 5×10^{11} ph mrad^{-2} mm^{-2}. Based on the Purcell effect [Pur46], well known from cavity quantum electrodynamics (CQED), we discuss the gain of emission into the waveguide modes.

The observation of quantum optical effects [Ada+13; RES20; RE21] with X-rays have been restricted to synchrotron radiation or XFELs so far. The combination of narrow-banded undulator radiation and Mössbauer nuclei led to the observation of various CQED effects with hard X-rays, such as the collective Lamb shift [Röh+10], subluminal propagation [Hee+15b], collective strong coupling [Hab+16], and Rabi splitting [Hab+17]. Recently, synchrotron radiation enabled CQED experiments with electronic resonances [Hab+19] as well. No CQED experiment has yet been performed with table-top X-ray sources.

Synchrotron radiation with its high brilliance[5] has advanced the field of X-ray phase-contrast imaging and tomography for static and even for dynamic samples [Lee+12; Wal+14; Ruh+17]. It is unsuitable, however, for the observation of fast dynamics with picosecond time resolution, due to its pulse duration on the order of 40 ps [Bal10] and a peak brilliance[6] of $\sim 10^{25}$ ph/(mrad^2 mm^2 0.1% BW) [Alt+06]. With a peak brilliance eight orders of magnitude (10^{33} ph/(mrad^2 mm^2 0.1% BW) [Alt+06]) higher than for 3rd generation synchrotrons and pulse durations of less than 100 fs [SSY00], XFELs enabled experiments in the ultrafast and non-linear optics regime [You+10; Roh+12; Hal+20; Hab+20; Ada03; RES20] and has led to observation of new effects not present in the visible regime, such as the anomalous nonlinear Compton effect [Fuc+15]. Apart from promising atomic resolution from single molecules in diffract-before-destroy schemes [Neu+00; Cha+06; Sei+11], XFELs are perfectly suited to study fast dynamics [Bar+08; Ino+16].

In chapter 3 of this work we develop an experimental scheme to study fast dynamics of laser-induced phase transitions with high spatial and temporal resolution and quantitative contrast in nearfield holography and demonstrate the setup with laser-induced cavitation bubbles [Bre14; Col48]. Cavitation is the process of bubble formation in a fluid. The laser-induced dielectric breakdown seeds a bubble nucleus, which is

---

[5] Brilliance is brightness per spectral width of the radiation, i.e. photons per solid angle, per source area, and per spectral width. It is common to give the spectral width for undulator radiation in units of 0.1 % of the whole band width (0.1 % BW) and for characteristic radiation per characteristic line.

[6] For pulsed sources peak brilliance is the maximum brilliance during the pulse.

followed by a fast expansion of the bubble, driving a shockwave, i.e. a compressed shell of fluid, in front of the bubble. We quantify the spatial pressure distribution of this shockwave in close proximity to the bubble nucleus experimentally for the first time, capturing the dynamics only nanoseconds after seeding. We observe discrepancies to numerical simulations, suggesting that more sophisticated models are necessary to describe the early dynamics after laser-induced dielectric breakdown. In chapter 4 we extend the method by X-ray diffraction to obtain information on the molecular structure during transient phase transition complementing the holography signal. Using this additional experimental approach we observe the non-equilibrium phase transitions after dielectric breakdown in a μ-fluidic water jet. After dielectric breakdown we quantify the pressure increase in the water jet and witness a transition of the molecular structure from a tetrahedral arrangement to the molecular structure of a simple liquid. We will show how single-pulse holography and diffraction at XFELs can complement each other to obtain quantitative information from the microscopic length scale to the molecular level with time resolutions, which are only limited by the pulse duration of the pump laser.

1.1 A need for bright sources: the example of propagation-based phase contrast imaging

While synchrotrons and XFELs offer very high beam quality in terms of brilliance or peak brilliance and ultrashort pulse durations, beam time is very restricted. Laboratory sources, however, are readily available but lack brightness and are thus constrained to low-coherence and low-photon flux applications.

In this section we will address these limitations by discussing the requirements for an exemplary type of experiments, namely propagation-based phase contrast imaging. To this end we will estimate the range of structure sizes which exhibit phase contrast under conditions of partial coherence. In addition we will discuss the influence of a finite resolution of the detector on the observable structure size. For a detailed introduction to X-ray holography the reader is referred to [Pag06].

1.1.1 Propagation-based phase contrast imaging

Dennis Gabor's invention of holography [Gab48; GB49] is the basis for X-ray near-field holography or propagation-based phase contrast imaging. As a phase-sensitive imaging technique, it uses interference effects to encode phase information of the object in the measurable intensity. Instead of using separate illumination and reference arms, the object is illuminated in an in-line geometry. Let the incoming complex wavefield $\Psi_{\text{in}}(\boldsymbol{r}_\perp, z)$ be a plane wave with wavenumber k propagating along z. $\boldsymbol{r}_\perp$ is a vector in the plane perpendicular to z. The disturbance by the object placed in the slab $z \in [z_{01} - \Delta, z_{01}]$ can be described using the projection approximation, so that

$$\Psi_{\text{out}}(\boldsymbol{r}_\perp, z = z_{01}) = \Psi_{\text{in}}(\boldsymbol{r}_\perp, z = z_{01}) \cdot \exp\left[-ik\bar{n}(\boldsymbol{r}_\perp)\right],$$

where $\bar{n}(\boldsymbol{r}_\perp)$ is given by the projection of

$$\bar{n}(\boldsymbol{r}_\perp) = \frac{1}{2}\int_{z_{01}-\Delta}^{z_{01}} \left[1 - n^2(\boldsymbol{r}_\perp, z)\right]\, \mathrm{d}z \approx \int_{z_{01}-\Delta}^{z_{01}} \left[\delta(\boldsymbol{r}_\perp, z) - i\beta(\boldsymbol{r}_\perp, z)\right] \mathrm{d}z,$$

with the complex refractive index $n = 1 - \delta + i\beta$. This approximation is valid as long diffraction inside the object can be neglected. The wavefield $\Psi_{\text{out}}(\boldsymbol{r}_\perp, z = z_{02})$ at the plane of detection is described by free-space propagation, which can be expressed by the Fresnel propagator in the near-field limit. The Fresnel propagator in its Fourier representation is given by the operator (as detailed in [Pag06])

$$\mathcal{D}_{z_{12}} = \exp\left(ikz_{12}\right) \mathcal{F}_\perp^{-1} \exp\left(\frac{-iz_{12}}{2k}\boldsymbol{k}_\perp^2\right) \mathcal{F}_\perp.$$

$\mathcal{F}_\perp$ and $\mathcal{F}_\perp^{-1}$ denote the Fourier transform in the sample plane and its inverse, respectively, with $\boldsymbol{k}_\perp$ being the reciprocal vector of $\boldsymbol{r}_\perp$. The propagation distance z_{12} between sample and detector is often expressed by the dimensionless Fresnel number $F = d^2/(\lambda z_{12})$ with a characteristic length d. We choose d to be the pixel size of the detector, which is a popular choice in X-ray holography. The measured intensity $I(\boldsymbol{r}_\perp) = |\Psi_{\text{out}}(\boldsymbol{r}_\perp, z = z_{02})|^2$ in the detection plane is given by the squared modulus of the wavefield.

Holography experiments are often performed with a diverging beam, i.e. in a cone beam geometry (Fig. 1.1a), to take advantage of the geometric magnification. According to the Fresnel scaling theorem a cone beam geometry can be transferred into an equivalent parallel beam geometry (see [Pag06] for details). The geometric magnification M of the cone beam is given by the ratio of the source-to-detector distance z_{02} and the source-to-sample distance z_{01}, i.e. $M = z_{02}/z_{01}$. The Fresnel scaling theorem states, that this situation is equivalent to a propagation by a parallel beam with a rescaled propagation distance $z_{\text{eff}} = z_{12}/M$, a rescaling of the image on the detector, i.e. a rescaling of the characteristic length d to $d_{\text{eff}} = d/M$, and an effective Fresnel number $F_{\text{eff}} = d_{\text{eff}}^2/(\lambda z_{\text{eff}})$.

To understand the impact of the dimensionless Fresnel number on the imaging contrast, let's consider a spherically shaped cavitation bubble phantom. The phantom consists of two concentric spheres with constant electron density ρ_e inside a homogeneous slab of uncompressed water (Fig. 1.1a, c). The inner sphere with lower density represents the gaseous bubble, whereas the outer shell has higher density than uncompressed water and represents the shockwave of the cavitation bubble. The radial (3d) electron density $\Delta\rho_e$ and the projected density profile $\Delta\bar{\rho}_e$ are shown as the difference to the density of the homogeneous slab in Fig. 1.1c. The 2d image of the holographic intensity for a Fresnel number of $F = 10^{-2}$ is depicted in Fig. 1.1b. The radial intensity of the hologram (Fig. 1.1d) shows how phase-contrast develops with decreasing Fresnel number F from gentle edge enhancement to strong holographic fringes. The direct contrast regime ($F \approx 10^{-1}$–10^{0}) is commonly used in propagation-based phase contrast imaging with laboratory X-ray sources, whereas in synchrotron experiments aiming at highest resolution experiments are performed in the holographic regime ($F \lesssim 10^{-2}$).

Quantitative information on the phase shift can be obtained from the holographic intensity by phase-retrieval algorithms. A variety of such algorithms have been proposed reaching from algorithms perfectly suited for the direct contrast regime [Pag+02; Bro02; Wit+09] to the holographic regime with single-step [Clo+99] or iterative approaches [Gur03; Gie+11; HTS18].

Why is phase-contrast imaging in the laboratory performed in a different regime, i.e at different Fresnel numbers, than experiments aiming at highest possible resolution at the synchrotron or XFELs?

1.1.2 Requirements for propagation-based phase contrast imaging

Let us consider a cone-beam setup with an incoherent source of finite source size σ_s and let us assume a detector with finite resolution σ_d. We will now estimate which structure sizes p are resolvable and exhibit phase contrast under experimental conditions of partial lateral coherence and limited detector resolution. While we aim at equipping the reader with an intuitive understanding of the key aspects, we refer to several studies [PGW97; WL04; WL07; HS18] treating the topic in detail.

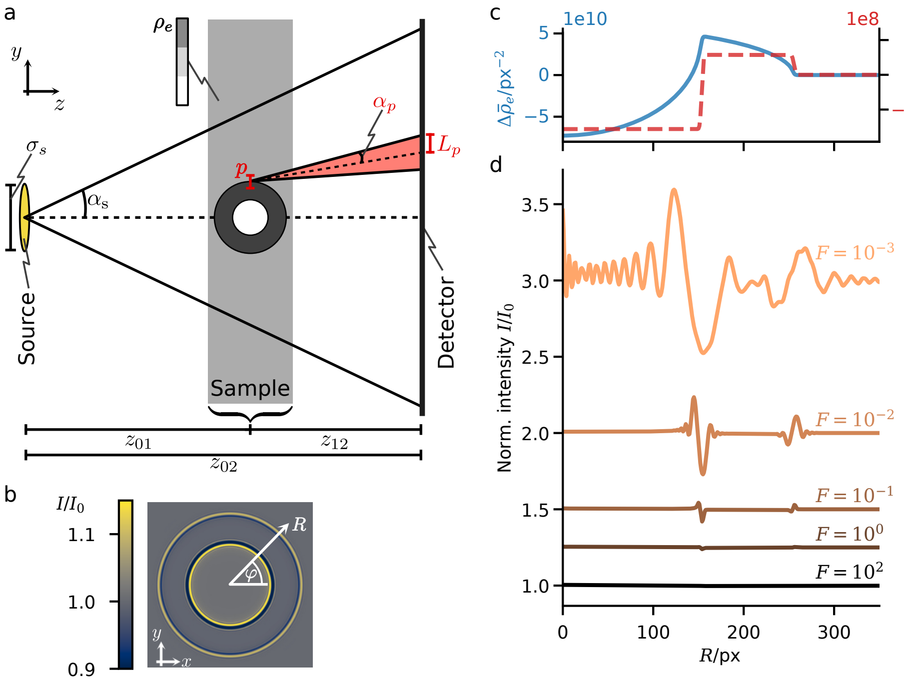

Fig. 1.1: X-ray near-field holography. (a) Cone-beam geometry of an X-ray holography setup. The source with size σ_s illuminates the sample which is placed in a thin slab at z_{01} behind the source. The detector at a distance of z_{02} behind the source is illuminated by the half cone angle α_s. The sample consists of different materials and densities. The sample depicted here is a phantom of a spherical cavitation bubble inside a homogeneous slab of water. The cavity of the bubble has lower density (vapour), whereas the compressed water in the shockwave shell has higher density than the homogeneous slab. In red: A structure with size p diffracts into the cone with half angle α_p leading to an extent of the diffracted cone of L_p on the detector. **(b)** Holographic intensity of a cavitation bubble phantom for a Fresnel number $F = 10^{-2}$. **(c)** Radial 3d electron density profile $\Delta\rho_e$ (red, right ordinate) of the cavitation bubble phantom, showing the difference to the homogeneous water slab, and projected electron density $\Delta\bar{\rho}_e$ (blue, left ordinate). **(d)** Radial intensity of the bubble phantom for different Fresnel numbers F. At high Fresnel numbers ($F = 10^2$) no phase contrast is visible. Medium Fresnel numbers ($F \approx 10^{-1}$–10^0), typical for experiments with table-top X-ray tubes and often referred to as direct contrast regime, show an edge enhancement in the intensity. Holographic fringes become visible for even smaller Fresnel numbers $F \lesssim 10^{-2}$. Experiments with synchrotron radiation aiming at highest resolution are typically performed in this holographic regime.

A structure with size p in the sample plane diffracts under an angle[7] of $\sin(\alpha_p) \approx \lambda/p$, corresponding to a lateral extent of $L_p = z_{12} \cdot \tan(\alpha_p)$ in the detection plane (cf. Fig. 1.1a). For hard X-rays with a wavelength on the order of 0.1 nm and structure sizes $p \gtrsim 1\,\mathrm{nm}$, the angle α_p is small, so that we can approximate the lateral extent on the detector by

$$L_p \approx \lambda z_{12}/p. \tag{1.1}$$

For interference, and thus phase contrast, the diffracted wave needs to be within the lateral coherence length $L_c \gtrsim L_p$ in the detection plane, with $L_c \approx \lambda z_{02}/\sigma_s$. This imposes a lower limit

$$p \gtrsim \frac{z_{12}}{z_{02}}\sigma_s = \sigma_s \left(1 - \frac{1}{M}\right)$$

for the structure size p to enable phase contrast, i.e. the structure size can not be smaller than the demagnified source size. This relation has great similarity to the result of [WL07] which was obtained by an approach based on Wigner distribution functions.

Furthermore, the structure with size p has to be illuminated coherently in the sample plane to enable interference. Thus the finite coherence length $l_c = \lambda z_{01}/\sigma_s$ in the sample plane imposes an upper limit on p

$$p \lesssim l_c = \frac{L_c}{M} = \frac{\lambda z_{02}}{M\sigma_s}.$$

Hence, the finite source size and thus the finite coherence length impose an upper and a lower limit on the structure size p. Both limits are visualized by the blue (lower limit) and red (upper limit) solid lines in Fig. 1.2. All structure sizes p between these two lines exhibit phase contrast. The range is maximized for $M \to 1$, with $M = 1$ describing the situation where sample and detection plane coincide, so that both fall in the plane with highest lateral coherence. While this is true for a perfect detector with infinite resolution, this property changes with a finite resolution of the detector.

To resolve the interference caused by diffraction at the structure with size p, the resolution σ_d of the detector needs to be smaller than the lateral fringe extent $L_p \geq \sigma_d$

---

[7] The exact shape of the structure might induce a constant factor in this relation. For simplicity we do not consider any exact shape and neglect this prefactor.

on the detector. With (1.1) we can formulate the upper limit

$$p \lesssim \frac{\lambda z_{12}}{\sigma_d} = \frac{\lambda z_{02}}{\sigma_d}\left(1 - \frac{1}{M}\right).$$

Furthermore, we require the structure to be resolved by the detector, i.e.

$$p \gtrsim \frac{\sigma_d}{M}.$$

Both limits imposed by the finite resolution of the detector are visualized by the dashed lines in Fig. 1.2.

To conclude, both the finite source size and the finite resolution of the detector impose an upper as well as a lower limit on the structure size p to enable phase contrast and to be detected. Combining these four limits we obtain the following range for p

$$\max\left\{\sigma_s\left(1 - \frac{1}{M}\right), \frac{\sigma_d}{M}\right\} \lesssim p \lesssim \min\left\{\frac{\lambda z_{02}}{M\sigma_s}, \frac{\lambda z_{02}}{\sigma_d}\left(1 - \frac{1}{M}\right)\right\}. \tag{1.2}$$

As the inverse magnification $1/M$ is bound to the interval $(0, 1)$ for a diverging beam, there is only a solution for p if the condition

$$\sigma_d \lesssim \frac{\lambda z_{02}}{\sigma_s} = L_c$$

is fulfilled. This result is rather intuitive. It requires the resolution of the detector to be smaller than the coherence length in the detection plane, as phase contrast is only visible within the coherence length.

The white area in Fig. 1.2 contains all values p and $1/M$ for which the condition (1.2) is fulfilled, for the example with $\sigma_d = 1.5\sigma_s$ and $\lambda z_{02} = 4\sigma_s$. Consequently, phase contrast experiments can only be performed in that regime.

To maximize the range of the structure size p to develop phase contrast for any magnification M, there are three different options for a given wavelength λ. Firstly, a larger source-to-detector distance z_{02} increases both upper limits on p and thus enhances phase contrast for larger structures. However, an increase in z_{02} decreases the photon flux on the detector with z_{02}^{-2}. Secondly, a better resolution of the detector (lower σ_d) decreases the lower limit on p towards lower magnifications M and increases the upper limit on p imposed by the detector. It thus increases the range for p in both directions for low magnifications. The photon flux however scales with the area of one detection element and thus the flux decreases with σ_d^2. But even if an infinite photon flux was

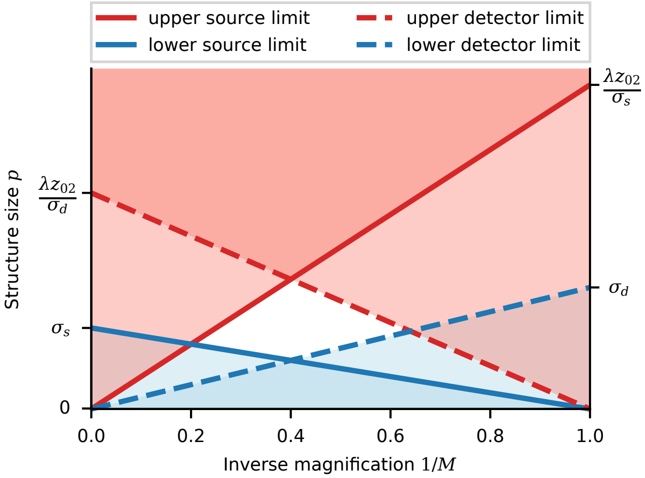

Fig. 1.2: Requirements for phase contrast. The finite source size σ_s and the finite resolution of the detector σ_d impose both an upper (red) and lower limit (blue) on the structure size p to enable and detect phase contrast in near-field holography. The white area marks the structure sizes and magnifications M for which all requirements are fulfilled. The plot shows the situation for $\sigma_d = 1.5\sigma_s$ and $\lambda z_{02} = 4\sigma_s^2$. In this example the range for p is maximized for an inverse magnification of $1/M = 0.4$.

available, the resolution of the detector would be limited by its technical realization. X-ray detectors with highest resolution are scintillator-based and their resolution is limited by the point-spread-function of the secondary radiation which depends on the type of scintillator and its thickness. Thinner scintillators give a better resolution but lower conversion efficiency. The resolution is limited to just below 1 µm [full width at half maximum (FWHM)] with an detective quantum efficiency of 2–5 % [Sta+02]. The third option to extent the range of resolvable structure sizes is to decrease the source size σ_s. A smaller source spot decreases the lower limit and simultaneously increases the upper limit on p towards higher magnifications. Nevertheless a smaller source spot σ_s typically decreases the photon flux as well. The scaling depends on the type of source. Apertures or slits decrease the flux with σ_s^2, whereas the maximum electron beam power and thus the flux scales linearly with the diameter of the source spot σ_s in the limit of thick anodes [GWA86]. A minimal source size using thick anodes is imposed by multiple scattering of electrons, however. Thin anodes as commonly used in transmission target X-ray tubes allow for smaller source spots, but only at the cost of further reducing the flux [Beh16]. In conclusion, all three options to increase the range for structure sizes p accessible with phase contrast decrease the photon flux.

X-ray phase-contrast tomography of unstained tissue with a volume of $\sim 1000^3$ resolution elements and 1.3 µm resolution (FWHM) at a liquid-metal-jet X-ray tube requires, for example, a total acquisition time of ∼14 h [Töp+18]. A higher resolution thus quickly increases the acquisition time to impractical values, as one has to consider that the setup and especially the sample need to be stable over this period of time. Whereas longer acquisition times might be to some extent an option for static samples, there is no possibility to increase the acquisition time for dynamic samples and time-resolved measurements. This prompts at the requirement for X-ray sources with high brightness.

1.2 Outline of the thesis

This work presents experiments involving the full range of available X-ray sources. On the one hand we exploit the extremely high peak brilliance of XFELs to observe dynamics using single femtosecond pulses with propagation-based phase contrast imaging. On the other hand we present a novel concept for the generation of spatially coherent X-rays with high brightness, emitted directly into the modes of an X-ray waveguide. Our results promise to shrink the gap in brilliance between table-top and large-facility X-ray sources.

In chapter 2, we report on a novel X-ray source concept to generate spatially coherent X-rays directly inside a planar X-ray waveguide by electron bombardment. The experimental results are compared to simulations and to results from X-ray fluorescence of the same waveguide systems at the synchrotron. We estimate the gain increase and extrapolate our experimental results to get a realistic brightness estimation under optimal conditions.

In chapter 3 we exploit the capabilities of highly brilliant X-ray sources with ultrashort pulses for the observation of fast dynamics with high temporal and spatial resolution in nearfield holography. In a pump-probe approach we use single-XFEL pulses to image the dynamics of laser-induced cavitation bubbles with nanofocus X-ray holography. We apply a tailored phase-retrieval approach to access the quantitative phase shift of the cavitation bubbles. The phase information is used to calculate the spatial pressure distribution of the shockwave driven by the expansion of the bubble. We compare our results to numerical models.

In chapter 4 we explore dielectric breakdown in a µ-fluidic water jet. We complement the X-ray holography approach from chapter 3 with time-resolved X-ray diffraction to obtain information on the molecular structure of water. We use the information on the molecular structure to calculate the pressure dynamics following the dielectric breakdown. In this combined approach we are able to obtain quantitative information from the microscopic length scale to the molecular level with time resolutions, that are only limited by the pulse duration of the pump laser.

We conclude with a summary and discussion of all results and provide an outlook in chapter 5.

Observation of electron-induced characteristic X-ray and bremsstrahlung radiation from a waveguide cavity

2

MALTE VASSHOLZ, TIM SALDITT

reproduced[1] from Science Advances **7***, eabd5677 (2021)* [VS21]

We demonstrate X-ray generation based on direct emission of spontaneous X-rays into waveguide modes. Photons are generated by electron impact onto a structured anode target, which is formed as an X-ray waveguide or waveguide array. Both emission of characteristic radiation and bremsstrahlung are affected by the changes in mode density induced by the waveguide structure. We investigate how the excited modal pattern depends on the positions of the metal atoms and the distance of the focused electron beam with respect to the waveguide exit side. We compare the results to synchrotron-excited fluorescence. We then discuss how X-ray generation in waveguides can be used to increase the brilliance and directional emission of table-top X-ray sources, with a corresponding increase in the spatial coherence. On the basis of the Purcell effect, we lastly show that the gain of emission into waveguide modes is governed by the quality factor of the waveguide.

---

[1] Subject to minor corrections.

2.1 Introduction

X-ray generation at the laboratory scale largely relies on electron impact sources and generation of characteristic X-ray radiation or bremsstrahlung in metal anodes. The continuous development of these sources has spurred fundamental science, particularly structure analysis by crystallography and X-ray diffraction, and benefits every day applications of medical imaging or non-destructive testing [Beh16]. The recent increase in brightness by μ-focus sources and especially liquid jet anodes [HOH03; Ote+08] now enables new applications by phase-contrast imaging and high resolution diffraction. Notwithstanding this progress, the principles of X-ray emission after K-shell ionization or by bremsstrahlung interaction in an anode have been the same over the past 120 years. In particular, the fact that non relativistic electron impact sources emit X-ray photons into the entire solid angle of 4π sr, with only smooth modulations due to polarization and self-absorption effects, severely limits their brightness [e.g., ph/(mm^2 sr s), where ph denotes photons]. Collecting photons over a wide angular range and refocusing them onto a sample is hampered by the fact that the X-ray index of refraction $n = 1 - \delta + i\beta$ asymptotically approaches one for high photon energy E. Resonators with sufficient quality factor Q to exploit effects of cavity quantum electrodynamics, for example, seem to be out of reach for broad-band laboratory radiation. Cavities based on dynamic single crystal reflection, for example, can be operated only for extremely narrow-banded radiation, making synchrotron radiation indispensable [Shv+03; Cha+05; Shv+10; Hal+20]. This is in sharp contrast to visible light, where the spontaneous emission is easily modified, already by placing the emitting molecule near a single interface [DKS68]. When incorporated into a suitable resonator, spontaneous emission can be suppressed or enhanced, known as the Purcell effect [Pur46], by many orders of magnitude. Changes in the modal density by structured matter, are in principle also known for X-rays since the discovery of the Kossel effect in single-crystal anodes [KLV35], and as an extension, angular modulations of X-ray fluorescence are also commonly observed in thin films and multilayers, both for excitation with synchrotron radiation and electrons [Jon+02; KLS95; AJ10], including the regime of relativistic electrons [Kap+11]. These effects have also been discussed in view of possible use for X-ray lasers [AJ10].

A much stronger modification of the modal density, however, can be provided by waveguides. Waveguiding becomes possible for X-rays by total reflection at grazing angles within suitable thin-film structures [SS74; Fen+93; Lag+97; Zwa+99; Pfe+00], or in two-dimensional channel waveguides [Pfe+02; Jar+05; CHS15], which can in principle offer much higher Q. In the simplest case, a planar guiding layer can be formed for example by a thin film with low electron density, surrounded by a high electron density cladding, enabling beam confinement down to sub-10 nm full width at half maximum (FWHM) [Krü+12]. Planar X-ray waveguides have already been used for fundamental X-ray quantum optics experiments in nuclear resonant scattering, e.g. measurements of increased spontaneous emission of atoms in a cavity [Röh+05], the collective Lamb shift of a cavity mode [Röh+10], electromagnetically induced transparency [Röh+12], the collective strong coupling of X-rays and nuclei [Hab+16], as well as for coupling to electronic resonances [Hab+19]. These X-ray quantum optics experiments as well as coherent imaging with waveguide modes [Bar+15b] rely on the coupling of highly brilliant synchrotron radiation into X-ray waveguides. While feasible for synchrotron radiation, this sequential approach of first generating X-rays and then coupling them into a waveguide is unsuited for laboratory X-ray radiation because of the low brilliance of electron impact sources. For this reason, waveguide optics is largely irrelevant for laboratory X-ray radiation today.

In this work, we present evidence for direct emission of characteristic and bremsstrahlung radiation into a waveguide. We directly generate X-rays inside a waveguide by a μ-focus electron beam (*e*-beam). This is fundamentally different from first generating the X-rays and then coupling into the waveguide, even if done in close proximity as in [DKK95], and results in pronounced peaks in the angular far-field distribution. Hence, X-ray emission into waveguide modes not only is of interest in view of X-ray quantum optics but also could augment the performance of electron impact sources since waveguides with $Q \gg 1$ could be exploited for a correspondingly increased spatial coherence. Furthermore, we show that the distance Δz between the spot of electron impact and waveguide exit can be used to control the far-field emission pattern. Last, we compare the measured far-field distribution to waveguide emission of X-ray fluorescence excited by synchrotron radiation, which we measure for the same waveguides, again with a precise control of Δz.

2.2 Experimental setup

To excite characteristic and bremsstrahlung radiation by electron bombardment inside the waveguide structures, we used the *e*-beam and electron optics of a modified μ-focus X-ray tube (R5 prototype, *Excillum AB*, Sweden). A custom anode chamber design allowed the mounting of a planar waveguide structure on a grounded metal support.

A main control parameter was the distance Δz between the exit side of the waveguide structure and the point of X-ray generation (Fig. 2.1A), i.e., the position of the electron spot, which was varied by adapting the current in the deflection coils. The *e*-beam was focused to a spot size of 10 µm FWHM. We varied the acceleration voltage between 15 and 50 kV with a total *e*-beam power of 400–450 mW. A silicon drift detector (SDD) resolved the X-rays outside the anode chamber as a function of photon energy E and angle θ_f with respect to the waveguide horizon (Fig 2.1A). For an increased angular resolution $\Delta\theta_f$ of the detection angle the SDD detector can be replaced by the charge-integrative hybrid pixel detector MÖNCH (MÖNCH03 prototype, Paul Scherrer Institut) [Ram+17]. Inside the waveguide anode, the X-rays are generated (Fig. 2.1A) either in a small, nearly monoatomic layer [fluorescent metal layer (FL)] within the low density guiding layer and/or inside the metal cladding layer. The X-rays generated within a region enveloped within a waveguide mode can couple into the mode, regardless of whether the metal is contained in the fluorescent layer, dispersed in the guiding layer or contained in the cladding layer. The latter is of practical importance since the high-density cladding is almost always composed of metal atoms. X-rays that are emitted into the waveguide modes can exit either through the top for the case of a leaky waveguide design based on a thin top cladding, or after propagation in the guiding layer at the exit side, i.e., at the truncation of the thin-film structure (Fig. 2.1B). The recorded intensity patterns (Fig. 2.1C) are interpreted with respect to the simulated modes of the waveguide, with their characteristic nodes and antinodes. For comparison, we excited X-ray induced fluorescence with a table-top µ-focus X-ray tube and synchrotron radiation. The observation angle of the X-ray fluorescence was at 90° to the primary X-ray beam (see Fig. 2.1A). The synchrotron setup was the `GINIX` endstation [Sal+15b] at the beamline P10 (PETRAIII, DESY). The synchrotron beam was focused to sub-micrometer spot size by a Kirkpatrick-Baez mirror system. Details of all setups, instrumentation, and parameters used are given in Methods.

Samples: We performed experiments with three different planar waveguide systems, to which we will refer as *Cu/Co*, *Fe/Ni*, and *Mo/C* system. The exact layer compositions are given in Table 2.1. The *Cu/Co* system is a single waveguide with a small nearly monoatomic layer (∂-layer) of *Co* in the *C* guiding layer sandwiched between *Cu* cladding layers. The thin top cladding allows for resonant beam coupling (RBC) into and out of the guided modes from the top interface. The two other systems are multiwaveguide systems, i.e., waveguides with multiple guiding layers. The *Fe/Ni* system is a 50×-stack of waveguides with a small ∂-layer of *Fe* in the center of the *C* guiding layer, sandwiched between *Ni* cladding. The *Mo/C* multiwaveguide system

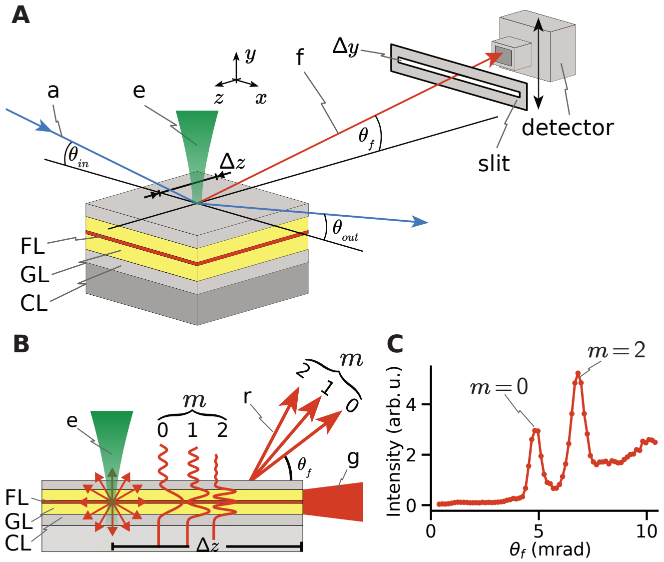

Fig. 2.1: X-ray generation in waveguides. (A) An *e*-beam (e) impinges onto a planar waveguide consisting of cladding layer (CL), guiding layer (GL), and a central fluorescent metal layer (FL). The electron impact excites atoms, which emit characteristic X-rays and bremsstrahlung into the waveguide. Angle- and energy-resolved detection is implemented by scanning an SDD detector. To increase the angular resolution, the SDD can be replaced by the MÖNCH detector. For excitation with X-rays: The *e*-beam (e) is replaced by a focused X-ray beam (a) impinging the waveguide in grazing incidence. Here, the detection is in an angle of 90° to the primary X-ray beam. Both beams (e) and (a) can be scanned in Δz to change the propagation length of the generated X-rays inside the waveguide. **(B)** Detailed view on the X-ray generation with electron impact. Characteristic X-rays are emitted into waveguide modes with mode numbers m. The X-rays exit the channel either through the thinned top cladding by evanescent waves (r) or directly at the end of the channel (g). **(C)** Detected far-field emission of characteristic X-rays generated inside the waveguide shows sharp emission peaks at the structure's horizon.

contains 30 waveguides with a ∂-layer of *Mo* in the center of the *C* guiding layers. The thick *Mo* cladding layers suppress RBC and thus reduce X-rays, leaving the channel through the top of the waveguide. Further details on the sample preparation are given in Methods.

The three systems were chosen to investigate several different metal compositions and geometric designs. While two systems allow the separation of fluorescent layer and cladding layer contributions, the *Mo/C* multiwaveguide system is designed in view of higher signal with cladding layer and fluorescent layer emitting at the same energy. The concept of amplification by waveguide multilayers is also particularly relevant for future upscaling. Note that for most applications, it is not necessary to separate the emission of different layers, as they would all emit into the same radiation cone.

Simulations: We simulated the X-ray generation inside the waveguides based on the reciprocity theorem. Accordingly, the simulation process is inverted to the experimental conditions. Instead of asking for the far-field probability distribution of a photon emitted from the location of a metal atom into a waveguide mode, propagating through the guide, and then leaving through the thinned top cladding or the side face, we ask for the field intensity at a given metal location inside the waveguide, when a far-field solution, i.e., a plane wave, impinges onto the structure (Fig. 2.2). If the excitation is far from the waveguide's exit face and the radiation can enter and exit only through the cladding (i.e., large Δz), the calculation of the wavefield inside the guides can be carried out for semi-infinite media and beams by matrix methods (Parratt) [Par54]. To describe the Δz dependence as required for the measurements close to the exit side at small Δz, we have used a finite-difference propagation code [MS17], taking into account the finite size and, if needed, the full dimensionality of the structure. We have verified that for semi-infinite systems and infinite beams, the two simulation approaches (finite difference and Parratt) give identical results. Fig. 2.2A shows the spatial intensity distribution inside a single waveguide channel with the same layer composition as the *Mo/C* multiwaveguide system. The intensity of the propagated field was calculated by finite-difference simulations [MS17]. The internal intensity distribution in the yz plane is shown for different plane wave angles of incidence θ_{PW}, each matching a different mode. In terms of the reciprocity theorem, the maps indicate the probability that a photon emitted at the given location exits to the corresponding far-field angle θ_f. Note the symmetries of the modes along y and the breaking of translational symmetry invariance along z that is induced by the truncation of the waveguide (exit side). Fig. 2.2B shows the intensity variation in the central metal layer with peaks corresponding to the modes. The broad maximum at $\theta_{\mathrm{PW}} \simeq 0$ corresponds

Table 2.1: Waveguide samples. The layer composition of the three samples is listed from top to bottom.

Sample	*Cu/Co*	*Fe/Ni*	*Mo/C*
Top layers	$1 \times \left\{\begin{array}{ll} Cu, & 5\,\text{nm} \\ C, & 20\,\text{nm} \\ Co, & 2\,\text{nm} \\ C, & 20\,\text{nm} \end{array}\right.$	$50 \times \left\{\begin{array}{ll} Ni, & 10\,\text{nm} \\ C, & 24.5\,\text{nm} \\ Fe, & 1\,\text{nm} \\ C, & 24.5\,\text{nm} \end{array}\right.$	$30 \times \left\{\begin{array}{ll} Mo & 25\,\text{nm} \\ C, & 16\,\text{nm} \\ Mo, & 1\,\text{nm} \\ C, & 16\,\text{nm} \end{array}\right.$
Bottom layer	*Cu*, 40 nm	*Ni*, 30 nm	*Mo*, 30 nm
Buffer layer	–	–	*Cr*, 10 nm
Substrate	*Si*	*Si*	*Si*
Fabrication process	Pulsed laser deposition	Magnetron sputtering	Magnetron sputtering

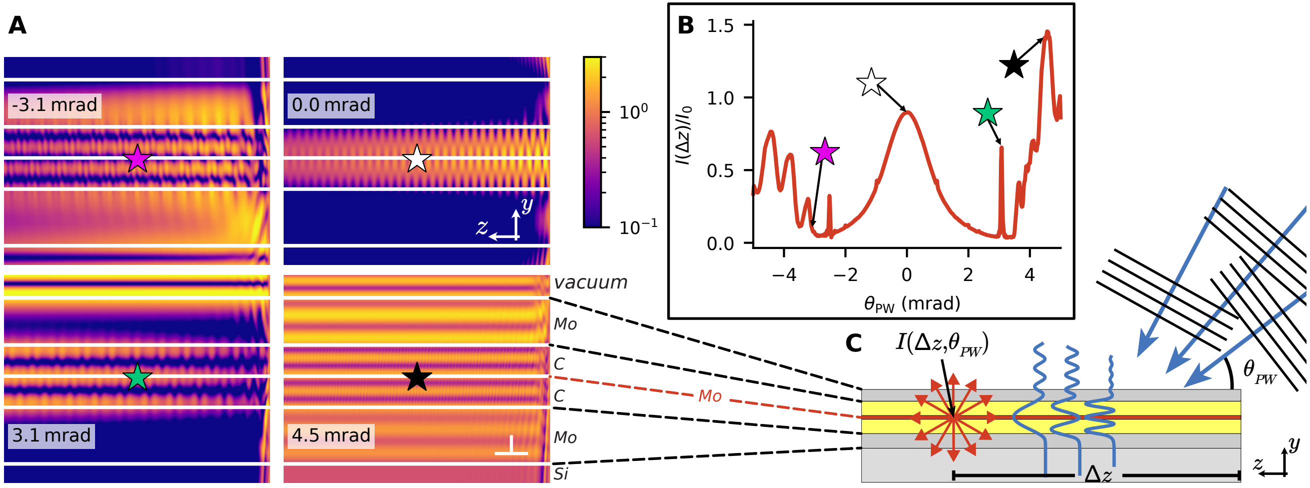

Fig. 2.2: Simulation of propagation and modal emission. **(A)** Propagation of the electric field inside a single *Mo/C* waveguide, when a plane wave is incident under the angle θ_{PW} as given in the inset. The main direction of propagation is along the z direction [see **(C)**]. The propagation is based on finite difference simulations. **(B)** Intensity of the propagated field as a function of θ_{PW} in the center of the guiding layer and at a distance of $\Delta z = 400\,\mu\mathrm{m}$ to the side edge. The colored stars mark the positions in (A) and (B). According to the reciprocity theorem, we now change directions: If an atom in the center of the guiding layer and at a distance of $\Delta z = 400\,\mu\mathrm{m}$ emits X-rays, then the intensity measured at an angle $\theta_f = \theta_{\mathrm{PW}}$ is given by (B). Scale bars (A), 10 nm in y, and 100 µm in z. The color in (A) scales with the normalized intensity of the electric field on a logarithmic scale.

to side coupling. As an interesting interference phenomenon, if one ”moves” an excited atom along z in the cavity, the emission rate into a waveguide mode oscillates with z, i.e., with the distance Δz to the exit side. This effect highlights that the emission into specific modes is modified by both dimensions of the waveguide structure. While the interpretation in terms of modal propagation is comparably simple for a structure with a single waveguide, the interference effects when simulated for the multiwaveguide system become both more complex and much more pronounced.

2.3 Results

Fig. 2.3 shows the recorded far-field patterns of the characteristic *Co* and *Cu* radiation for the *Co/Cu* waveguide excited by electron bombardment, and for comparison, also fluorescence induced by a laboratory µ-focus X-ray source for the same sample structure. The data were recorded by the SDD detector with an angular resolution of $\Delta\theta_f = 250\,\mu\text{rad}$ for X-ray induced fluorescence and $\Delta\theta_f = 285\,\mu\text{rad}$ for electron impact. The *Co*-K radiation, which is excited in the central ∂-layer, couples preferably to the even modes of the waveguide cavity, namely $m = 0$ and $m = 2$ with antinodes in the central *Co* layer (Fig. 2.3A for *Co*-K$_\alpha$ and Fig. 2.9 for *Co*-K$_\beta$). For the *e*-beam-excited characteristic radiation, the radiant flux Φ_p per *e*-beam power [ph/(s mrad^2 W)] is given on the right ordinate. The modal pattern of the *Cu*-K$_\alpha$ radiation, excited in the cladding, peaks at even and uneven modes, as expected since all modes exhibit strong evanescent tails in the cladding (Fig. 2.3B). For the signal detected from both layers, electron and X-ray excitation show similar patterns. The peak positions agree with the simulations. For better comparability, we have convolved the angular distribution of the simulated data with the instrumental resolution of $\Delta\theta_f = 250\,\mu\text{rad}$. Synchrotron-excited fluorescence of this structure with higher angular resolution and where the radiation exits through the side edge of the waveguide are shown in Fig. 2.10.

To investigate the emission of X-rays into multiwaveguides we first turn to synchrotron-excited fluorescence inside the *Fe/Ni* multiwaveguide system before investigating this effect for characteristic radiation generated by electron bombardment. The synchrotron setup has two advantages for the interpretation of the experimental data: (i) The monochromatic 8 keV beam allows for the excitation of the central *Fe* layers only, whereas the K-edge of the *Ni* cladding layers is above the primary photon energy. (ii) The nanofocused synchrotron beam excites a small region only, such that the distance Δz to the side edge of the waveguide structure is well controllable with negligible

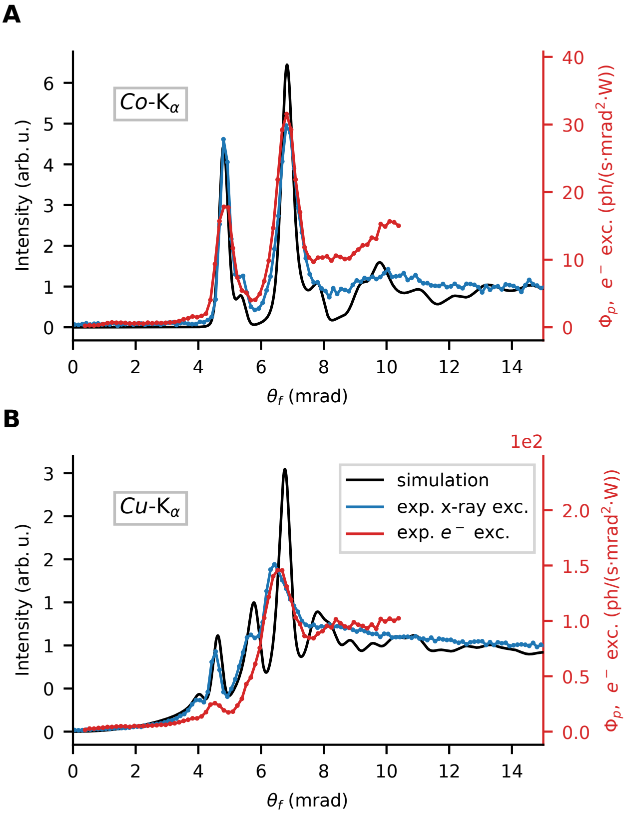

Fig. 2.3: Characteristic radiation in the *Co/Cu* waveguide. Far-field intensity of the characteristic K_α lines, exhibiting modal peaks as a function of angle θ_f with respect to the waveguide horizon. Intensities measured with an SDD detector excited with electron impact and, for comparison, fluorescence excited with a laboratory X-ray tube. The right ordinate shows the K_α radiant flux Φ_p per *e*-beam power for the characteristic (*e*-beam excited) radiation. **(A)** *Co*-K_α radiation excited in the central ∂-layer. **(B)** *Cu*-K_α radiation excited in the cladding. Peak positions match the simulated intensities.

primary beam size. Fig. 2.4A shows the *Fe*-K signal of an exemplary detector image of the MÖNCH. By interpixel interpolation of the MÖNCH, we obtain a sampling corresponding to $\Delta\theta_f \simeq 25\,\mu$rad. The signal shows strong modulations along the θ_f direction. Along the $\theta_\perp$ direction, perpendicular to θ_f, the intensity is constant, as expected because of the planar geometry. By integration over the horizontal extent (along $\theta_\perp$) of the detector, we obtain the intensity curve $I_{Fe}(\theta_f)$ (Fig. 2.4B). Fluorescence photons trapped in a waveguide mode can either leak out via an evanescent wave to the top (the equivalent of RBC), or at the side face of the waveguide (the equivalent of front coupling). The second fraction of fluorescence radiation results in an interference pattern near the horizon, and is emitted from an effective source of small cross-section with high divergence, controlled by the waveguide structure, i.e., mainly the guiding layer thickness. Both beams are spatially coherent, hence, the fraction leaking through the top originates from a large source spot and has low divergence [JD04].

By scanning the synchrotron beam toward the edge of the waveguide, we obtain for each position Δz an intensity curve $I_{Fe}(\theta_f)$. Fig. 2.4C shows these curves as an intensity map $I_{Fe}(\theta_f, \Delta z)$. The intensity map highlights the periodicity in Δz of the radiation exiting at the side face of the waveguide ($\theta_f \simeq 0$). The modal structure, which we already observed for the single waveguide (cf. Fig. 2.3), appears again for radiation ”leaking” through the top but is now modified by multiwaveguide interference. Note the pronounced interference effects at the truncated side face of the waveguide structure. Fig. 2.4D shows simulated data for comparison.

As we show next, the strong modulation effects of X-ray emission in truncated waveguide arrays can also be exploited for characteristic radiation with electron impact sources. For the generation of characteristic X-rays with electron impact inside multiwaveguides we chose the *Mo/C* structure. The 25 nm thick *Mo* cladding suppresses radiation leaking evanescently through the top cladding and thus enhances the fraction of radiation exiting at the edge of the waveguide structure. Furthermore, the cladding and the central metal layer, contribute to the same characteristic lines. We used the MÖNCH area detector with $4\times$ subpixel interpolation, resulting in an angular resolution of $\Delta\theta_f \simeq 25\,\mu$rad. A 35 µm thick *Ag* foil was used as spectral filter, to enhance the contrast between the bremsstrahlung background and characteristic *Mo*-K emission. Since the *e*-beam spot is substantially larger than the focused synchrotron beam, we expect the intensity modulations along Δz to be less sharp than in the synchrotron measurements. We have used the Monte Carlo software package *PENELOPE2014* [Sal15] to simulate the electron dose distribution in the structure for a given acceleration voltage, verifying that the *e*-beam reached deep into the buried waveguide structure.

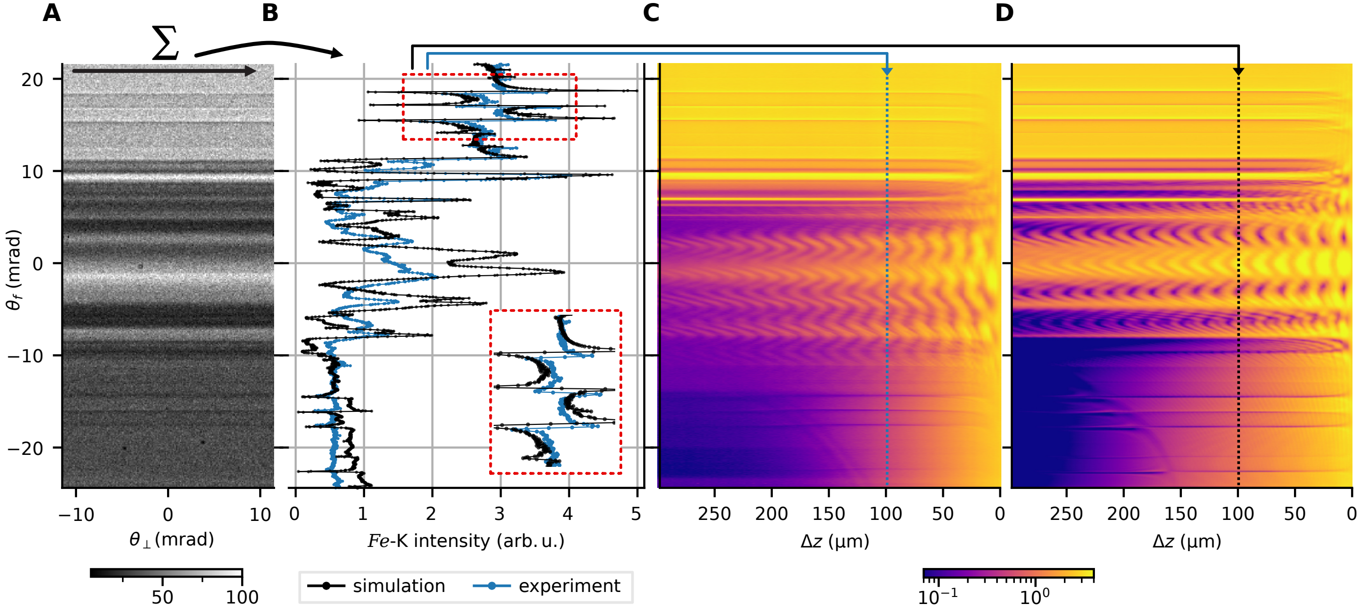

Fig. 2.4: Synchrotron-excited fluorescence inside the *Fe/Ni* multiwaveguide. Modification of *Fe*-K fluorescence intensity I_{Fe} by the waveguide modes, measured by scanning a focused synchrotron beam close to the side face of the waveguide. **(A)** Detector image of I_{Fe}, shows strong modulations as a function of θ_f, whereas I_{Fe} is constant along the lateral direction $\theta_\perp$. Radiation exits through both interfaces: the exit face of the waveguide $\theta_f \simeq 0$ and the top cladding. The intensity at negative θ_f is damped by absorption in the substrate. **(B)** $I_{Fe}(\theta_f)$ is obtained after integration along $\theta_\perp$ of the detected intensity. The simulated intensity is shown for comparison. The zoom in the inset shows Fano-like lineshapes. **(C)** The variation of fluorescence intensity close to the exit side $I_{Fe}(\theta_f, \Delta z)$, with each column of the matrix corresponding to an intensity profile such as in (B). Pronounced oscillations show that the emission of fluorescence oscillates with distance to the exit of the waveguide. **(D)** Simulated intensity. The arrows indicate Δz of the profiles shown in (B). The color scales with the intensity in arbitrary units on a linear scale (A) and logarithmic scale (C and D).

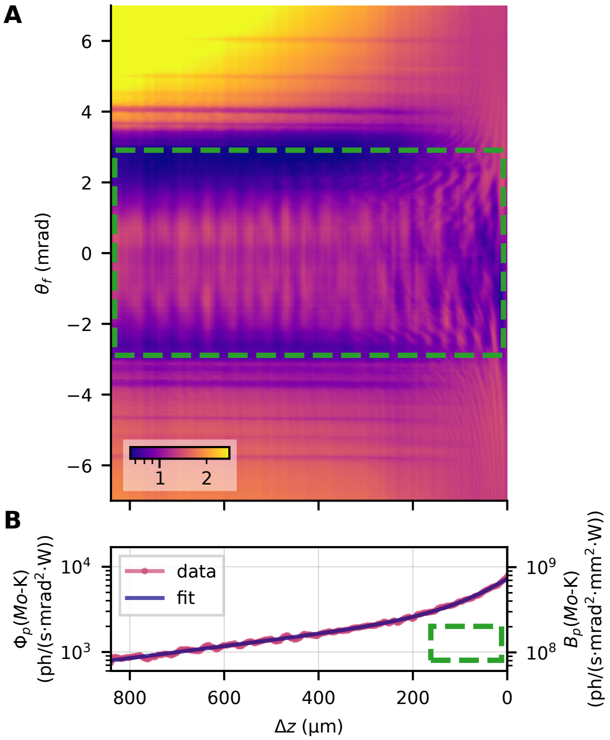

Fig. 2.5: Characteristic radiation of the *Mo/C* multiwaveguide. Variation of characteristic *Mo*-K intensity when scanning the *e*-beam toward the truncated side of the waveguide array. **(A)** I_{Mo} as a function of the exit angle θ_f and the distance Δz between the *e*-beam position and the waveguide edge. For better visibility of the interference effects of the radiation exiting through the side edge, the intensity map $I_{Mo}(\theta_f, \Delta z)$ has been corrected for the damping of the waveguide, by a division with Φ_p^{fit} (see below). **(B)** Total radiant flux Φ_p per incident *e*-beam power of *Mo*-K radiation exiting through the side face of the waveguide, i.e., between the angular range $|\theta_f| \leq 2.9\,\text{mrad}$ [green rectangle in (A)]. The least square fit Φ_p^{fit} of a bi-exponential decay to the radiant flux Φ_p yields two characteristic decay lengths ($1/e$-lengths), a slow decay $\Delta z_{1/e} = 622(11)$ µm and a faster decay $\Delta z_{1/e} = 82(2)$ µm, which can be attributed to the 0th and 1st mode, respectively. The right ordinate shows the *Mo*-K brilliance per *e*-beam power of the radiation leaving through the side edge. The color in (A) scales with the intensity in arbitrary units on a logarithmic scale.

Fig. 2.5A shows the *Mo*-K radiation as a function of angle θ_f and distance Δz, recorded by scanning the *e*-beam over the *Mo/C* waveguide target along z. Fig. 2.5B shows the intensity exiting through the side face of the channels (integrated intensity within $|\theta_f| \leq 2.9$ mrad; cf. green rectangle in Fig. 2.5A) in terms of radiant flux Φ_p per unit *e*-beam power for characteristic *Mo*-K emission. A bi-exponential decay Φ_p^{fit} is fitted to Φ_p to determine the characteristic decay lengths $\Delta z_{1/e}$ of the intensity inside the waveguides. The least square fit yields a slow decay with $\Delta z_{1/e} = 622(11)$ µm and a fast decay with $82(2)$ µm. The slow decay can be attributed to the damping of the 0th mode ($m = 0$), whereas the fast decay can be attributed to the 1st mode ($m = 1$), with a higher fraction of the modal intensity in the cladding and, thus, stronger absorption. We can estimate an effective X-ray source spot of $A_{\text{X-ray}} \simeq 9.9\,\mu\text{m}^2$ for the radiation leaving through the side face of the waveguides, given by the guiding layer thickness times the number of waveguides 33 nm × 30 in the y direction and the width of the *e*-beam of 10 µm in the lateral direction. Dividing Φ_p by $A_{\text{X-ray}}$ yields the brilliance B_p of the *Mo-K* radiation leaving through the waveguide's side edge per *e*-beam power (cf. right ordinate in Fig. 2.5B). To improve the visibility for the interference effects of the radiation leaving the waveguide array at the side face, we have corrected the intensity map $I(\theta_f, \Delta z)$ in Fig. 2.5A for the absorption inside the channel, i.e., by division with the bi-exponential fit Φ_p^{fit}. The intensity leaving through the side face shows strong modulations with Δz. The modulations are not only a redistribution of intensity to different angles θ_f but also visible as small oscillations in the radiant flux Φ_p (cf. Fig. 2.5B). Fig. 2.11 shows Φ_p divided by Φ_p^{fit} to highlight these oscillations for different integration ranges in θ_f. For angles of $|\theta_f| \geq 4$ mrad, Fano-like intensity modulations are visible. In Fig. 2.12, similar measurements are shown for characteristic *Ni*-K radiation excited in the cladding of the *Fe/Ni* multiwaveguide system for experimental and simulated data.

Last, we show that the observed effects of electron impact X-ray generation in waveguides are not limited to characteristic radiation but also change the phase-space distribution for bremsstrahlung. To this end, we inspected energy dispersive data of the SDD detector for the *Fe/Ni* multiwaveguide system excited with electron bombardment. The energy resolved intensity map $I(\theta_f, E)$ (Fig. 2.6) shows the characteristic *Fe* and *Ni* radiation as horizontal lines, with local maxima at the external angles of the waveguide modes. In between these horizontal lines the bremsstrahlung background shows the same local maxima, all lying on hyperbolic functions, which describe the external angles of the waveguide modes as a function of E (see inset in Fig. 2.6). This shows that not only characteristic radiation but also the bremsstrahlung continuum is directly emitted into the waveguide modes.

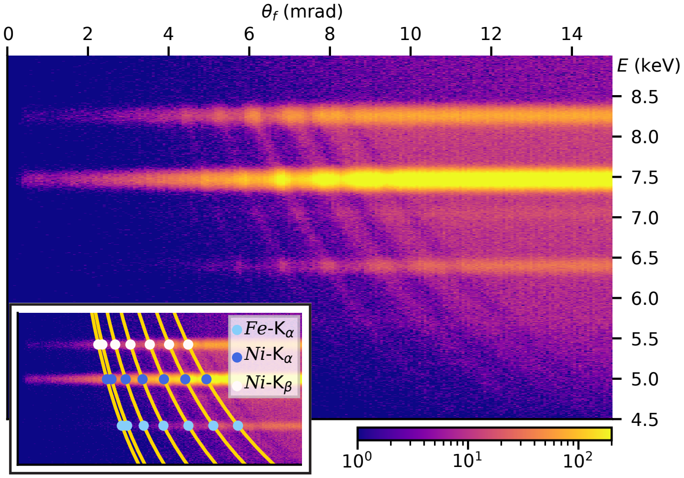

Fig. 2.6: *e*-beam excited characteristic and bremsstrahlung radiation in the *Fe/Ni* multiwaveguide system. The X-ray spectrum is measured with the SDD detector as a function of exit angle θ_f. The mode pattern for each of the characteristic emission lines—*Fe*-K$_\alpha$, *Fe*-K$_\beta$, *Ni*-K$_\alpha$ and *Ni*-K$_\beta$—is observed as horizontal lines with the local maxima at the angles of the waveguide modes. The bremsstrahlung background in between the horizontal lines of characteristic radiation also shows the modulation of the waveguide's mode pattern. The inset shows the theoretical positions of the modes for the characteristic radiation (dots) and for the bremsstrahlung continuum (lines), with mode numbers $m = 0$ to 6 (from left to right). The color scales with the intensity in arbitrary units on a logarithmic scale.

2.4 Discussion

The results show that waveguide anodes affect the emission phase space of characteristic X-rays and bremsstrahlung. The far-field distribution of the emission changes with the distance between the exciting *e*-beam and the side edge of the waveguide. The observed intensity profiles are highly modulated with sharp features that are in good agreement with simulations based on finite differences and the reciprocity theorem. Notably, the angular emission profile of the fluorescence and characteristic radiation excited in the waveguide (cf. Figs. 2.4B–D and 2.5A) exhibits a Fano-like lineshape, which can be attributed to the interference of the radiation of the waveguide modes ("narrow" resonance) with fluorescence that did not couple into the waveguide (forming a "broad" background channel). The Fano lineshape parameter changes as a function of the phase shift between the two contributions with θ_f, as observed for nuclear resonant scattering [Hee+15a], giving rise to a sequence of different lineshape features: Lorentzian, inverted Lorentzian, and Fano profile with cusp/dip or dip/cusp, respectively, as described in general and in great detail in [Lim+17].

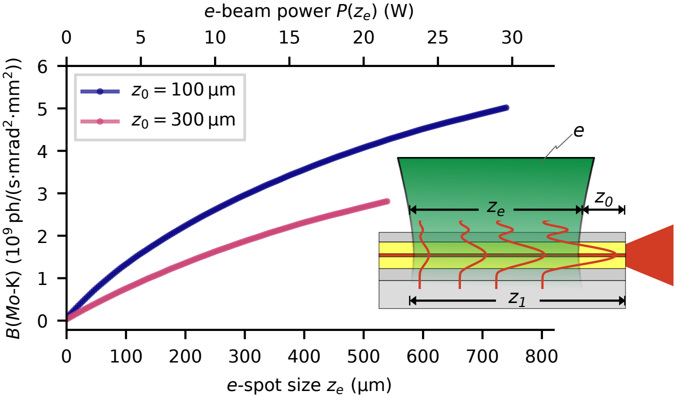

Fig. 2.7: Increasing the brilliance of the *Mo/C* waveguide with elongated *e*-beam spots. The brilliance B of the characteristic *Mo*-K radiation generated inside the *Mo/C* waveguide system can be increased substantially by expanding the *e*-beam spot on top of the waveguide along the z direction. The area power density of the *e*-beam is kept constant at the value used in the experiments $p_e = 4\,\mathrm{kW/mm^2}$. We calculated the brilliance by numerical integration of the data in Fig. 2.5B. The integration limits of the *e*-beam are from z_0 to $z_1 = z_0 + z_e$ (see inset). Note that the effective X-ray spot size of the modes leaving the waveguide through the side face does not change with a variation of z_e. The *e*-beam power $P(z_e)$ is given on the upper abscissa.

For the *Mo/C* waveguide system, we have already achieved a brightness of $B_p \approx 5 \times 10^8\,\mathrm{ph\,s^{-1}\,mrad^{-2}\,mm^{-2}\,W^{-1}}$, with an experimental setup which was not at all optimized for high brightness. We will next discuss how the brightness can be increased experimentally. For conventional X-ray sources, the effective size of the X-ray source spot is directly proportional to the size of the *e*-beam. However, the source spot of the radiation generated in an X-ray waveguide and leaving the waveguide through the side face does not depend on the size of the *e*-beam in the z direction, but only on the waveguide's geometry. Hence, an elongation of the *e*-beam along z with constant area power density will increase the radiant flux without increase of the effective X-ray source spot and hence will directly benefit brilliance. We have calculated this brilliance increase for the *Mo/C* waveguide. To this end, we numerically integrated the brilliance $B_p(\Delta z)$ shown in Fig. 2.5B for a given range of Δz. Fig. 2.7 shows the resulting brilliance. Note that the area power density does not change with increasing *e*-beam size z_e. For $z_e = 700\,\mu\text{m}$, we obtain a *Mo*-K brilliance of $B \approx 5 \times 10^9\,\text{ph}\,\text{s}^{-1}\,\text{mrad}^{-2}\,\text{mm}^{-2}$ at an area power density of $4\,\text{kW}\,\text{mm}^{-2}$ of the *e*-beam. This area power density was chosen to be deliberately low to not saturate the MÖNCH detector (a flux as low as $\sim$ 1 photon per 100 pixel and frame is required for energy-resolved detection) and is substantially lower than the damage threshold. With proper heat management, a two orders of magnitude higher power density could be applied to the waveguide target, resulting in a brilliance increase to $B \approx 5 \times 10^{11}\,\text{ph}\,\text{s}^{-1}\,\text{mrad}^{-2}\,\text{mm}^{-2}$. To increase heat dissipation, the *Si* substrate of the waveguides could easily be replaced by diamond wafers with substantial increase in heat conductivity.

Next, we discuss the changes in emission, when an atom is placed in a waveguide resonator. Fig. 2.5B indicates that a variation of Δz substantially changes the far-field distribution of the radiation emitted through the side face of the waveguide. Apart from damping due to mode propagation, small oscillations are observed, which do not vanish after integrating the intensity spectrum along θ_f (cf. Fig. 2.11 for a detailed presentation). Together with the rich interference profiles as a function of angle and position in the resonator, this supports the view that the emission process itself is already modified by the emitter position in the cavity. This is conceptually similar to the emission of Mössbauer atoms in thin film structures, which have already been described successfully in the framework of cavity quantum electrodynamics (CQED) [Len+20]. Hence, the Purcell effect describing the enhancement of the spontaneous photon emission of atoms in a cavity is the natural starting point for this problem. For a 3d cavity, the enhancement factor with respect to free space emission is given by [Pur46]

$$F_P = \frac{3}{4\pi^2}\left(\frac{\lambda}{n}\right)^3 \frac{Q}{V},$$

where Q is the quality factor of the resonator, V is the modal volume, n is the index of refraction, and λ is the wavelength. Note that the Purcell effect can also be calculated on the basis of the reciprocity approach, as recently shown theoretically for emission from a source inside a resonator into an open optical system [Sch+18]. In the following, we sketch out a simple argument of how to estimate the gain factor G for a source where the anode is structured such that it supports photon emission into bound modes, for example, in the form of a planar waveguide or an array of cylindrical fibers. The metal for emission of characteristic radiation can be a component of the cladding or can be integrated into the guiding core. The simplest structure would be an array of planar waveguides deposited onto a substrate, which could be used either in transmission or in reflection (Fig. 2.8C), as it was used in this manuscript. More challenging to fabricate, but leading to a higher G, would be an array of channel waveguides (Fig. 2.8B), formed for example, by macroscopically long cylindrical holes with radius $a \simeq 50$ to 200 nm etched into a metal. Starting from Fermi's golden rule for the transition rate of spontaneous emission into just one waveguide mode $W_{if} = 2\pi/\hbar|H_{if}|^2\delta(E_i - E_f)$ with dipolar interaction $H = -\boldsymbol{\mu} \cdot \mathbf{E}$ and waveguide modes of vector potential with magnitude $A_m = c_m \exp(i\beta_m z)\psi_m(\boldsymbol{r}_\perp)$, the quantized field of the cavity mode becomes [Tum+09; DGK96]

$$\mathbf{E}(\boldsymbol{r}_\perp, t) = \sum_m \sqrt{\frac{\hbar\omega_m}{2}} \left(ia_m e^{-i\omega t}\mathbf{A}_m(\boldsymbol{r}_\perp) - ia_m^\dagger e^{i\omega t}\mathbf{A}_m^*(\boldsymbol{r}_\perp)\right).$$

We now consider the shape function of the guided mode $\psi_m(\boldsymbol{r}_\perp)$ in such a (planar or channel) waveguide. The mode intensity distribution $I_m \propto |\psi_m|^2$ has a width Δ that is smaller than the guiding channel cross section a because of the mode confinement but is on the same order. The modes are orthogonal and normalized

$$\int d\boldsymbol{r}_\perp \; \psi_m(\boldsymbol{r}_\perp)\psi_n^*(\boldsymbol{r}_\perp) = \delta_{nm} \; ,$$

where the integral is in the plane orthogonal to the optical axis. At the waveguide exit, the mode propagates (diffracts) into free space with a divergence given by $\theta = c_a \; \lambda/\Delta$, where the prefactor c_a depends on the exact functional shape of the mode. θ can, of course, also be regarded as a numerical aperture, and Δ can be regarded as a resolution-defining beam confinement. Let the guiding core (or cladding) contain atoms in an excited state, for example, due to K-shell ionization following electron impact, and hence be a source of X-ray emission. Since the mode density differs from free space, the emission rate of X-ray photons is modified by the cavity. Analogous to the optical case, where 1d and 2d emission into cavity modes is well established [Jun+09], we can also use the Purcell factor here, generalized from 3d cavities to one- and two-dimensional resonators and set $n \simeq 1$ for hard X-rays. The enhancement factor for spontaneous emission into an X-ray waveguide mode then becomes [Tum+09]

$$\begin{aligned}
\text{1d: } F_{1d} &= \frac{\lambda}{4} \, \frac{Q_{\text{planar}}}{d_{\text{eff}}} \, , \\
\text{2d: } F_{2d} &= \frac{1}{\pi} \left(\frac{\lambda}{2}\right)^2 \frac{Q_{\text{channel}}}{A_{\text{eff}}} \, ,
\end{aligned}$$

for planar and channel waveguides, respectively. Here, Q is the quality factor of the cavity mode, which can be calculated for a leaky cavity by numerical field propagation based on the reciprocity relation. For this purpose, one computes the field intensity enhancement in the resonator, when a free-space solution impinges onto the resonator from infinity with suitable boundary conditions and under angles fulfilling the resonance condition. While plane wave solutions are used for the planar case, Bessel functions are suitable for the cylindrical waveguides, yielding typical values in the range of $Q_{\text{planar}} \simeq 10^1$ to 10^2, and $Q_{\text{channel}} \simeq 10^2$ to 10^4, depending on the parameters; see also [Bro95] for calculations of Q in the analog case of optical waveguides. The effective confinement d_{eff} and A_{eff} is obtained from the mode intensity distribution $|\psi|^2$ and hence is approximately the width $\Delta < a$ of the mode. For the typical mode confinement of hard X-ray waveguides we always have $(\lambda/a) \leq 10^{-2}$, so that emission into free space completely dominates the emission into the mode. However, compared to the photons emitted into the particular solid angle Ω_θ of the mode in the absence of the waveguide, we still can have a substantial gain, namely

$$G_{\text{planar}} = F_{1d} \, \frac{4\pi}{2\pi\,\theta} = \frac{1}{2c_a} \, Q_{\text{planar}} \, \frac{\Delta}{d_{\text{eff}}} = c_m \, Q_{\text{planar}} \, ,$$

with unitless mode-specific prefactor $c_m = \Delta/(2c_a d_{\text{eff}})$. For a channel waveguide, we obtain the same relation with the corresponding Q factor and $c_m = \Delta^2/(c_a^2 A_{\text{eff}})$. Since $\Delta \approx d_{\text{eff}}$, the value of c_m is of order $O(1)$ and can be determined from precise numerical calculations, which can also take the distribution of the metal source atoms into account. As we see, the gain in the directional brilliance of the source, i.e., the brilliance measured when only the far-field radiation cone of the mode is evaluated, is essentially given by the quality factor of the waveguide; hence, $G \simeq Q$.

Last, we discuss the experimental Q factor of the waveguide resonators in the current work. Starting from the definition $Q = 2\pi E_0/E_{\text{L}}$, where E_0 denotes the stored energy and E_{L} denotes the lost energy per cycle in the waveguide resonator, we have to consider the exponential decay of the waveguide's exit intensity, as the generating *e*-beam is moved away from the edge, i.e., the curve measured in Fig. 2.5B. Expressed in number of cycles n_{c}, where a cycle is defined by one period of the internal total reflection of the guided beams, we can write for the stored energy in the resonator $E_S = E_0 e^{-\mu n_{\text{c}}}$. Hence, $Q = 2\pi/\mu = 2\pi z_{1/e}/(2\Delta l)$, with $z_{1/e}$ as the $1/e$-length of the decay and Δl as the distance between two consecutive reflections, calculated from the internal mode propagation angle θ_{int} and the effective width of the waveguide mode D_{eff}. With θ_{int} given by Snell's law and the external angle of the mode calculated from the Parratt formalism, Q can be directly computed from the measured $z_{1/e}$.

From the bi-exponential fit in Fig. 2.5B, we obtain $z_{1/e} = 622(11)\,\mu\mathrm{m}$ and $z_{1/e} = 82(2)\,\mu\mathrm{m}$, for the 0th and 1st mode, respectively, and hence $Q_0 = 64(2)$ and $Q_1 = 11.0(3)$. The experimentally determined values for $z_{1/e}$ also indicate that a much higher photon number could have coupled into the waveguide mode by expanding the *e*-beam, while keeping the X-ray source size constant. The width of the *e*-beam could be increased to the measured modal decay length $z_{1/e}$ (see Figs. 2.7 and 2.5). However, at the current setup, increasing the beam size and beam power was not possible for reasons of *e*-beam optics. Furthermore, it would have resulted in detector saturation. Conversely, a correspondingly upgraded experimental setup would directly result in the corresponding brilliance gain as shown in Fig. 2.7.

2.5 Summary and Outlook

We showed the direct emission of spontaneous X-rays into waveguide modes, as a manifestation of the Purcell effect. As a result of this work, we demonstrated a novel X-ray source concept based on X-ray photon emission directly into X-ray waveguide modes. Instead of first generating a beam in an X-ray tube and then coupling it into an optic, photons are generated directly in a structured anode target, forming an X-ray waveguide or waveguide array. The metal for emission of characteristic radiation can be a component of the cladding or can be integrated into the guiding core. The simplest such structure is an array of planar waveguides deposited onto a substrate, which can be used either in reflection geometry, as was done in this work, or in transmission geometry (see Figs. 2.8B–C). If the geometry is properly chosen, then the size of the effective X-ray source spot does not depend on the *e*-beam spot size for the generation of X-rays in table-top sources with waveguide anodes. This observation results in an estimated brilliance of $B \simeq 5 \times 10^{11}\,\mathrm{ph\,s^{-1}\,mrad^{-2}\,mm^{-2}}$ for a ”fully filled” cavity (Fig. 2.7), operated at the presumed power threshold for solid targets. This will require a suitable heat management. Two-dimensional waveguide cavities could be realized by an array of channel waveguides, formed for example by macroscopically long cylindrical holes with radius $a \simeq 50$ to 200 nm etched into a metal. For these waveguide channels the mode density calculations yield even higher mode densities and Q factors in the range of 10^2 to 10^4, depending on photon energy, optical constants of the materials and geometric parameters. Directed emission of characteristic radiation and bremsstrahlung into waveguide modes along with an associated increase of spatial coherence in the corresponding angular cone could greatly benefit applications such as coherent imaging without synchrotron radiation.

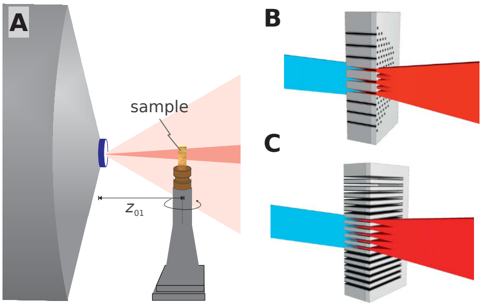

Fig. 2.8: X-ray source based on direct emission into waveguide modes. (A) A source can, for example, be realized by exchanging the conventional diamond-supported *W* layer in transmission targets with a diamond-supported waveguide structure. The waveguide anode emits into a narrow radiation cone (dark red) with increased brilliance in comparison to the emission cone of a conventional anode (light red). The diamond forms the vacuum window and, at the same time, supports the waveguide structure, which can consist of cylindrical **(B)** or planar guides **(C)**.

2.6 Methods

2.6.1 Waveguide structures

In this work, we used three different waveguide systems (cf. Table 2.1). Two systems (*Fe/Ni*, and *Mo/C* multiwaveguides) were fabricated by magnetron sputtering by *Incoatec GmbH* (Geesthacht, Germany). The *Fe/Ni* system consists of 50 waveguides each with layer sequence of [*Ni* (10 nm)/*C* (24.5 nm)/*Fe* (1 nm)/*C* (24.5 nm)] deposited on a buffer layer of 30 nm *Ni*. The *Mo/C* system consists of 30 waveguides each with a layer sequence of [*Mo* (25 nm)/*C* (16 nm)/*Mo* (1 nm)/ *C* (16 nm)] deposited on a layer of 30 nm *Mo* and an additional 10 nm thick buffer layer of *Cr*. Both systems were deposited on a 3 mm thick *Si* substrate. The third waveguide system is a single waveguide *Co/Cu* system fabricated by pulsed laser deposition. The exact layer sequence is [*Cu* (5 nm)/*C* (20 nm)/*Co* (2 nm)/*C* (20 nm)/*Cu* (40 nm)] on 1 mm thick *Si* substrate. The *Mo/C* and the *Fe/Ni* system were diced by a wafer saw (DAD321, DISCO, Tokyo, Japan); the *Co/Cu* waveguide was cut by scribe and break with a diamond tip. No further processing was done to the edges of the samples.

2.6.2 Cavity modes excited by synchrotron radiation

The experiments with synchrotron radiation were carried out at the `GINIX` endstation [Sal+15b] of the beamline P10 at the PETRAIII storage ring (DESY, Hamburg, Germany). The schematic of the experimental setup is shown in Fig. 2.1B. The 8 keV synchrotron beam was focused by a Kirkpatrick-Baez mirror system to about 500 nm $\times$ 350 nm [horizontal $\times$ vertical (h $\times$ v)], with a divergence of 1.6 mrad $\times$ 1.0 mrad (h $\times$ v). Instead of the SDD detector and an entrance slit (Fig. 2.1A), we used the hybrid pixel area detector MÖNCH (see below) for the X-ray detection. The detector was placed at 90° to the incoming synchrotron beam. The distance between primary beam and detector was 200 mm. We used an interpolation factor of 5, resulting in a pixel size of 5 µm. Hence, the angular resolution $\Delta\theta_f$ of the observation angle θ_f is 25 µrad. The energy resolution of about 1 keV was sufficient to separate fluorescence and primary radiation, whereas it was not sufficient to separate K_α and K_β radiation. We used this setup in combination with the *Co/Cu* waveguide (cf. Fig. 2.10) and the *Fe/Ni* system (cf. Fig. 2.4). The angle of grazing incidence θ_{in} of the synchrotron beam was 4.1 mrad for the *Co/Cu* and 7.6 mrad for the *Fe/Ni* waveguide. Note that in both systems with 8 keV primary radiation only the central ∂-layer (*Co* and *Fe*) was excited, whereas the K-edge of the cladding material (*Cu* and *Ni*) is above the excitation energy.

2.6.3 Cavity modes excited at a µ-focus X-ray source

We used a liquid-metal jet µ-focus X-ray source (MetalJet D2, *Excillum AB*, Kista, Sweden) with Galinstan anode, operated at 70 kV acceleration voltage, a total power of 60 W, and an electron spot size of 6 µm $\times$ 10 µm (h $\times$ v). The primary beam was focused by a Montel multilayer optic (ELM43GA, *Incoatec GmbH*, Geesthacht, Germany) to a spot size of 100 µm and a divergence of 7.5 mrad. The reflection of the focusing optic is optimized for the *Ga*-K_α radiation. A schematic of the setup is shown in Fig. 2.1B. The SDD detector (see below) was placed at 90° toward the primary beam. The distance between the detection entrance slit and the primary beam was 200 mm. The width of the entrance slit was $\Delta y = 50$ µm, resulting in an angular resolution $\Delta\theta_f$ of the observation angle θ_f of 250 µrad. We used the *Co/Cu* waveguide at this setup (cf. Fig. 2.3). In this experiment the incoming *Ga*-K_α radiation excites fluorescence in both the *Co* ∂-layer and the *Cu* cladding.

2.6.4 Cavity modes excited with electron impact

We used the electron gun and electron optics of a μ-focus X-ray source (R5 liquid-metal jet prototype, *Excillum AB*, Kista, Sweden) with a customized anode chamber design. The chamber enables the mounting of planar waveguide structures as anode with orthogonal electron impact onto the top surface of the waveguide. The *e*-beam was scanned along the waveguide's surface by the deflection coils of the electron optics. The following settings were used:

***Co/Cu* waveguide:** 35 kV acceleration voltage, 450 mW *e*-beam power, SDD detector with 100 μm entrance slit, 350 mm source to detector-slit distance, $\Delta\theta_f \approx$ 285 μrad angular resolution of detection angle, and 40 s exposure time (cf. Fig. 2.3).

***Fe/Ni* waveguide (SDD detector):** 15 kV acceleration voltage, 450 mW *e*-beam power, SDD detector with 50 μm entrance slit, 370 mm source to detector-slit distance, $\Delta\theta_f \approx$ 270 μrad angular resolution of detection angle, and 10 s exposure time (cf. Fig. 2.6).

***Fe/Ni* waveguide (MÖNCH detector):** 15 kV acceleration voltage, 450 mW *e*-beam power, MÖNCH detector, 165 mm source to detector distance, 25 μm physical pixel size, 5 μm interpolated pixel size (5× interpolation), $\Delta\theta_f \approx$ 30.3 μrad angular resolution of detection angle, 1 ms exposure time per frame and 500,000 frames per *e*-beam position. A 20 μm thick steel foil was used as chromatic filter (cf. Fig. 2.12).

***Mo/C* waveguide:** 50 kV acceleration voltage, 400 mW *e*-beam power, MÖNCH detector, 250 mm source to detector distance, 25 μm physical pixel size, 6.25 μm interpolated pixel size (4× interpolation), $\Delta\theta_f \approx$ 25 μrad angular resolution of detection angle, 1 ms exposure time per frame, and 500,000 frames per *e*-beam position. A 35 μm thick *Ag* foil was used as chromatic filter, to increase the contrast between the *Mo*-K_α/K_β radiation and the bremsstrahlung's background (cf. Fig. 2.5).

2.6.5 Energy width and finesse (*Mo/C* waveguide)

For the *Mo/C* waveguide, we can calculate the energy width (FWHM) of the m-th resonant mode with photon energy E as $\delta E_m = \frac{E}{Q_m}$. With the previously determined Q factors for the 0th and 1st mode [$Q_0 = 64(2)$ and $Q_1 = 11.0(3)$], we get $\delta E_0 = 0.273(5)$ keV and $\delta E_1 = 1.60(4)$ keV. The energy linewidth (FWHM) of the characteristic *Mo*-K_α and K_β radiation is between 6 and 7 eV [Men+19]. The finesse of the waveguide is given by [Pas08]

$$F = \frac{\pi}{2\arcsin\left(\frac{1-\sqrt{\rho}}{2\sqrt[4]{\rho}}\right)},$$

where ρ is the fraction of energy stored in the resonator after one full cycle. With $Q = 2\pi/\mu$ and $1/\mu$ as the number of cycles, where the fraction of energy in the resonator drops to $1/e$, we get $\rho = \exp(-\mu)$. Hence, the finesse is $F_0 = 65(2)$ and $F_1 \approx 11(1)$ for the 0th and 1st mode, respectively.

2.6.6 Detectors

We used two different detectors, an SDD and a hybrid-pixel area detector. The SDD detector (AXAS-M1 H50-139V, *KETEK GmbH*, Munich, Germany) has a single pixel with a detection area of 65 mm^2, 450 µm sensor thickness and a built-in 100 mm long multilayer collimator. The energy resolution is specified to be 139 eV (FWHM) at 5.9 keV. To increase the angular resolution of the SDD detector, we used slit blades in front of the built-in collimator. We mounted the detector on a motorized stepper stage enabling the acquisition of angular dependent intensity measurements.

As a second detector, we used the MÖNCH03 prototype detector [Ram+17], developed at the Paul Scherrer Institute (Villigen, Switzerland). The MÖNCH is a charge-integrating hybrid-pixel area detector with 25 µm physical pixel size and a number of 400×400 pixels. By counting single photon events within an area of 3×3 pixels, we are able to access the deposited charge distribution of each individual photon. This enabled the calculation of the photon energy, which is proportional to the deposited charge and to interpolate the exact photon hit position with subpixel accuracy [Car+14]. In this work, we used an interpolation factor of 5, resulting in an interpolated pixel size of 5 µm. The theoretical energy resolution is 0.85 keV, in this experiment we observed an energy resolution of about 1 keV (FWHM).

2.6.7 Calculation of radiant flux and brilliance

We calculated the radiant flux of the *Co/Cu* waveguide (cf. Figs. 2.3 and 2.9) from the photon counts of the SDD detector. The air absorption of the path between source and detector is corrected, with a transmission of about 55 % for *Co*-K$_\alpha$, 64 % for *Co*-K$_\beta$ and 66 % for *Cu*-K$_\alpha$ [Sch+11]. The solid angle of the detector is given by the detection area 0.8 mm^2 (slit gap × sensor width) and the source-to-detector distance (350 mm).

The *Mo*-K radiant flux Φ_p and brilliance B_p of the *Mo/C* waveguide (cf. Fig. 2.5) are calculated from the registered photon counts on the MÖNCH detector. The counts are corrected by the absorption of the 35 µm thick *Ag* filter, with a transmission of about 38 % at 17.5 keV [Sch+11]. Furthermore, the absorption cross section of the 300 µm thick *Si* sensor of the MÖNCH is corrected. The absorption of the sensor is about 37 % at 17.5 keV [Sch+11]. The solid angle of a single pixel is given by the pixel size and source-to-detector distance. For the calculation of the source brilliance B_p exiting through the truncated side face of the *Mo/C* multiwaveguide system, we estimated the effective X-ray source spot size to be given by the guiding layer thickness times the number of waveguides 33 nm $\times$ 30 in the y direction and the spot size of the *e*-beam (10 µm, FWHM) in the lateral direction. Hence, the size of the effective X-ray source spot is $A_{\text{source}} \approx 9.9\,\mu\text{m}^2$.

2.6.8 Finite-difference simulation

We used PyPropagate [MS17] for simulating the propagation of the electromagnetic field inside the waveguide cavities. The angular-dependent intensity maps were calculated using the reciprocity theorem (cf. Fig. 2.2). Hence, we used PyPropagate to calculate the internal field inside the waveguide at a given position $I_{\theta_{\text{PW}}}(y, \Delta z)$ for different angles of plane wave incidence θ_{PW}. According to the reciprocity theorem, these intensities correspond to the observed angular intensity distribution if a molecule emits photons at the given position $(y, \Delta z)$.

Acknowledgements: We thank Sarah Hoffmann-Urlaub for preparation of the thin film sample by pulsed laser deposition, Anna Bergamaschi and Sabina Chiriotti for letting us use the MÖNCH detector and for advice on its use, Markus Osterhoff and Leon M. Lohse for help in implementing the detection scheme. Funding: We acknowledge funding by the Max Planck School of Photonics supported by BMBF, Max Planck Society, and Fraunhofer Society.

Author contributions: Both authors designed research together; In-house experiments were carried out by M.V.; synchrotron experiments were carried out by both authors. M.V. performed data analysis and simulation in close discussion and interaction with T.S.. Both authors wrote the manuscript.

Competing interests: All authors declare that they have no competing interests. M.V. and T.S. are inventors on a pending patent related to this work filed by Georg-August-Universität Göttingen (no. DE10 2020 109 906.1, filed April 2020). The authors declare that they have no other competing interests

Data and materials availability All data needed to evaluate the conclusions in the paper are present in the paper and/or the Supplementary Materials. Additional data related to this paper may be requested from the authors.

2.7 Supplementary figures

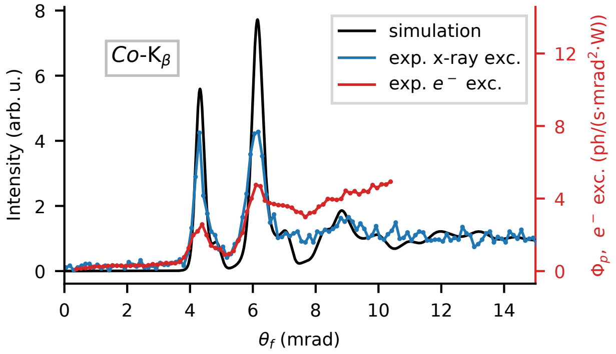

Fig. 2.9: Characteristic radiation in the *Co/Cu* waveguide. Far-field intensity of the characteristic *Co*-K$_\beta$ line, exhibiting modal peaks as a function of angle θ_f with respect to the waveguide horizon. Intensities measured with an SDD detector excited with electron impact and, for comparison, fluorescence excited with an laboratory X-ray tube. The right ordinate shows the K$_\beta$ radiant flux Φ_p per e-beam power for the e-beam excited characteristic radiation. Peak positions match the simulated X-ray generation in the waveguide.

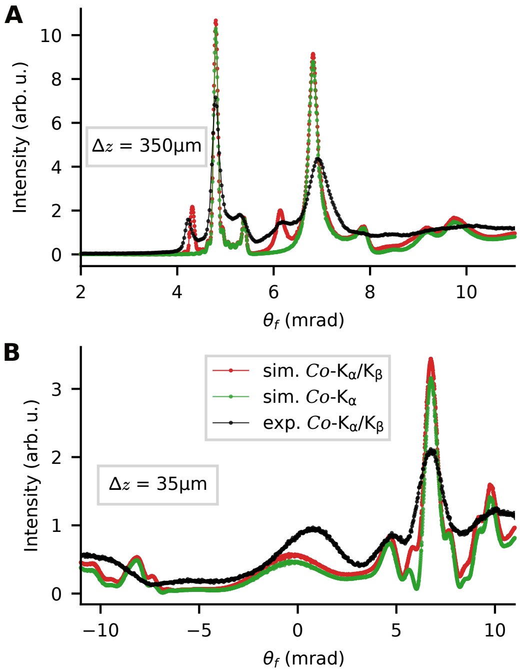

Fig. 2.10: X-ray excited fluorescence in the *Co/Cu* waveguide. Far-field intensity of the *Co*-K fluorescence lines, exhibiting modal peaks as a function of angle θ_f with respect to the waveguide horizon. The intensities are measured with the MÖNCH detector at the synchrotron for the distances $\Delta z = 350\,\mu\text{m}$ **(A)** and 35 µm **(B)** to the waveguide edge. Peak positions match the simulated X-ray generation in the waveguide for a superposition of *Co*-K_α and K_β radiation.

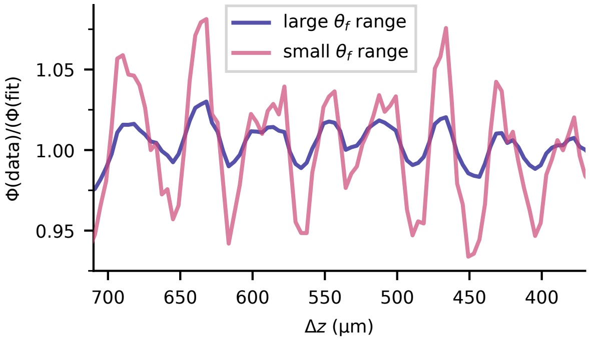

Fig. 2.11: Intensity modulations when moving the *e*-beam along Δz. Radiant flux Φ of the *Mo/C* waveguide system divided by the bi-exponential fit (cf. Fig. 2.5). The data show modulations of Φ by about 5 % for an angular range of θ_f from −2.9 to 2.9 mrad (small θ_f range, corresponding to the green rectangle shown in Fig. 2.5) and of about 1–2 % for an angular range θ_f from −7.1 to 7.1 mrad (large θ_f range). For the larger θ_f range the signal was corrected for background variations for better visibility of the modulations.

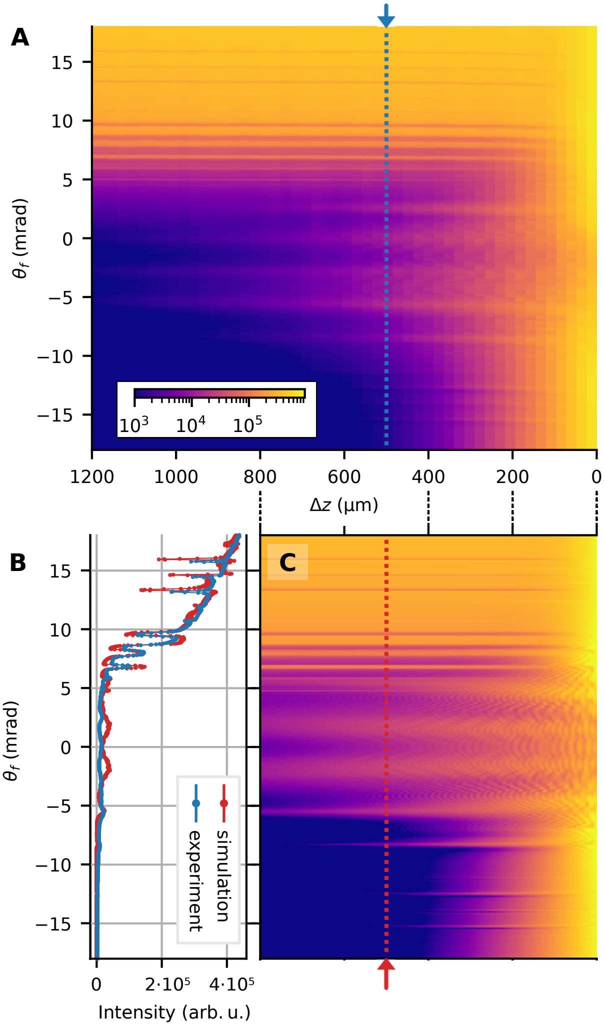

Fig. 2.12: Characteristic *Ni*-K radiation in the *Fe/Ni* multiwaveguide system. **(A)** Measured characteristic *Ni*-K radiation $I_{Ni}(\theta_f, \Delta z)$ excited in the *Ni* cladding layers for different *e*-beam positions Δz and observation angles θ_f. **(B)** *Ni*-K intensity for $\Delta z = 500\,\mu\text{m}$ for measured data (blue) and simulated data (red). **(C)** Simulated *Ni* intensity map $I_{Ni}(\theta_f, \Delta z)$. For the measurements, a 20 µm-thick steel foil was used as chromatic filter. The color scales with the intensity in arbitrary units on a logarithmic scale.

Pump-probe X-ray holographic imaging of laser-induced cavitation bubbles with femto-second FEL pulses

3

M. VASSHOLZ, H. P. HOEPPE, J. HAGEMANN, J. M. ROSSELLÓ, M. OSTERHOFF, R. METTIN, T. KURZ, A. SCHROPP, F. SEIBOTH, C. G. SCHROER, M. SCHOLZ, J. MÖLLER, J. HALLMANN, U. BOESENBERG, C. KIM, A. ZOZULYA, W. LU, R. SHAYDUK, R. SCHAFFER, A. MADSEN, T. SALDITT

*reproduced[1] from Nature Communications **12**, 3468 (2021)* [Vas+21]

Cavitation bubbles can be seeded from a plasma following optical breakdown, by focusing an intense laser in water. The fast dynamics are associated with extreme states of gas and liquid, especially in the nascent state. This offers a unique setting to probe water and water vapor far-from equilibrium. However, current optical techniques cannot quantify these early states due to contrast and resolution limitations. X-ray holography with single X-ray free-electron laser pulses has now enabled a quasi-instantaneous high resolution structural probe with contrast proportional to the electron density of the object. In this work we demonstrate cone-beam holographic flash imaging of laser-induced cavitation bubbles in water with nanofocused X-ray free-electron laser pulses. We quantify the spatial and temporal pressure distribution of the shockwave surrounding the expanding cavitation bubble at time delays shortly after seeding and compare the results to numerical simulations.

---

[1] Subject to minor corrections.

3.1 Introduction

Small transient or strongly driven cavitation bubbles in liquids exhibit a wide range of interesting nonlinear effects. They can experience violent collapse [LK10; BHL02], which is associated with shockwave emission into the liquid, high compression, heating of the bubble medium, light emission (sonoluminescence) or chemical reactions. In the vicinity of a solid surface or interface they can form liquid jets, resulting in erosion of the material. In ultrasonically driven multi-bubble systems (acoustic cavitation) [CM17], the mutual interaction of bubbles and their interaction with the sound field can lead to structure formation and collective behavior. Apart from fundamental aspects of non-equilibrium physics, these processes are relevant for a range of medical procedures, for example to emulsify tissue in cataract surgery [Bre15] or bubble-mediated drug delivery [Lip+18]. The understanding of cavitation bubbles and dynamics is important as well for sonochemistry, ultrasonic cleaning and corrosion prevention. For well-controlled experiments on cavitation bubbles, short laser pulses are commonly used, which seed cavitation bubbles by the transition from a laser-generated plasma to a hot, compressed bubble nucleus, and finally to an expanding gas and vapour bubble in the liquid environment. This transition from the plasma to a bubble, the plasma growth, subsequent cooling of the plasma and generation of shockwaves in the medium, as well as the precise states of matter in the bubble remain elusive. For several decades, the main tools to study cavitation dynamics have been acoustic methods, optical pump-probe spectroscopy [Vog+99] and optical imaging [Lau72], with up to 100 million frames per second by high-speed ICCD cameras [LL03]. Increasing sensitivity of optical sensors has more recently allowed for direct imaging of bubble oscillations and sonoluminescence light emission in multi-bubble fields [CM17]. Likewise, the initial bubble formation and shockwave emission after dielectric breakdown was measured with acoustical methods and optical methods, such as bright and dark field imaging, optical interferometry, Schlieren photography, and streak imaging [VBP96; Tok+09; Tag+16; Vey+16; Vey+18; Hay+16; Sin+19; Kim+20c]. However, due to the small scales and the fast dynamics, imaging of the bubble interior and its close environment during dielectric breakdown and collapse still poses unmet challenges. Optical methods are limited by the numerical aperture of long-distance objectives, required to image cavitation bubbles sufficiently far from interfaces. Sub-nanosecond time resolution and sub-micrometer spatial resolution are required to follow the motion of the phase boundary and the dynamics of the bubble interior. In the absence of direct imaging methods, knowledge of the collapsed bubble state has been inferred from spectroscopic measurements of the emitted light [FS05], and has been based on model calculations [MCY97; WR93; Sch+12; VSY99]. Several models have been developed to describe the nonlinear phenomenon of dielectric breakdown in liquids and the following cavitation dynamics [Sac91; Vog+96; NV96; KHR97; CGV97; NV99]. However, many aspects of the dynamical evolution of the bubble and the structure of the phase boundary remain unclear. Open questions relate to e.g. the presence of inhomogeneities, the existence of converging shocks, and even more fundamentally to the exact spatial density and pressure profile of the bubble and the surrounding shockwave in different states.

In this work we demonstrate near-field holographic imaging of cavitation bubbles with single X-ray free-electron laser (XFEL) pulses. This experimental approach offers a quasi-instantaneous high resolution structural probe at different stages after seeding, particularly useful to investigate extreme states of bubble generation and collapse. The method offers higher resolution and penetration depth than ultra-fast optical microscopy, and importantly a unique direct sensitivity to the electron density profile, which is not accessible by the aforementioned optical methods. Such experimental data are required to assess the validity and limits of current numerical models and theoretical hypotheses and improve our basic physical understanding of these processes. More generally, near-field X-ray holography with nano-focused single FEL pulses is a promising tool to study driven condensed matter and warm dense matter. Cone beam holography with XFEL pulses was previously used to image shockwave propagation in diamond [Sch+15]. In contrast to the shockwave propagation in solids, we image the dynamics of complex phase transitions in liquid water after dielectric breakdown, with higher geometrical complexity. Compared to the recently demonstrated X-ray microscopy of laser-induced dynamic processes with parallel beam optics [Ibr+15; Vag+19] or an incoherent plasma X-ray source [Ant+19], the present method offers higher spatial resolution and sensitivity, not limited by the detector pixel size. We have measured micrometer-sized cavitation bubbles in a pump-probe imaging scheme with single XFEL pulses. For a quantitative analysis, we have developed a high-throughput workflow of the geometrically magnified near-field holograms. To this end, we introduce a phase retrieval approach, which makes use of the radial symmetry of the cavitation bubbles. With this analysis, the three dimensional (3d) mass-density distribution of the bubble's interior, of the interface between bubble and shockwave, as well as of the shockwave surrounding the cavitation bubble is obtained at a spatial sampling of about 100 nm pixel size and a temporal resolution of a few nanoseconds, only limited by the pulse duration of the pump laser. The density profiles allow to extract the 3d-pressure distribution of individual shockwaves in space and time in close proximity to the cavitation center. This pressure distribution is not accessible with other methods. Optical methods only measure a single pressure value directly at the shockfront [VBP96], leaving the pressure distribution in between bubble and shockfront unknown. Hydrophones for acoustic methods cannot be placed in close proximity to the cavitation center. We compare the measured pressure distribution with simulations based on the commonly used Gilmore-Akulichev model for cavitation [Gil52]. In total, density and pressure distributions are evaluated for more than 3000 individual cavitation events, which can then be used to compute histograms of physical properties beyond simple ensemble averages.

3.2 Results

3.2.1 Instrumentation and implementation

To observe cavitation dynamics with X-ray near-field holography (NFH), an infrared (IR) laser-pump and X-ray-probe scheme is employed. The main components of the experimental setup (Fig. 3.1a) are the focusing optics of the X-ray beam, a pulsed IR laser generating cavitation inside a water-filled cuvette and an X-ray camera recording the X-ray holograms. The experiment is performed at the MID (Materials Imaging and Dynamics) instrument [Mad+21; Tsc+17] of the European XFEL [Alt+06]. The XFEL provides ultra-short X-ray pulses on the order of 100 fs, or less, with a photon energy of 14 keV at a repetition rate of 10 Hz and 3×10^{11} photons in average per pulse. X-rays are focused with a set of Beryllium compound refractive lenses to a focal spot size of ~78 nm (calculated full width at half maximum, FWHM) [BS19]. A focused IR laser with wavelength 1064 nm, numerical aperture 0.2, 6 ns pulse duration and 24 mJ pulse energy, excites cavitation events inside a water-filled cuvette. The cuvette is placed in a distance of $z_{01} = 144$ mm behind the X-ray focus. The holographic contrast is formed by free-space propagation towards the scintillator-based (LuAg:Ce, thickness 20 µm) X-ray camera positioned at a distance of $z_{02} = 9578$ mm behind the X-ray focus. The geometric magnification of $M \approx 66.5$ yields an effective pixel size in the sample plane of $d_{\text{eff}} = 98$ nm and a Fresnel number of $F = 7.6 \times 10^{-4}$. The setup is operated in air, but an 8 m long evacuated flight tube between the setup and X-ray camera reduces absorption losses. The X-ray data is complemented with additional measurements. A high-speed (HS) optical camera observes the cavitation process simultaneously to the X-rays (Fig. 3.1a, c). The acoustic signal of the cavitation events is recorded by a piezo-ceramic microphone glued to a wall of the cuvette. The following measurement scheme is operated with 10 Hz repetition rate (Fig. 3.1b): (i) The IR pump laser shoots into the water-filled cuvette inducing a cavitation bubble with probability η. (ii) After a time delay Δt the FEL X-ray pulse probes the excited bubble and the X-ray camera records the hologram. (iii) The HS optical camera records multiple frames, where the first frame is synchronized to the IR laser pulse to detect the plasma spark. (iv) A digital oscilloscope records the signal of the microphone. The cavitation dynamics are recorded by measurements for different time delays Δt between IR laser pump and X-ray probe (Fig. 3.1d). Details on the experimental setup and the timing scheme are given in the Methods section and in [Ost+21]. With this measurement scheme, we acquired X-ray holograms for more than 20000 individual cavitation events. To extract the quantitative phase of the cavitation bubbles from the holograms, we present a tailored phase retrieval approach for objects with radial symmetry. The phase retrieval gives access to physical quantities of the cavitation bubbles and enables to resolve the density and pressure in space and time. In the following we analyze single individual cavitation events, followed by an automated procedure to extract phase, density and pressure individually for an ensemble of over 3000 cavitation events. The automated selection was carried out based on criteria to ensure that the hologram contained a single cavitation bubble only, which did not exceed the field of view. Based on the spatial density and pressure distributions, we show how key properties of the cavitation dynamics change with the deposited laser energy. If not stated otherwise, we always refer to the shockwave generated by the dielectric breakdown rather than the shockwave emitted by the bubble collapse.

3.2.2 Phase retrieval reveals the bubble density profile

Near-field holographic X-ray imaging encodes the object's phase shift and absorption properties in intensity modulations based on self-interference of the undisturbed primary beam and its modulations by the sample. Phase retrieval denotes the process of decoding the sample's properties from the intensity measurements, i.e. the hologram. In a first pre-processing step, contributions of an imperfect illuminating wavefront have to be identified and removed. In synchrotron experiments this is typically done by a simple empty-beam division, i.e. dividing the measured intensity with sample by the intensity of the empty beam. This approach requires stable beam properties. However, the spontaneous nature of the SASE process of FEL radiation leads to strong pulse to pulse fluctuations, including strong variations in the total intensity and pointing of

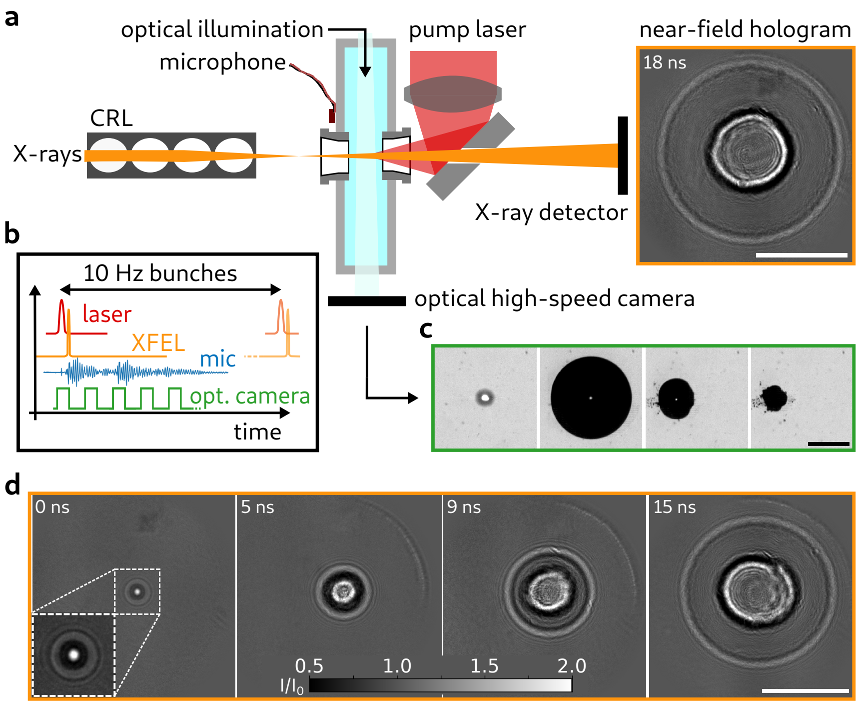

Fig. 3.1: Holographic imaging of cavitation at the MID instrument. a, The FEL X-ray pulses are focused to nanometer spot size by the beryllium CRLs. A cuvette with water is placed behind the X-ray focus. The pump laser is focused by a lens and reflected by a subsequent plane mirror into the water to seed the bubble. The X-ray and the laser beam are antiparallel. The X-ray beam passes through a small hole in the laser mirror to the X-ray detector. The distance between X-ray focus and laser focus, i.e. the seeding point of cavitation, is $z_{01} = 144\,\text{mm}$ and between X-ray focus and detector $z_{02} = 9578\,\text{mm}$. A high-speed optical camera observes the bubble formation perpendicular to the X-ray beam. A microphone at the cuvette's wall registers the acoustic signal of cavitation events. **b**, Timing scheme of the experiment. The pump laser excites a cavitation bubble at a time Δt prior to the FEL pulse. The optical high-speed camera acquires a series of images with the first frame synchronized to the pump laser pulse. The microphone signal of the acoustics is recorded (mic). **c**, Image sequence of the optical high-speed camera. The first frame (left) shows the plasma spark. The following frames have time delays of 40 µs, 140 µs and 160 µs (left to right) with respect to the first frame. **d**, Empty-beam corrected X-ray holograms of cavitation events at different times Δt, indicated in the top left corner. The holograms show strong contrast at the inner interface (gas/shockwave) and at the outer interface (shockwave/equilibrium water). Scale bars: 50 µm (a, d), 500 µm (c).

the X-ray beam, impeding empty-beam correction. To overcome these challenges, we acquire a set of single-pulse empty beams and decompose this set into its statistical contributions by a principal component analysis (PCA). The best suited linear combination of components is determined for each single-pulse hologram individually and used for empty-beam correction. This approach was initially proposed for synchrotron data [Van+15] and is described in more detail for FEL radiation in [Hag+21].

A variety of phase retrieval algorithms are available, including single step [Clo+99] and iterative approaches [Luk05; Loh+20; Hag+21]. Here, we use a phase retrieval approach, which exploits the radial symmetry of the cavitation bubbles to reduce complexity and requirements on the signal-to-noise ratio of the measured holograms. We denote this approach the Radially Fitted Phase (RFP). RFP is a forward-model approach, minimizing the difference between the measured intensity and the numerically propagated intensity of the sample's phase shift $\bar{\phi}$, as illustrated in Fig. 3.2a–c. The radial intensity $I_{\text{meas}}(R)$ is calculated by averaging over the polar angle of an empty-beam corrected and center-shifted hologram (Fig. 3.2a, b). The phase retrieval approach is formulated as an optimization problem, searching for the projected radial phase $\bar{\phi}(R)$ (Fig. 3.2c) minimizing the ℓ^2-norm between the numerically forward propagated intensity $I(\bar{\phi})$ and the measured radial intensity I_{meas}. A fast and efficient Hankel-transform based Fresnel-type propagator is used for the propagation in radial coordinates. Furthermore, we exploited the fact that the stoichiometry of water in the cuvette is constant, albeit at different density, i.e. our sample consists of a single material with non constant complex-valued index of refraction $n(R) = 1 - \delta(R) - i\,\beta(R)$, but with constant ratio β/δ. Details on the propagator, the optimizer, and the calculation of the center coordinates of the cavitation bubble are given in the Methods section. For comparison, Fig. 3.2d shows the two-dimensional projected phase, retrieved by the iterative Alternating Projections (AP) scheme [HTS18]. The polar angle average of the AP reconstruction is compared to the RFP reconstruction in Fig. 3.2e.

The phase retrieval gives access to the projected phase $\bar{\phi}$. However, to obtain information on the 3d-density distribution of the cavitation bubble, a projection inversion is needed. Assuming sphericity of the bubble, the projection inversion is given by the inverse Abel transformation. We use a regularized version of the inverse Abel transform, which stabilizes the inner voxels with low volumetric weight against noise (see Methods), to obtain the 3d phase shift $\phi(R)$ of the cavitation bubbles (Fig. 3.2f). The measured phase describes the difference of the sample to the surrounding medium, which is in this case water at equilibrium. Thus, a positive/negative phase shift corresponds to an electron density lower/higher than uncompressed water, respectively.

Fig. 3.2 ***(next page)*****: Holographic phase retrieval and cavitation bubble density.** **a**, X-ray hologram (normalized intensity I/I_0) of a cavitation bubble at $\Delta t = 10\,\mathrm{ns}$, exhibiting strong contrast at the inner interface (gas/shockwave) and outer interface (shockwave/equilibrium water). For phase retrieval, the hologram is averaged along the polar angle to obtain the radial intensity distribution. **b**, Radial intensity distribution of (a) and intensity obtained from numerical propagation of the RFP retrieved phase (see (c)). **c**, In a forward model approach the projected phase $\bar{\phi}$ of the bubble is retrieved by minimizing the difference to the radial intensity distribution (Radially Fitted Phase, RFP). **d**, Retrieved phase of (a) using the AP algorithm, for comparison. The phase distribution reflects the deficit density in the core and excess density in the shockwave. **e**, The average along the polar angle of the AP reconstruction is compared to the result obtained from RFP (c). **f**, radial three dimensional phase ϕ reconstructed from the RFP projected phase (c). The right ordinate shows the calculated density distribution of the cavitation bubble for an ellipticity factor $\epsilon \approx 0.8$. Scale bars: 10 µm (a, d).

$\phi(R)$ describes the phase shift induced per voxel as a function of distance R to the center of the bubble and is proportional to the mass density $\rho(R)$ at a given distance R as $\rho(R) = \rho_0(1 - \epsilon\,\phi(R)/(k\,\delta))$, with k being the wavenumber of the X-rays and $\rho_0 \simeq 1\,\mathrm{g\,cm^{-3}}$ the equilibrium density of water. We determine the radius of the bubble boundary R_B and shock front R_SW at the FWHM of the respective slope of the density profile. These key values are indicated by the vertical dotted lines in Fig. 3.2f. To compensate for an initial ellipticity of the cavitation bubble, originating from a plasma elongation in the direction of the laser during dielectric breakdown, we introduce an ellipticity factor ϵ to relax the constraint on sphericity to axisymmetric ellipsoidal bubbles. We define the ellipticity factor to be the ratio of the two principal axes of the ellipsoid $\epsilon = a_\perp/a_z$, where a_z is the principal axis along the direction of the X-ray beam and $a_\perp$ the principial axis perpendicular to the beam. ϵ is chosen such that the density of the vapor inside the bubble cavity corresponds to the density of water vapor $\rho \approx 0$. Fig. 3.2f shows the phase profile (left axis) and density profile (right axis) of an exemplary cavitation bubble, consisting of gas phase core (phase maximum/density minimum) and shockwave shell (phase minimum/density maximum). For this bubble, the ellipticity factor evaluates to $\epsilon \approx 0.8$. The shockwave exhibits a density excess of $\sim 0.3\,\mathrm{g/cm^3}$. The ellipticity of the bubble changes quickly with the time delay Δt (cf. Fig. 3.6c). The median of the ellipticity decreases to the minimum value of $\epsilon \approx 0.7$ within the first ~6 ns and relaxes to 0.9–1 at ~18 ns.

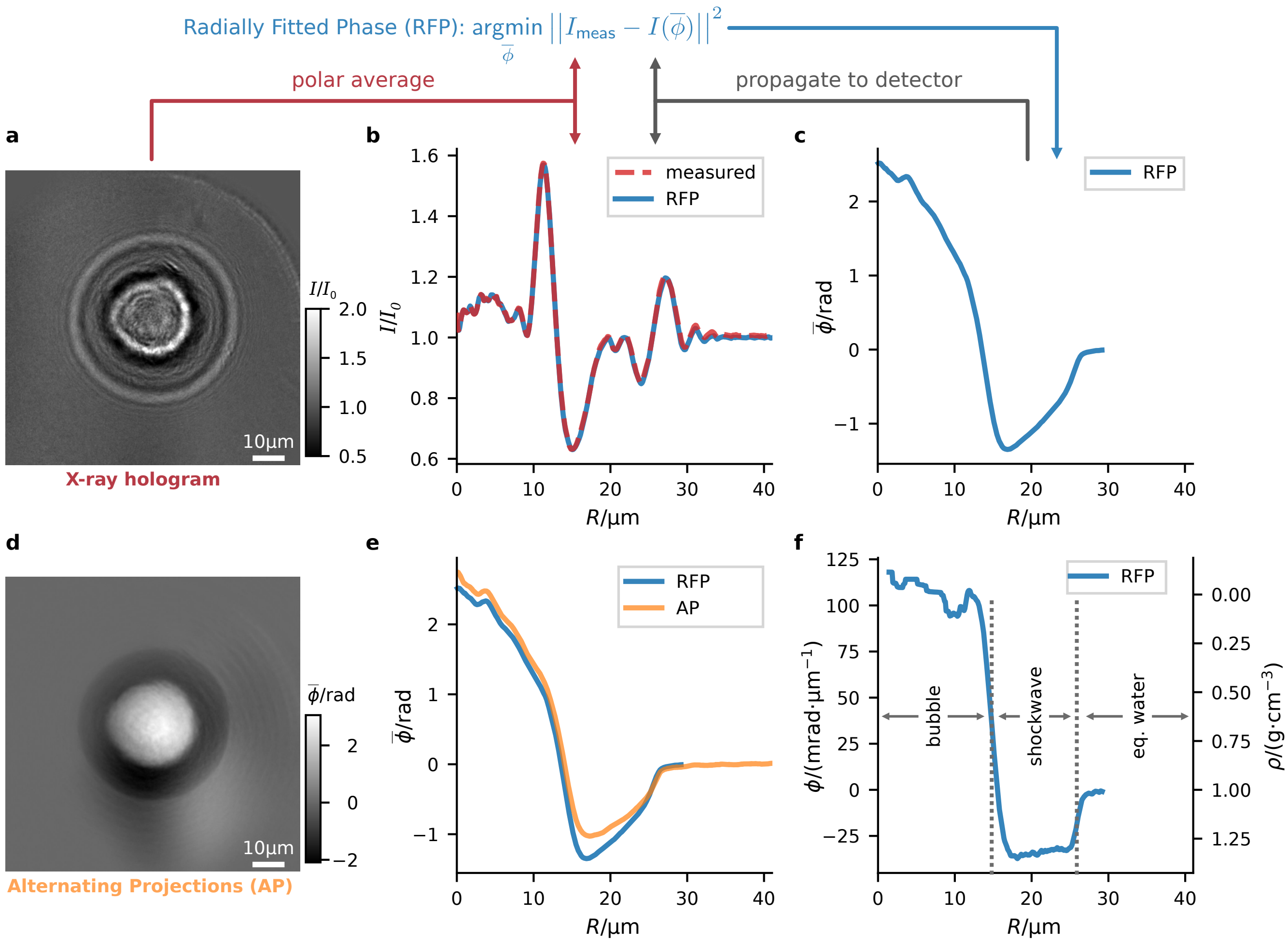

Fig. 3.2: *(caption previous page)*

3.2.3 Pressure distribution

Based on the mass density $\rho(R)$ we calculate the spatial pressure distribution $p(R)$ of the shockwave using the empirical Tait equation of state [Hay67]

$$\frac{p(R)+B}{p_0+B}=\left(\frac{\rho(R)}{\rho_0}\right)^n,$$

with the hydrostatic pressure $p_0 = 0.1\,\text{MPa}$ and the constants $B = 314\,\text{MPa}$ and $n = 7$ for water [Rid88]. Fig. 3.3 shows the 3d radial phase distribution $\phi(R)$ and the pressure distribution of the shockwave $p(R)$ for three different time delays, without ellipticity correction. For each Δt two different bubble energies E_B are shown. The energy of the cavitation event was estimated from the bubble lifetime τ, i.e. the time between dielectric breakdown and collapse, measured by the signal of the microphone at the cuvette's wall. The energy driving the bubble E_B scales approximately linearly with the third power of the lifetime τ [Lor17] (see Methods for details). Fig. 3.3 demonstrates that with X-ray holography the pressure distribution of the shockwave $p(R)$ can be obtained in close proximity to the center of the cavitation event. The cavitation events with high bubble energy E_B show an initial peak pressure of more than 20 GPa, the low energy events have peak pressures $\sim$10-times lower. Note that we have some uncertainty in the pressures due to the exact shape of the bubble along the projection direction (X-ray beam axis). It is certainly reasonable to assume axial symmetry, and we can also correct for an ellipsoidal shape, as discussed above. However, higher order contributions (in particular cone- or pear-like distortions) may also be present. This would, however, not affect the overall features of the extracted distribution such as the sign of the pressure slope or the width of the pressure distribution. Before we compare the obtained pressure distribution with simulated data, we will have a closer look at the dynamics of cavitation bubbles and the shockwave pressure in the next part.

3.2.4 Density and pressure dynamics

Out of 20000 holograms of individual cavitation events, we processed an automatically selected subset of over 3000 events. For each event the 3d-spatial phase distribution was retrieved. A summary of the results is shown in Fig. 3.4. The evolution of the bubble boundary radius R_B (radius of the interface bubble to shockwave) and the shockwave radius R_SW (outer boundary of shockwave to equilibrium water) shows a faster decrease of bubble wall velocity for lower energetic cavitation events (Fig. 3.4a).

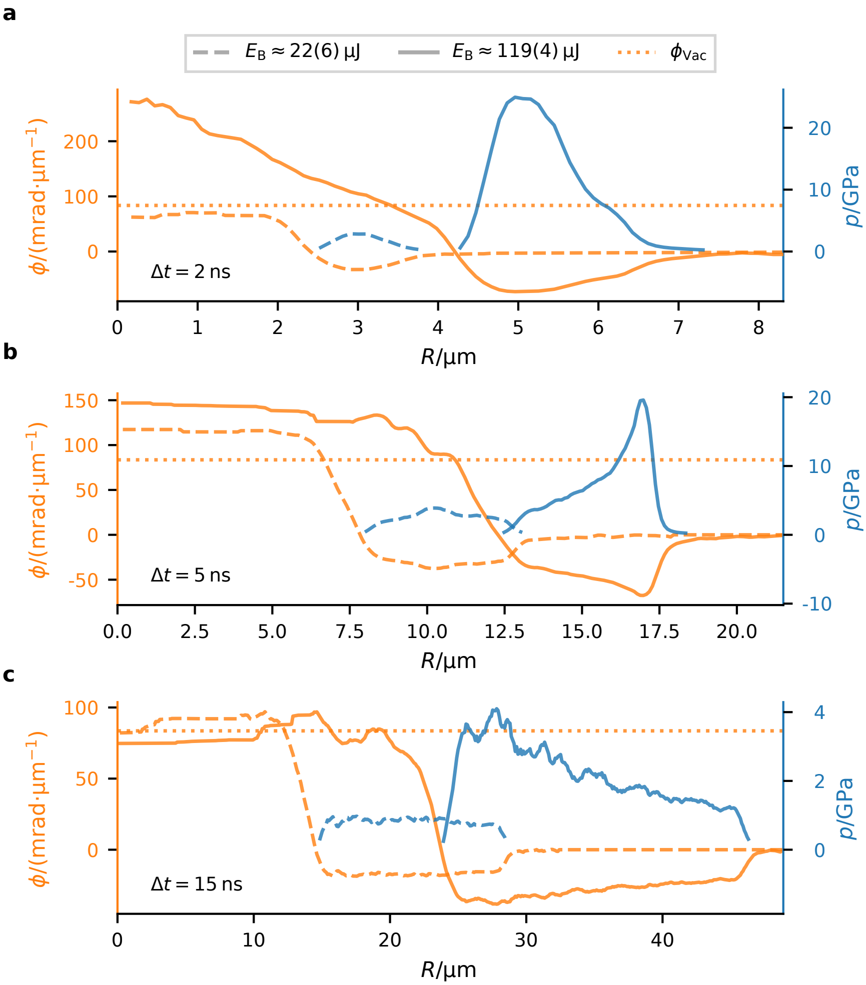

Fig. 3.3: Phase and pressure distributions of individual bubbles. a–c, Radial phase $\phi(R)$ and spatial shockwave pressure $p(R)$ for $\Delta t = 2$ ns, 5 ns and 15 ns, respectively. For each delay two exemplary cavitation events with energy of $E_\mathrm{B} \approx 22(6)$ µJ (dashed) and 119(4) µJ (solid) are compared. The 3d-phase distribution $\phi(R)$ is shown on the left ordinate (orange), the pressure distribution of the shockwave $p(R)$ on the right ordinate (blue). The phase shift of vacuum to water ϕ_vac (dotted) is shown for comparison. A phase profile exceeding this line (as is typically the case for small $\Delta\tau$ and high E_B) indicates a non-spherical bubble, and hence the necessity to introduce the ellipticity factor ϵ (see text). The pressure distribution of the shockwave was calculated using the Tait equation.

Fig. 3.4 ***(next page)*****: Cavitation dynamics.** **a**, Radius of bubble and shockwave boundary R_B and R_SW. Each scatter dot represents one processed cavitation event. The color scales with the bubble's energy (shared colorbar with (b), logarithmic scale). **b**, Radial 3d phase profiles $\phi(R)$ of cavitation events with 2–3 µm bubble boundary radius (dashed box in (a)). The radial phase was reconstructed from the RFP phases $\bar{\phi}$. The color represents E_B. The median of all phase distributions is shown in black. The phase shift of vacuum to water ϕ_vac is shown for comparison **c**, Median of phase profiles for different ranges of R_B, showing how the median phase evolves with time. Here, only cavitation events with E_B between 66–130 µJ were used. The color represents the median of the time delay Δt. The (smoothed) envelope of the shockwave's phase shift (black) is used to calculate the shockwave's peak pressure p_peak as a function of the distance to the bubble center R. **d**, $p_\mathrm{peak}(R)$ obtained from the envelope of the shockwave's phase shift for energy ranges E_B between 7–66 µJ (low E_B), 66–130 µJ (med. E_B) and 130–250 µJ (high E_B).

Each of the scatter dots shown in Fig. 3.4a represents one cavitation event with an individually retrieved phase distribution $\phi(R)$. In the following, we narrow the data down to describe the density and pressure dynamics for different energy ranges of the ensemble. To this end, we process the median of the 3d phase shift $\phi_\mathrm{med}(R)$ of all events of the ensemble for which the bubble boundary radius R_B and the energy values E_B are within a specified range. Fig. 3.4b shows the median of the phase shifts for cavitation events with R_B between 2–3 µm. This step is repeated for different ranges of R_B (Fig. 3.4c), color-coded with the median time delay Δt. Here, only cavitation events with energy E_B between 66–130 µJ were used. From the envelope of the shockwave's phase shift (median profiles), we calculate the peak-pressure distribution of the shockwave $p_\mathrm{peak}(R)$ as a function of the distance R to the center of the cavitation event. This value describes the average peak pressure that an observer measures in a distance R when the shockwave travels by. Fig. 3.4d shows $p_\mathrm{peak}(R)$ calculated from the median 3d phase profiles for three different energy ranges. Note, that here we did not compensate for ellipticity in the pressure calculation. Fig. 3.12 shows the same data with ellipticity correction. However, in this case the evolution of the peak pressure $p_\mathrm{peak}(R)$ does not monotonically decrease after reaching its maximum. This hints at the fact that cone- or pear-like shape distortions are more important at these time scales [VBP96]. In this case, the shockwave of the bubble is better modeled by a sphere than an ellipsoid, even if the cavity is not. We will see in the next section that the overall average pressure of the shockwave without ellipticity correction indeed fits reasonably well with the simulations.

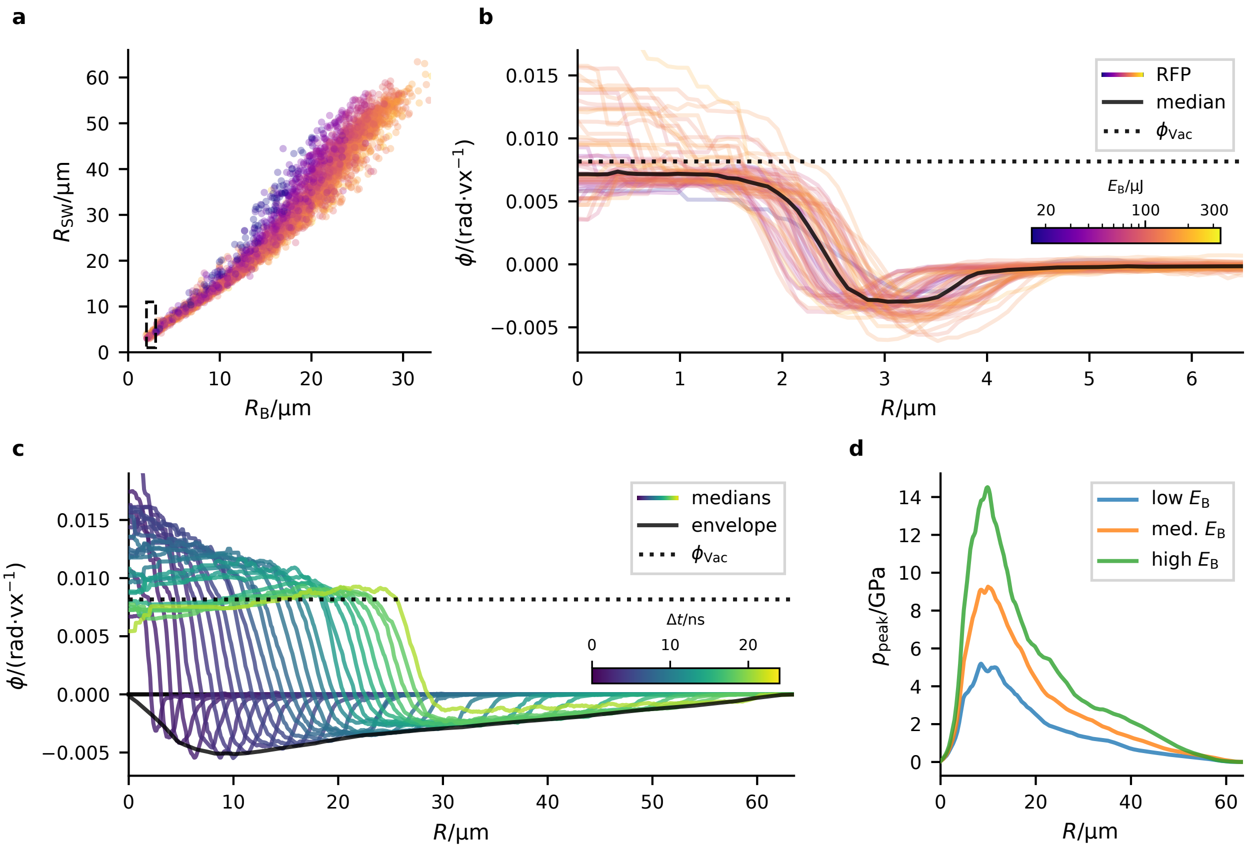

Fig. 3.4: *(caption previous page)*

3.2.5 Comparison to numerical simulations

We will now compare our data to results obtained from numerical simulations using the Gilmore-Akulichev model [Gil52] (in the following referred to as Gilmore model). The Gilmore model describes the dynamics of the bubble wall accounting for compressibility of the liquid and sound radiation. It allows the calculation of the shockwave, that is emitted during the rapid bubble expansion, via the Kirkwood-Bethe hypothesis [KB42]. Both steps use the modified Tait equation of state (3.2.3) for water (see Methods for further details).

For two exemplary energy ranges of the bubble energy E_B, we optimized the starting conditions of the simulations (similar as in [VBP96]) to fit the trajectory of the bubble wall radius $R_\mathrm{B}(\Delta t)$. The low E_B simulation was optimized for data in the energy range E_B between 20–33 µJ and the high E_B simulation for 111–130 µJ. Fig. 3.5a shows the trajectories $R_\mathrm{B}(\Delta t)$ and $R_\mathrm{SW}(\Delta t)$ for the high E_B simulation together with the experimental values in the corresponding energy range (cf. Fig. 3.14 for the low E_B trajectories). The Tait equation overestimates the shockwave speed for shock pressures exceeding 2.5 GPa [Vog+96]. To compensate this overestimation in our simulations, we treat the value B as an effective parameter of the Tait equation. With an adjustment (see section 3.5.4 for further details) of B to $2B_0$ ($B_0 = 314$ MPa [Rid88]) we achieve a good agreement of the shockfront trajectories $R_\mathrm{SW}(\Delta t)$ with our data (cf. Fig. 3.5a and Fig. 3.14a-c).

The numerical simulations yield spatial pressure distributions $p(R)$ which we compare to the experimentally determined profiles in Fig. 3.5b for the low E_B and in Fig. 3.5c–e for the high E_B simulations. Regarding the average pressure and not the functional form of the profile $p(R)$, we observe reasonable agreement for both energy ranges (see also $p_\text{peak}(R)$ in Fig. 3.14d), only the average pressure for late $\Delta t \approx 15$ ns and high E_B (Fig. 3.5e) lies significantly below the experimental data. The line shapes of $p(R)$ agree well only at low E_B, even though also here the experimental curves show some distinct features not found in the simulated profile. More importantly, for high E_B, pronounced deviations appear. The experimental profiles $p(R)$ are more highly peaked or exhibit a higher slope, which is at intermediate and late Δt not even correctly predicted in its sign. To show that this deviation is not a matter of our selection of events, we include a variety of different $p(R)$ distributions for individual cavitation bubbles within the corresponding energy range in Fig. 3.5c–e.

3.3 Discussion

In summary, we have demonstrated that extreme states of cavitation bubbles can be probed by holographic imaging with nano-focused femtosecond FEL pulses, at high spatial and temporal resolution. Quantitative analysis of near-field diffraction patterns in the holographic regime gives access to physical conditions within the cavitation bubble, including the transition from early plasma state to a cavitation bubble, density profile, and shockwave pressure at different time delays Δt after seeding. The technique offers the possibility of studying structural dynamics under different conditions (liquid parameters, external driving) in detail for a large ensemble of cavitation events. This makes it possible to study not only individual events, but simultaneously the entire ensemble, without uncontrolled ensemble averaging. In particular, all structural parameters can be sorted into bins of bubble radius, time after seeding, and/or bubble energy.

The shockwave shell bounded by the bubble radius R_B and the outer shockwave radius R_SW can be precisely quantified in terms of width and spatial density and pressure distribution as a function of time and bubble energy. Within this shell, the density and hence also the corresponding pressure is not constant, but exhibits a peak, which quickly builds up with Δt or correspondingly R_B, reaching a maximum p_max at around $R_\mathrm{B} \simeq 10\,\mu\mathrm{m}$, before it decays again more slowly with R_B. p_max is a function of bubble energy and can exceed 20 GPa (Fig. 3.3a, b). The pressure profile as a function of R is asymmetric, in particular for large R_B, where the maximum is near the inner interface and the pressure then decreases almost linearly to the equilibrium value (cf. Fig. 3.3c). Contrarily, at $R_\mathrm{B} \simeq 10\,\mu\mathrm{m}$, i.e. when compression is highest in the shockwave, density and pressure accumulate at the outer interface (Fig. 3.3b). Note that the density profile extracted from the holograms is independent of assumptions regarding any equation-of-state, while the pressure profile is not. Here we have used the Tait equation as the simplest empirical model, but the density profile can of course also be analyzed with respect to different equations of state. The widths of both interfaces (gas-shockwave and shockwave-liquid) are also of interest. The profiles exhibit a smooth transition from compressed vapour to liquid with no sharp phase boundary, in contrast to the interface profile of equilibrium bubbles. Of course, the apparent width could also result from effects of non-spherical bubble shape, but this can—at least to some extent—be excluded for bubbles with lower energy (blue/magenta curves in Fig. 3.4b) and higher R_B (green/yellow curves in Fig. 3.4c). Note that in these cases the phase profiles do not exceed the maximum vacuum/water phase shift (dashed lines), which is an indication

Fig. 3.5 *(next page)*: Simulations. **a**, Trajectories of the bubble wall radius R_B and the shockfront radius R_SW for the high E_B simulation for both values of B. The energy range of E_B for the experimental data shown here is between 111–130 µJ. The radius of maximal expansion of the simulations yields a bubble energy of 91 µJ. **b**, comparison of the measured shockwave's pressure profile $p(R)$ with the simulated $p(R)$ (low E_B simulation, $E_\mathrm{B} \approx$ 20–33 µJ) for three different time delays, again for both values of B. The time delay of the simulated profile was chosen such that it represents the experimental profile best. The exact time delays of the experimental data is $\Delta t = 2$ ns, 5 ns and 15 ns, and $\Delta t = 1.4$ ns, 6.5 ns and 13.3 ns for the simulations. The experimental pressure profiles are the same as in Fig. 3.3 with $E_\mathrm{B} \approx 22(6)$ µJ. **c–e**, same as b, but now for the high E_B simulation. The three different time delays Δt are indicated in the top left corner. The bold black curve shows the pressure profiles from Fig. 3.3 with $E_\mathrm{B} \approx 119(4)$ µJ. The gray curves are a selection of pressure profiles within the energy range shown in (a).

for the sphericity of the bubbles.

The spatial density or pressure distribution close to the bubble nucleus can not be measured with optical or acoustic methods. Optical measurements could only determine a single pressure value at the shockfront from shockfront velocity measurements. For this reason we find significantly higher peak pressures, even for lower bubble energies, within the shockwave shell compared to optical shockfront observations [VBP96]. Hydrophones for acoustic measurements disturb the shock evolution when placed in too close proximity to the cavitation center. Additionally, the hydrophones average over different radii, as the hydrophone dimensions are large, compared to the shockfront curvature at early times. For the first time we were able to measure the spatial shockwave pressure close to the cavitation center, and to compare it to numerical simulations. The comparison with numerical simulations showed a reasonable agreement with the overall peak pressure evolution (cf. Fig. 3.14d). However, the functional form of the pressure profiles shows a pronounced discrepancy (cf. Fig. 3.5b–e). The deviations of the high E_B simulations to the data is stronger than for the low E_B case. In order to rule out that this discrepancy is an artefact of elliptical or conical shape deformations along the beam axis, which would not be correctly accounted for in the reconstruction, we have carried out analytical and numerical simulations, see section 3.5.3 of the Supplementary information. These show that for realistic deformation amplitudes, the density profile in the shockwave, if reconstructed under false shape assumption, would only be scaled but not altered in shape. At the same time, the orthogonally positioned optical camera helped to rule out events with multiple plasma cores and correspondingly stronger deformations. At the same time, we cannot

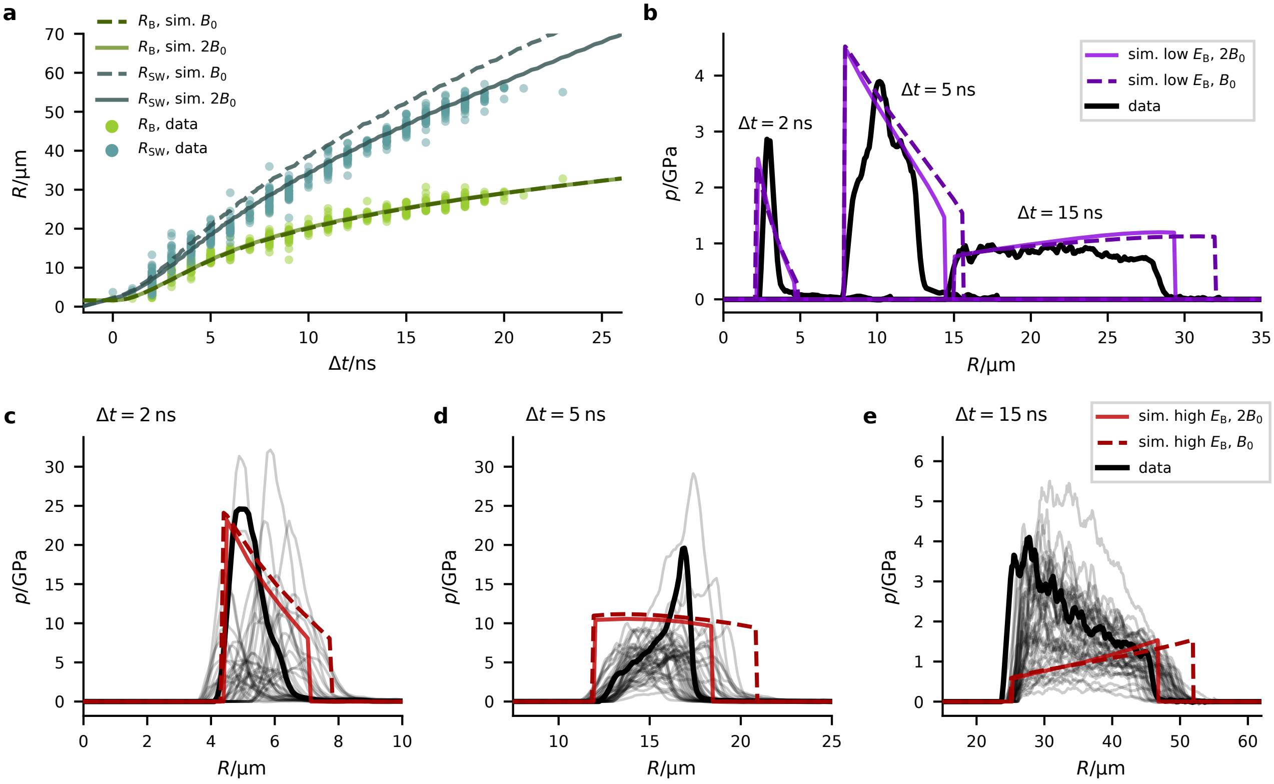

Fig. 3.5: *(caption previous page)*

exclude that already moderate deformations could lead to variations of the shockwave along the directions parallel to the the bubble surface. Also, the optical camera cannot resolve the early stages with potentially stronger asymmetry. However, by reducing the laser power to the sub-threshold regime of bubble seeding, the probability of strongly asymmetric events was significantly reduced. It is also important to note, that the higher order modes of bubble deformations are strongly damped, see section 3.5.3 of the Supplementary information. In future, the bubble shapes could be further controlled by observing the cavitation bubbles perpendicular to the pump-laser beam axis. In such a geometry, a possible variation of the shockwave density in different directions from the bubble center could be probed, which would be an interesting effect in itself to be targeted in a follow-up experiment. In that case one would need to use a 2d-phase retrieval approach (e.g. AP, cf. Fig. 3.6d, e) and the Abel transform for cylinder symmetry. A comparison with numerical simulations carried out with full spatial dimensionality (3d) [Koc+16] could also shed light on how crucial the exact shape of the bubble influences the spatial pressure distribution of the shockwave.

Importantly, however, realistic shape distortions can not explain the inversion of the pressure slope between simulation and data. We therefore must attribute the main discrepancy to the model assumptions. Notably, the Gilmore model approximates the Mach number up to the first order. Cavitation bubbles of higher energy and velocity are therefore less accurately described by the model. With the capability to probe the density profile directly by holographic X-ray imaging, new theoretical approaches beyond the current models are now timely and promising, since the predictions could be put under direct experimental validation. Correspondingly, the pressure profiles presented here could guide novel theoretic work.

The direct accessibility of density profiles also motivates evaluation and development of more advanced models in the future. In such efforts, the equations of state of water should be put into question. Incorporation of more details of optical breakdown, plasma growth [Liu+03], phase transition and heat exchange [BK04] could be addressed as well as higher-order liquid compression terms in spherical bubble models, as well as non-spherical laser plasma shapes, which can be treated by 3d fluid dynamics simulations [CGV97; Koc+16].

The methodology presented here can also be applied to more complex environments, such as cavitation interaction with a wall or interface. More generally the method can be extended to different sample systems, from driven complex fluids, to plasmas and warm dense matter. The spatial resolution was limited to about $\lesssim 500\,\mathrm{nm}$, which can be attributed to the dispersive focusing effects of the SASE pulses by the CRL. By either increasing monochromaticity with, e.g. seeded SASE pulses or by the use of achromatic nanofocusing optics with high numerical aperture, the resolution could be scaled up by more than an order of magnitude, see section 3.5.2 of the Supplementary information for a detailed discussion of resolution and scalability. While we have focused here on the bubble trajectory after seeding in a regime where a nanosecond-pump laser was sufficient, picosecond or femtosecond pump pulses would allow to investigate the ultra-fast time scales of optical breakdown in water, plasma generation and the nascent state of bubble generation.

With a future extension of the presented method, vital questions on the bubble collapse, associated with single-bubble sonoluminescence, could be answered. To this end, the collapse of the bubbles needs to be predictable with nanosecond accuracy. This could be achieved by trapping the cavitation bubbles in a stationary ultrasonic field [LK10; BHL02], synchronizing the bubble trajectory to the ultrasound (see section 3.5.5 for more details). The exact radii of collapsing bubbles are not known experimentally, but are smaller than 1 μm in diameter and can therefore not be resolved with visible light. Numerical models [MCY97; WR93; Sch+12; VSY99] predict an inhomogeneous, fast evolving distribution of pressure, density and temperature for the bubble collapse, with converging compression or shockwaves, demixing, chemical reactions and the formation of a nanoscopic thin-plasma core [CM17; MCY97; LL03] which is supposed to be the source of cavitation luminescence. With the presented methodology, direct experimental validation of this scenario is now within reach.

Acknowledgements: We thank Peter Luley and Jan Goemann for technical help. The authors thank the European XFEL in Schenefeld, Germany for granting beam time for this project. The engineering team and technicians at the MID instrument are gratefully acknowledged for help in setting up the experiment. This research was supported in part through the Maxwell computational resources operated by DESY.

Funding: M.V. and T.S. are members of the Max Planck School of Photonics supported by BMBF, Max Planck Society, and Fraunhofer Society, which has also funded consumables and instrumentation for the cavitation and optical setup. J.Hagemann and C.G.S. have been funded by the Helmholtz Imaging Platform (HIP), a platform of the Helmholtz Incubator on Information and Data Science. We acknowledge funding of the nanofocusing setup at MID by BMBF project 05K13OD2 *Erzeugung und Charakterisierung von nanofokussierten XFEL-Pulsen zur Abbildung ultraschneller*

Prozesse in Materie and for the IR-laser by BMBF project 05K16RF2 *Mikroskopische Flüssigkeitsstrahlen zur Untersuchung der Dynamik und Kinetik struktureller Nichtgleichgewichtsphasenübergänge am Europäischen Freie-Elektronen-Laser*. Open Access funding enabled and organized by Projekt DEAL.

Data availability: The data that support the findings of this study are available from the corresponding author upon reasonable request and after 2022-06-10 through European XFEL services under [HS19].

Code availability: The algorithms used to reproduce the findings of this study are described in detail within the manuscript and the Methods. The code is available from the corresponding author upon reasonable request.

Author contributions: T.S., J.Hagemann authored the proposal of the XFEL experiment, with help from M.O., T.K. and R.M.. M.V., H.P.H., J.Hagemann, J.M.R., and M.O. prepared the experiment from the user side, with support/advice from T.S., R.M. and T.K.. M.S., J.M., J.Hallmann, U.B., C.K., A.Z., W.L., R.Shayduk, R.Schaffer, led by A.M. prepared and contributed instrumentation and experimental technology of the beamline, complemented by synchronisation and integration work by M.O., M.V., and H.P.H.. F.S., A.S. and C.G.S provided the nano-focus optic. M.V., H.P.H., J.Hagemann, J.M.R., M.O., A.S. and T.S. performed the XFEL experiment with M.S., J.M., J.Hallmann, U.B., C.K., A.Z., W.L., R.Shayduk, R.Schaffer, and A.M.. M.V., H.P.H., M.O. and J.Hagemann analyzed data with input from T.S. and R.M.. The manuscript was mainly written by M.V. and T.S. with substantial input from co-authors. All authors read and approved the manuscript.

Competing interests: The authors declare no competing interests.

3.4 Methods

3.4.1 Experimental design

X-ray optics

The experiment was performed at the MID (Materials Imaging and Dynamics) instrument [Mad+21; Tsc+17] at the European X-ray Free-Electron Laser [Alt+06] in

Schenefeld, Germany. The FEL was operated at 14 GeV electron energy and an undulator line delivered ultra-fast (100 fs or less) X-ray pulses with 14 keV photon energy, 10 Hz repetition rate in single-bunch mode and 600(300) µJ average pulse energy or about $3(2) \times 10^{11}$ photons per pulse. The X-rays were focused by a stack of 50 nano-CRLs, aberration corrected by a custom-made phase plate [Sei+17b], with a focal length of 298 mm and a numerical aperture of 4.3×10^{-4}. Prior to the nano-CRLs, the *CRL-1* system of the MID instrument [Mad+21] was used to prefocus the X-rays. The prefocus was chosen such that the beam size at the nano-CRLs overilluminated the nano-CRLs' aperture. The X-ray focus to sample distance was $z_{01} = 144$ mm and focus to detector distance $z_{02} = 9578$ mm. The X-ray detector was a five mega pixel sCMOS camera (Andor Zyla 5.5, Oxford Instruments, Abingdon, United Kingdom) with a fiber-coupled scintillator (LuAg:Ce, thickness 20 µm) converting X-rays to optical photons with a pixel size of 6.5 µm. The cone-beam geometry led to 66.5 × magnification and 98 nm effective pixel size in the sample plane. The Fresnel number, describing the wave-optical properties of the imaging system, was $F = 7.6 \times 10^{-4}$. In the sample cuvette, the X-rays passed two quartz-glass windows with 150 µm thickness and about 5 mm of water.

Laser optics

We used a Litron Lasers Nano L 200-10 (Litron Lasers, Rugby, United Kingdom) laser system with 1064 nm wavelength, 6 ns pulse duration and 200 mJ maximum pulse energy, which was reduced to 24 mJ by an internal attenuator. The beam was expanded to increase the numerical aperture to 0.2 , with a focal length of 50 mm. A flat mirror with a through-hole allowed co-linear alignment of the laser and X-ray beam. The focal spot size is expected to exceed the diffraction limited FWHM of 1.7 µm, since in addition to spherical abberations of the lens, the through-hole on the last mirror introduced aberrations to the wavefront and a fine adjustment of the laser focus position was used to match the laser and X-ray focus after focal alignment of the laser. The seeding rate of the cavitation events was about 23 % with a Root-Mean-Square variation of 3 %. Multi-bubble events have been observed for about 30 % of the cavitation events. The radius of maximum expansion of the cavitation bubbles was typically in the range of 500–700 µm, with lifetimes of 100–150 µs. A detailed analysis of these properties is published separately in [Ost+21].

Optical high-speed measurements

Observation of the individual cavitation events with the optical high-speed camera (Photron Fastcam SA5, Photron, Tokyo, Japan) allows to capture the full bubble dynamics, including plasma breakdown, expansion, first collapse and bubble rebound from the side. Images where recorded with background illumination with a continuous halogen light source (LS-M352, Sumita, Japan) using a long-distance microscope (K2 Distamax, Infinity, USA). Incoming light is refracted by the cavitation bubble, creating a shadow in the bright-field image. From the optical imaging we deduce the number and shape of plasma luminescence spots and follow the full bubble motion, including the measurement of its maximum expansion radius R_{max}. Due to limitations in the data download speed from the optical camera's internal memory, optical measurements are conducted for approximately half of all runs. Additional information and exemplary high-speed recordings can be found in Fig. 3.6.

Timing equipment

In order to process each cavitation event individually, precise timing, as well as the ability to relate each data source to one unique cavitation bubble is necessary. The FEL provided a unique train ID for each X-ray pulse, which was stored along with the signals acquired by the MID instrument. However, custom equipment, not fully integrated to the FEL's data acquisition system (DAQ), was necessary for this experiment. To this end, an AND gate was used to synchronize data sources not integrated in the FEL's DAQ with the FEL's unique train IDs. The AND gate provided a centralised first pulse, so that pump laser, high-speed camera, and the data recording of the microphone started simultaneously. The output of the AND gate was fed to the FEL's DAQ, so that this first pulse could be attributed to the unique train ID of one X-ray pulse.

For the precise timing, we used a pair of low jitter delay generators (DG535, Stanford Research Systems) controlling the delays of the lasers flash lamp, Pockels cells, and the high-speed optical camera to the FEL's master trigger. The delay between the flash lamp and Pockels cells was kept constant at 160 µs for maximal laser output. The signals of the microphone, the FEL's master trigger, the output of the laser Pockels cells and the shutter output of the high-speed optical camera were digitised by an USB oscilloscope (PicoScope 6402C, Pico Technology, St Neots, United Kingdom). Further details on the timing setup, including cabling schemes and all electronic components are published in [Ost+21].

3.4.2 Data analysis

Phase retrieval: Radially Fitted Phase

Propagation of radially symmetric wavefields: The two dimensional (2d) Fourier transform $\mathcal{F}$ of a 2d signal $f(x, y)$ with radial symmetry $f(x, y) = f(r\ \cos\theta, r\ \sin\theta)$ is related to the zeroth-order Hankel transform $\mathcal{H}_0$ as [Bad09]

$$\mathcal{H}_0\left[g\right](\nu) = \frac{1}{2\pi}\mathcal{F}[f](\nu\cos\theta, \nu\sin\theta). \tag{3.1}$$

As the zeroth-order Hankel transform is self-inverse, the 2d Fourier transform of a radially symmetric signal is (up to prefactors) self-inverse as well. The 2d Fresnel propagator is written as [Pag06]

$$\begin{aligned}\psi(x, y, z = \Delta) \approx \exp(ik\Delta) \cdot \\ \mathcal{F}^{-1}\left[\exp\left(\frac{-i\Delta(\nu_x^2 + \nu_y^2)}{2k}\right)\mathcal{F}[\psi(x, y, z = 0)]\right],\end{aligned}$$

with $\psi(x, y, z)$ the wavefield at position (x, y, z), where z is the direction of propagation and Δ the propagation distance. $\mathcal{F}$ is the 2d Fourier transform in a plane perpendicular to the propagation distance and (ν_x, ν_y) the Fourier coordinates. $\mathcal{F}^{-1}$ is the inverse Fourier transform, respectively. Note that the Fresnel kernel is radially symmetric, as it only depends on $\nu_x^2 + \nu_y^2 =: \nu_\perp^2$. This implies that the propagated wavefield $\psi(x, y, z = \Delta)$ of a radially symmetric wavefield $\psi(x, y, z = 0) = \psi(r_\perp, z = 0)$ at $z = 0$ has radial symmetry as well and thus only depends on $(r_\perp, z)$. Using eq. (3.1) we can write the propagated wavefield as

$$\begin{aligned}\psi(x, y, z = \Delta) = \psi(r_\perp, z = \Delta) = \exp(ik\Delta) \cdot \\ \mathcal{H}_0\left[\exp\left(\frac{-i\Delta\nu_\perp^2}{2k}\right)\mathcal{H}_0[\psi(r_\perp, z = 0)]\right].\end{aligned} \tag{3.2}$$

The discrete Hankel transform can be written as a matrix multiplication of an $N \times N$ matrix H_0 with an $N \times 1$ vector representing a discretization of a function f [BC15]. With a discrete kernel of the Fresnel propagation D_Δ, this gives a fast and efficient Fresnel-type propagator in radial symmetric coordinates

$$\psi(r_i, z = \Delta) = \exp(ik\Delta)H_0 D_\Delta H_0 \psi(r_i, z = 0).$$

The propagation matrix $P_\triangle = H_0 D_\triangle H_0$ has to be calculated only once and can be used for propagation of different wavefields ψ, so that the Fresnel propagation reduces to the matrix multiplication of $P_\triangle$ with a wavefield ψ.

Radially Fitted Phase: The phase retrieval approach Radially Fitted Phase makes use of the radial symmetry of the cavitation bubbles and is formulated as an optimization problem, searching for the object's phase $\bar{\phi}(R)$ minimizing the ℓ^2-distance of the calculated radial intensity $I(\bar{\phi}(R))$, when propagating $\bar{\phi}$ numerically to the detector, to the measured radial intensity I_{meas}, i.e. $||I_{\text{meas}}(R) - I(\bar{\phi}(R))||^2$. For the calculation of $I(\bar{\phi})$, the object's exit field is calculated in a first step, using a constant β/δ-ratio κ. The assumption of constant κ is perfectly satisfied for the cavitation bubbles containing water and water vapour at different pressures only. In a second step, the object's exit wavefield $\psi_{\text{obj}}(R) = \exp\left[(i+\kappa)\bar{\phi}(R)\right]$ is propagated to the detector, using the matrix approach from eq. (3.2). The minimization of the ℓ^2-norm is done by the BFGS algorithm [NW06], a quasi-Newton method by Broyden, Fletcher, Goldfarb, and Shanno implemented in the *minimize* function of *SciPy*'s *optimization* submodule (version 1.4.1) [Vir+20]. The method can be easily extended to be regularized by further penalty terms, such as total variation (TV) norm or Tikhonov regularization. For the data shown in this work the algorithm was stable without further regularization.

Regularized inverse Abel transform: The phase retrieval gives access to the projected phase of the cavitation bubbles, but to access physical quantities, the 3d phase of the cavitation bubble is indispensable. The inverse Abel transform [BB00] gives a fast and efficient way to calculate the 3d phase from its projection as a linear map, with the assumption of spherical symmetry. However, the reconstruction of the central voxels of the 3d-phase distribution is strongly affected by noise, as the number of voxels per shell with radius R decreases quadratically. To stabilize the inverse Abel transform against noise, we regularized the inner voxels with an ℓ^1-norm total variation penalty term up to a radius R_{TV} which is 60 % of the radius R_{B} where the bubble transitions into the shockwave. This regularizes about 36 % of all voxels of the gaseous bubble and even less of the whole volume, including the shockwave. The optimization uses *SciPy*'s *minimize* function as described in the paragraph above.

Acoustic signal

The acoustic signal is detected by a piezoelectric microphone, glued to the outside of one of the cuvette walls. The acoustic waves emitted by the optical breakdown and the collapse are recorded by the USB oscilloscope (PicoScope 6402C, Pico Technology, St Neots, United Kingdom), with a sampling rate of 38.4 ns. At the position of the microphone, in a distance of ∼15 mm from the breakdown position, the shock and sound waves are dispersed. Noise originating from reflections from the cuvette walls, and further scattering from impurities and satellite bubbles are present. The lifetime τ is obtained as the time interval between the first two strongest peaks of the convolved microphone intensity (rectangular kernel with a width of 38.4 µs). For random samples, we verified that these two peaks correspond to the breakdown and first collapse of the cavitation events.

Classification of cavitation events

Individual cavitation events are classified in terms of the mechanical bubble energy E_B that is deposited by the IR laser pulse. This value can be accessed from the maximum expansion radius of the cavitation bubble R_max, related by [Lor17; PP77]

$$E_\mathrm{B} = \frac{4}{3}\pi(p_0 - p_v)R_\mathrm{max}^3.$$

Here $p_0 = 100\,\mathrm{kPa}$ is the ambient hydrostatic pressure and $p_v = 2.34\,\mathrm{kPa}$ the vapour pressure at ambient temperature of $T_0 = 20^\circ\mathrm{C}$ [Lid+95]. Since direct measurement of R_max by the high-speed optical camera is available only for about half of all events, we extrapolated the relation between the lifetime τ, which is obtained from the acoustic signal, and R_max. For a spherical collapse this relation is given by [Lor17; KDH71]

$$\tau = 2 \cdot 0.915\, R_\mathrm{max}\sqrt{\frac{\rho_0}{p_0 - p_v}},$$

with $\rho_0 \simeq 1\,\mathrm{g\,cm^{-3}}$ the equilibrium water density. Note that the lifetime τ is assumed to be twice the collapse time. We observe a linear relation of $R_\mathrm{max} = m \cdot \tau + b$ with $m = 4.45(3)\,\mathrm{m\,s^{-1}}$ and $b = 84(3)\,\mu\mathrm{m}$. Hence the measured collapse time is prolongated by a factor of 1.22 with respect to the spherical case, given by the Rayleigh-Plesset model. In part, this is expected to be induced by boundary interaction of the cavitation bubble with the entrance window. The offset b can not fully be attributed to the initial size of the breakdown plasma. Further details are published in [Ost+21].

3.4.3 Numerical modeling of cavitation and shockwave dynamics

Bubble dynamics

The dynamics of the early bubble growth was simulated with a Gilmore-Akulichev model [Gil52] in combination with shockwave propagation based on the Kirkwood-Bethe hypothesis [KB42]. This model is usually used for simulations including acoustic radiation as it incorporates both liquid compressibility as well as a pressure-dependent sound velocity [LV13]. We implemented a time-dependent absorption of the laser pulse energy into the Gilmore model as was previously used in [VBP96].

The calculation is based on two steps — the first step is the simulation of the bubble boundary motion via the solution of the following system of differential equations for the position R and velocity U of the bubble wall:

$$\begin{aligned}
\dot{R} &= U \\
\dot{U} &= \left[-\frac{3}{2}\left(1-\frac{U}{3C}\right)U^2 + \left(1+\frac{U}{C}\right)H + \frac{U}{C}\left(1-\frac{U}{C}\right)R\frac{dH}{dR}\right] \\
&\quad \cdot \left[R\left(1-\frac{U}{C}\right)\right]^{-1},
\end{aligned}$$

with the pressure dependent sound velocity C, the enthalpy H and pressure P at the bubble wall, given by

$$\begin{aligned}
C &= c_0\left(\frac{P+B}{p_0+B}\right)^{\frac{n-1}{2n}}, \\
H &= \frac{n(p_0+B)}{\rho_0(n-1)}\left[\left(\frac{P+B}{p_0+B}\right)^{\frac{n-1}{n}} - 1\right], \\
P &= \left(p_0 + \frac{2\sigma}{R_n}\right)\left(\frac{R_n}{R}\right)^{3\kappa} - \frac{2\sigma}{R} - \frac{4\eta U}{R}.
\end{aligned}$$

Here, $c_0 = 1483\,\mathrm{m\,s^{-1}}$ is the sound velocity in water at normal pressure $p_0 = 100\,\mathrm{kPa}$ [Lid+95], $n = 7$ and $B = 314\,\mathrm{MPa}$ are empirical parameters of the Tait equation of state [Rid88], $\rho_0 = 998\,\mathrm{kg\,m^{-3}}$ is the density of water, $\sigma = 72.538\,\mathrm{mN\,m^{-1}}$ the surface tension at the water-vapour interface, $\kappa = 4/3$ the polytropic exponent and $\eta = 1.046\,\mathrm{mPa\,s}$ the dynamic viscosity of water at room temperature [VBP96]. The bubble interior is modeled as an ideal gas. The laser pulse is assumed to be Gaussian-shaped, and incorporated by the time-dependent rest radius

$$R_n(t) = R_{nb}\left[0.5\left(1+\text{erf}\left(\frac{t-t_a}{\sigma_l\sqrt{2}}\right)\right)\right]^{\frac{1}{3}}.$$

The increase of vapour volume of a sphere with radius $R_n(t)$ is proportional to the deposited laser energy. In this way, R_n expands during the presence of the laser pulse and is constant afterwards, driving the rapid expansion of the cavitation bubble. We used the error function erf(t) with the width σ_l to compute the energy deposition of the Gaussian shaped pulse with a FWHM width of $\tau_l = 2\sigma_l\sqrt{2\ln(2)}$. The effective initial bubble radius $R_{na} = R_n(t=0)$ is varied via t_a. We typically choose $R_{na} \approx 1\,\mu\text{m}$, being significantly smaller than the radius of the initial plasma spark observed by the optical camera.

Shockwave propagation

The second step of the simulation is the calculation of the pressure profile for radii r beyond the bubble wall radius R ($r > R$), via shockwave propagation. To this end, we compute the trajectories of the characteristics using each state of the bubble wall trajectory as initial conditions for the propagation of the invariant quantity $G = r(h + u^2/2) = R(H + U^2/2)$ by solving the following system of differential equations [KB42; KDH71; Hol10]:

$$\begin{aligned}
\dot{r} &= u + c \\
\dot{u} &= \frac{1}{c-u}\left((u+c)\frac{G}{r^2} - \frac{2c^2u}{r}\right) \\
\dot{p} &= \frac{\rho_0}{r(c-u)}\left(\frac{p+B}{p_0+B}\right)^{\frac{1}{n}}\left(2c^2u^2 - \frac{c^2+uc}{r}G\right)
\end{aligned}$$

Here, r is the position, u the velocity and p the pressure of the characteristic. Further parameters, such as the pressure-dependent sound velocity c, are given in the previous paragraph.

Pressure profiles are found as plane-intersections of constant $t = \Delta t$ in the $p(r,t)$-space spanned by all characteristics. At the shock front, a discontinuity is present, indicated by ambiguous distributions $u(r)$ and $p(r)$. As prescribed by the conservation laws of mass-, momentum- and energy-flux through the discontinuity, the position of the shock front r_s is determined to be at the position, where the area below and above the ambiguous part of the respective $u(r)$ curves are equal [LL91; VBP96]. For Δt where a shock has not yet formed, the front of the pressure profile was determined as the width where the pressure surrounding the bubble drops to $1/e^2$ of its peak pressure. The model assumes a constant gas pressure $p(r < R) = P$ inside the cavity, and equilibrium pressure $p(r > r_s) = p_0$ beyond the shock front.

We optimize the parameters R_{na}, R_{nb}, τ_l, and t_0, so that the simulated trajectories of the bubble wall $R_\mathrm{B}(\Delta t)$ and shock front position $R_\mathrm{SW}(\Delta t)$ fit with the experimentally determined values from X-ray imaging, as well as with the optical and acoustic measurements. The time shift t_0 is used to determine the arrival of the seeding laser with respect to the FEL pulse.

Alternatively, we are able to compare directly the simulated pressure profiles $p(r > R)$ to the data obtained by X-ray holography.

3.5 Supplementary Materials

3.5.1 High-speed optical imaging and plasma shape

Here, we show additional images of the optical high-speed camera, including images of the breakdown plasma luminescence. The optical camera observes the cavitation events from the side, perpendicular to the X-ray beam. An exemplary bubble cycle is depicted in Supplementary Fig. 3.6a. Note that this is the same cavitation event as shown in Fig. 3.2 of the main manuscript. As described in detail in the Methods section of the main manuscript, the maximum radius of expansion R_max of the cavitation bubble in combination with the lifetime τ measured with the microphone signal is used to determine the deposited bubble energy E_B. Furthermore, we can analyse the shape of the initial breakdown plasma, which is usually visible in the first frame of the high-speed video. We determine the number of plasma cores, each of them leading to the generation of a cavitation bubble and shockwave. Additionally, we can estimate an ellipticity factor $\epsilon_\mathrm{opt} = h/b$ of the breakdown plasma with the height h and width b of the plasma luminescence spot. Note that the image containing the plasma spark was exposed for the shutter opening time of 1.01 µs, during which the plasma already expanded to its maximum extent. The change of the plasma luminescence shape becomes obvious as ϵ_opt varies significantly already upon a shift of the optical camera trigger delay of multiples of 10 ns. In Supplementary Fig. 3.6b the first frame of a high-speed video is shown as a close-up, with two illustrated ellipses representing

ϵ of the X-ray measurements and ϵ_{opt} of the optical camera for comparison. We observe different sizes and ellipticities in both measurements. Note that the X-ray hologram was taken with an ultra-fast flash at $\Delta t = 10$ ns whereas the optical image was taken with a shutter time of 1.01 µs. The ellipticity ϵ extracted from the X-ray data decreases with Δt. In the early expansion phase, the cavitation bubble is more elliptical (Supplementary Fig. 3.6c). However, we did not find a substantial correlation between ϵ_{opt} of the optical camera and the ellipticity ϵ of the X-ray data. This is not surprising not only in view of the different integration times, i.e. single pulse X-ray exposure versus >1 µs long exposure time of optical camera, but also the different contrast mechanisms. In the X-ray data, we probe the density profile of bubble and shockwave, whereas we primarily probe the plasma luminosity in the optical data.

As we induce cavitation in a sub-threshold regime of the seeding laser's irradiance, we mostly observe almost point-like or elliptical plasma cores which fluctuate in their position along the IR laser axis. In Supplementary Fig. 3.7a some examples of individual cavitation events are depicted. Supplementary Figures 3.7b and c show enlarged images of two cavitation events. The latter is a rather rare event (in the sub-threshold regime) with multiple elliptical plasma cores and is not further processed in the X-ray analysis workflow (vetoed out). Note that in this run, the timing of the 1.01 µs optical shutter was chosen such that the camera is illuminated until 260(25) ns after optical breakdown. The outer limit of the bubble thus corresponds to its maximum expanse at a time of about 260 ns.

In Supplementary Fig. 3.6d–f we show a cavitation event with two breakdown plasma cores. The double event is visible in both measurements, in the side view of the optical camera and in the 2d phase reconstructed hologram (Alternating Projections [AP] phase retrieval [HTS18]). Such events, including even more chaotic scenarios as shown in Supplementary Fig. 3.16, are not suited to compute $\phi(R)$ with the radial symmetric phase retrieval approach RFP, however can be reconstructed with the 2d approach. For instance, in Supplementary Fig. 3.6f one clearly recognizes the two compression waves emanating from the plasma cores. Events like this could be further analyzed in terms of bubble and shock densities of nascent or even crossing shock waves from different breakdown positions. However in the presented work, such events have been excluded from the analysis.

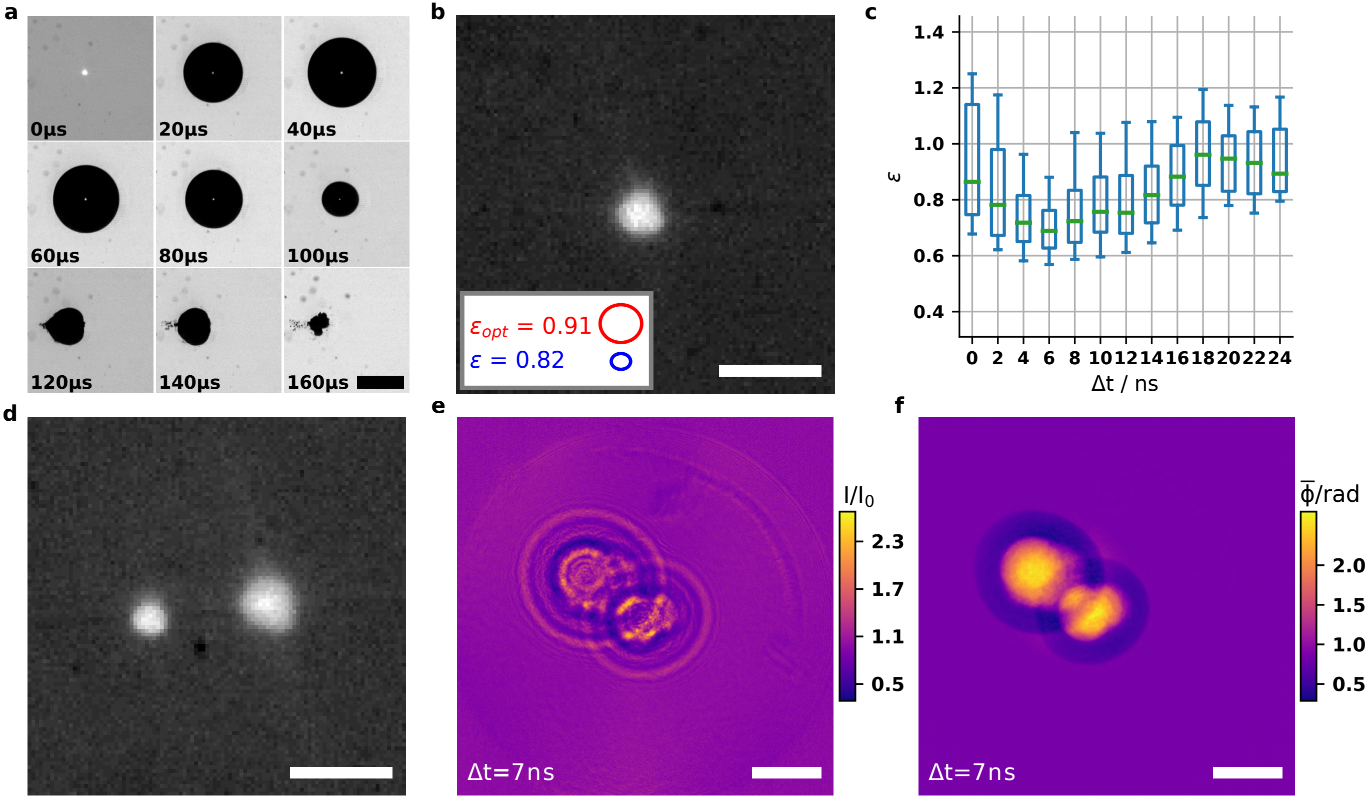

Fig. 3.6: *(caption next page)*

Fig. 3.6 *(previous page)*: Observations of the plasma shape. **a**, Optical high-speed measurements of a full bubble cycle. The first frame is synchronized to the X-ray pulse with a time delay of $\Delta t = 7$ ns after the IR-pump pulse. **b**, Enlarged view of the plasma luminescence, with indicated ellipticity and scale of the optical (red) and X-ray (blue) measurements. The two ellipses are drawn to scale. The same cavitation event is shown as in Fig. 3.2. **c**, Box-whisker plot of the ellipticity ϵ from the X-ray measurements, with respect to 2 ns bins of Δt (green line, median; the box contains 50 % of the data; whiskers show the 10th and 90th percentile). **d**, single frame of optical high-speed measurement featuring a double-breakdown event. **e**, Normalized intensity I/I_0 of the X-ray hologram of the event in (d). Note, that the observation direction of the optical and X-ray imaging are perpendicular. **f**, AP phase reconstruction of the event in (d). Scale bars: 750 µm (a), 200 µm (b, d), 25 µm (e, f).

3.5.2 Spatial resolution and scalability

We briefly discuss the spatial resolution and its scalability for the method of single pulse holography using cone-beam geometry. Importantly, X-ray holography is not subject to the resolution restrictions known for optical imaging of cavitation bubbles. In fact, as stable seeding of cavitation bubbles requires substantial distances from the cuvette wall optical imaging with high numerical aperture objectives is impeded, and resolutions in the range 2–10 µm are already quite exceptional. This is not the case for X-ray imaging in cone-beam geometry, which in principle can achieve the resolution given by the focal spot size. The present experiment was designed for sub-100 nm spot size (CRL focus), and a well matched geometrical magnification of 66, resulting in an effective pixel size of 98 nm. However, different resolution deteriorating factors have to be taken into account, including possible aberrations of the incoming beam, bandwidth of the XFEL radiation, detector PSF, etc.

To obtain an estimation on the resolution of the presented method, we analyze the interface profile of a stably floating bubble. This seems a better choice than a cavitation bubble, since the out-of-equilibrium nature of a cavitation bubble could result in a broadened interface between the gas and aqueous phase. Supplementary Fig. 3.8a, b show the X-ray hologram of a floating bubble and the angularly averaged intensity, respectively. The highest spatial frequency encoded in the hologram can be estimated by the maximum scattering angle of the interface, or more precisely the angular range of fringe visibility. Supplementary Fig. 3.8b shows fringes extending over an angular range of 0.14 mrad, corresponding to a half-width-at-half-maximum (HWHM) resolution of 3.8 px, or 370 nm. Note that the possible resolution given by the entire illuminated detector area and the numerical aperture of the CRLs with a theoretical

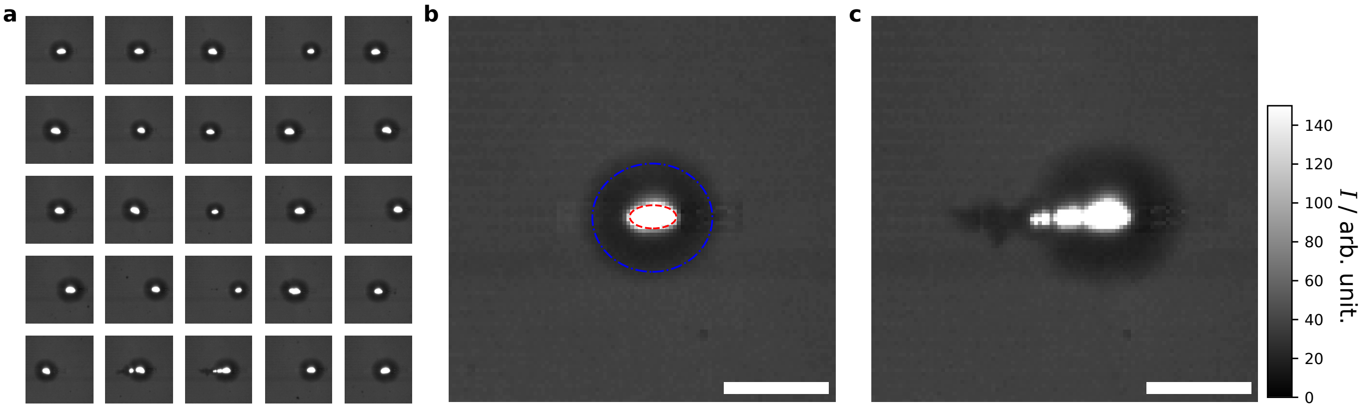

Fig. 3.7: Optical observations of the plasma and cavitation bubble. **a**, Exemplary overview of individual cavitation events. The position of the plasma core fluctuates along the laser beam axis. **b**, Enlarged view of a cavitation event with an ellipsoidal plasma core. The early state of the expanding bubble is visible as the dark region surrounding the plasma spark. The bubble-water interface is blurred due to its motion. We extract semi-major and -minor axes of $a_p = 44\,\mu\text{m}$ and $b_p = 22\,\mu\text{m}$ for the plasma core (red) and $a_b = 114\,\mu\text{m}$ and $b_b = 103\,\mu\text{m}$ for the expanding bubble (blue). **c**, Cavitation event with multiple plasma cores. Such events can be identified by the optical measurements and are vetoed out in the X-ray analysis workflow. In this measurement, the timing of the optical shutter was chosen such that the camera illuminates until 260(25) ns after optical breakdown. Scale bars: 200 µm.

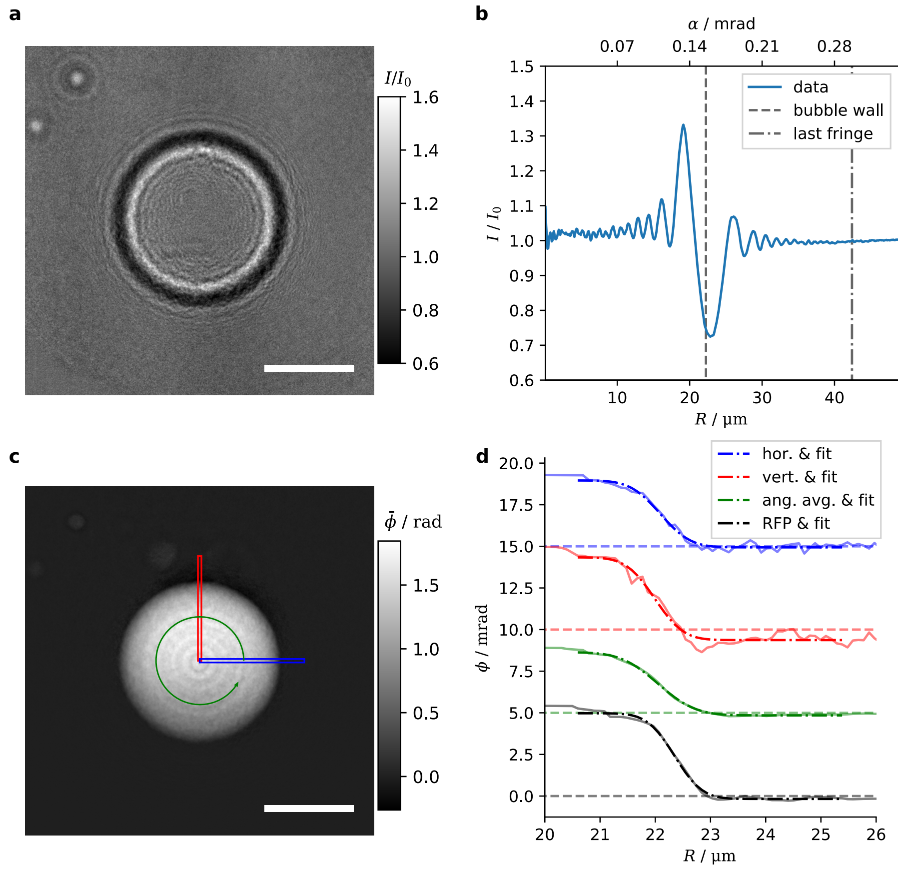

Fig. 3.8: Resolution estimation: **a**, Normalized intensity I/I_0 of the X-ray hologram of a freely floating bubble, i.e. no cavitation bubble. **b**, Angular average of the intensity of the X-ray hologram (a). The upper abscissa shows the diffraction angle α on the detector. The angle of maximum Fresnel diffraction (fringe visibility), i.e. the range spanned between the bubble wall and the outermost fringe is given by $\alpha_{\max} \approx 0.14$ mrad, corresponding to a resolution of about 370 nm (HWHM). **c**, AP reconstruction of the projected phase $\bar{\phi}$ of the floating bubble (a). In the marked regions line profiles have been extracted for further analysis of the resolution. **d**, Reconstructed radial (3d) phase profiles $\phi(r)$ as a function of the radius R. The HWHM resolution is determined from an error function fitted to the data. The blue, red and green curves show the radial 3d phase $\phi(r)$ of the line profiles from the AP reconstruction in (c). For better visibility, the curves are offset by 5 mrad. The dashed lines indicate zero phase shift for each color. The obtained HWHM resolution is 500(40) nm (horizontal, blue), 480(60) nm (vertical, red), and 620(20) nm (angular average, green). The black curve is obtained from the phase retrieved by the RFP algorithm. The HWHM resolution of the RFP phase is 460(20) nm. Scale bars: 25 µm corresponding to a detection angle of 0.18 mrad in (a); 25 µm in (c).

focal spot size of 78 nm (FWHM) is in principle much higher.

To quantify the influence of the phase retrieval on the resolution, we analyze line profiles of the reconstructed phase. Supplementary Fig. 3.8c shows the reconstructed phase (2d projected phase) of the equilibrium bubble, as reconstructed by the AP algorithm. Profiles along the horizontal and vertical direction as well as radially averaged profiles are then used for a regularized inverse Abel transform to obtain the reconstructed phase $\phi(r)$ (3d phase), which is proportional to the electron density. A modified error function with width σ is fitted to the curve to obtain the interfacial width. We find 500(40) nm for the horizontal profile, 480(60) nm for the vertical profile and 620(20) nm for the radial average. Furthermore, we calculate the edge steepness from the density profile, obtained by the RFP reconstruction algorithm. Here, the interfacial profile $\phi(r)$, fitted to an error function, results in a HWHM of 460(20) nm. Note that all given values represent the HWHM of the edge, given by HWHM $= 1.17\sigma$, with σ the RMS-width of the error function. Importantly, the achieved resolution is sufficient to probe the interface profiles of the cavitation bubbles. The cavitation event shown in Fig. 3.2 of the main manuscript, for example, exhibits an edge width of 1270(10) nm for the bubble boundary and 690(20) nm (HWHM from RFP) for the shock front, well in excess of the resolution limit. We can take this as an indication that the interfacial width of cavitation bubbles is intrinsically broader than the equilibrium gas-water interface.

Nevertheless, the theoretically achievable resolution of sub-100-nm is not reached. We have identified the spectral bandwidth of the SASE radiation of the XFEL with approximately 60 eV (FWHM) to be a major cause for a focus broadening and thus a degradation of the resolution. CRLs are chromatic optics, i.e. different photon energies are focused with a different focal length. The focal length f is proportional to the inverse of the decrement δ of the refractive index $f \propto \delta^{-1}$ [Sch+01] and the decrement scales with $\delta \propto E^{-2}$. Hence, for small variations ΔE in the photon energy we get a deviation Δf of the focal length of approximately $\Delta f/f \approx 2\Delta E/E$. If we approximate the spectral bandwidth of the XFEL pulses to be on the order of $\Delta E/E \approx 4 \times 10^{-3}$ (FWHM), we get for $f = 298$ mm a deviation in the focal length of $\Delta f \approx 2.4$ mm (FWHM). This value is almost 15-times the Rayleigh length of 160 µm. The beam diameter at $\Delta f/2 \approx 1.2$ mm defocus is already larger than $\gtrsim$ 600 nm (FWHM). The superposition of the different longitudinal modes of the XFEL radiation thus results in a substantial broadening of the X-ray focus and consequently to a degradation of the holographic resolution. The approximated focal width of $\gtrsim$ 600 nm (FWHM) is in good agreement with the resolution obtained from the maximum scattering angle of the holograms of 370 nm (HWHM).

Next, we briefly comment on scalability. Cone-beam X-ray holographic imaging has been demonstrated at resolutions down to 25 nm [Bar+15b], based on waveguide-filtered synchrotron radiation. For the present single pulse holographic imaging experiment, scaling up the resolution would require higher longitudinal coherence or an achromatic optic, to achieve a truely diffraction-limited spot size in the sub-100 nm range. To this end, either the longitudinal coherence of the beamline needs to be improved by e.g. seeded SASE radiation or achromatic optics like X-ray waveguides, with even higher numerical apertures, could be exploited.

Last, we briefly compare the present spatial resolution to optical imaging of cavitation bubbles. As cavitation is usually investigated in bulk water, i.e. a cuvette with significant extent, long-distance objectives are used for imaging. As a benchmark example we can refer to [VBP96], where the detailed shape of a large plasma cone of laser seeded cavitation bubble is resolved at a working distance of 35 mm, and with a resolution stated as 4 μm. Stan et. al [Sta+16] imaged XFEL-induced explosions of a water jet with optical imaging. In this special case of an experiment without the need for a water-filled cuvette, they obtained a resolution of 780 nm (half cycle) for a test pattern and $\sim$1 μm for the water jet. To our knowledge, however, such resolution values were not yet achieved in imaging for cavitation in bulk water. Furthermore, in contrast to the present approach, it is impossible for optical cavitation imaging to scale the resolution up. More importantly, optical contrast does not allow for a direct measurement of the shockwave density close to a cavitation nucleus, let alone a quantitative pressure profile.

For visual appreciation of the high spatial sampling in the present x-ray imaging approach, we include Supplementary Fig. 3.9, showing two enlarged images of early states of laser-induced cavitation events. Both the flat-field corrected X-ray hologram as well as the AP reconstructed phase shift $\bar{\phi}$ is shown in each image. Sub-micrometer scale density fluctuations are visible both in the X-ray hologram as well in the reconstructed phase. These can be attributed to fluctuations in the initial breakdown plasma which still persist after plasma growth.

3.5.3 Influence of ellipticity

In the present experimental setting, no lateral X-ray view of the cavitation bubble was recorded. While the high-speed optical camera can help to control ellipticity ϵ and to veto out strongly asymmetric cavitation events, e.g. due to formation of multiple

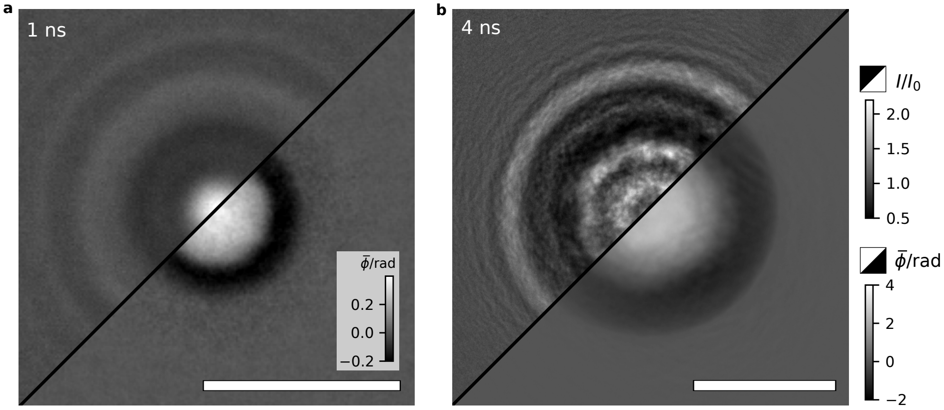

Fig. 3.9: X-ray holograms and retrieved phase image. Cavitation events probed at **a**, $\Delta t = 1\,\mathrm{ns}$ and **b**, $\Delta t = 4\,\mathrm{ns}$ respectively, during optical breakdown and plasma expansion. The upper left part of the images shows the normalized intensity I/I_0 of the X-ray hologram. The bottom right part shows the X-ray phase shift $\bar{\phi}$ in the sample plane, obtained by AP phase reconstruction. Scale bars: $10\,\mu\mathrm{m}$.

plasmas (see Supplementary Fig. 3.6), the illumination times of the optical camera are too long to match the X-ray acquisitions. They hence can only inform on bubble shapes at later times, or more precisely, show shapes which must be regarded as a time integral. For this reason, the assumption of a spherical or elliptical shape when reconstructing a radial profile of the cavitation bubble, has to be critically questioned. Non-spherical shapes of cavitation bubbles have been investigated by methods of linear stability analysis, showing that the growth process is stable [PS78], with perturbations subject to either damped or over-damped relaxation. For viscous fluids the latter is true and the perturbation amplitude tends to zero as the bubble grows [PS78]. At the same time, the initial conditions for laser seeded bubbles result in axial-symmetric but not spherical-symmetric initial conditions. We therefore must expect elliptical or even pear-formed bubble deformations at the early times, see Supplementary Fig. 3.6, and the discussion in the main manuscript regarding the constraint of positive electron density in the bubble center. Hence, while one observes a spherical shape with bubble radius R_0 from the projection image (or equivalently the hologram), the actual radius of curvature may be higher $R \geq R_0$. In the simplest case we would expect an elliptical half axis along the optical axis z with $R_z = R_0/\epsilon$, but in the beginning, pear-like shapes are also likely. Importantly, both elliptical and non-elliptical (but differentiable) shape deformations can be treated in the same manner in form of a Taylor expansion around the spherical (or even the elliptical) case. Since, however, the projection of an ellipsoid is again an ellipse, an ellipsoidal deformation results in a projection profile $P(x)$ which is scaled by a prefactor, but preserves its functional form, see the schematics in Supplementary Fig. 3.10. In the same manner, a spherically bulged slab of radius R and thickness d with, for example, a flat radial profile (hat profile), projects to a profile

$$P(x) = \begin{cases} 2\left(\sqrt{(R+d)^2 - x^2} - \sqrt{R^2 - x^2}\right) & , x \leq R \\ 2\sqrt{(R+d)^2 - x^2} & , R < x \leq R + d \\ 0 & , x > R + d\,. \end{cases}$$

Written in unitless coordinates $x' = (x - R)/d$ and $R' = R/d$, and expanding for $R' \ll 1$, the projected profile becomes [Bee+09; Mel09]

$$P(x') \simeq \begin{cases} 2\left(\sqrt{1 - x'} - \sqrt{-x'}\right) & , -R' \leq x' \leq 0 \\ 2\sqrt{1 - x'} & , 0 < x' \leq 1 \\ 0 & , x' > 1\,. \end{cases}$$

Hence an inverse Abel transform, falsely assuming radial symmetry and not accounting for $\epsilon \neq 1$ would still yield the correct flat hat profile of the slab. Since arbitrary profiles can be approximated by concentric shells (each with a hat function), the shapes of the projection profiles are preserved unless the deformations become excessively large or non-differentiable. Supplementary Fig. 3.11 presents numerical solutions to corroborate the conclusions drawn from the analytical slab model. Again, we see that the hat profile reflecting a flat density profile of compressed water in the shock wave around a distorted gas bubble projects to the same functional form $P(x)$, when restricting the range of x to the range of the projected shock wave. More relevant still, is the radial density profile $\rho(r)$ computed by the inverse Abel transform from $P(x)$, which clearly reconstructs a flat hat profile for all cases shown. Altogether, this confirms our conclusions in the main text. The deviations of the experimental shock waves from the fluid dynamical model predictions, as shown in in Fig. 3.5c–e of the main manuscript, cannot be explained by parameter choices regarding the radius of curvature, or equivalently ϵ or even more general shape deformations along the optical axis. Instead the deviations, and in particular the inversion of the pressure slope has to be attributed to shortcomings of the model, which were previously not observed, since the density and pressure profile could not be properly accessed. At the same time, we stress that in the relatively simple scenario treated here, the density of the shockwave does not vary along the directions parallel to the bubble surface,

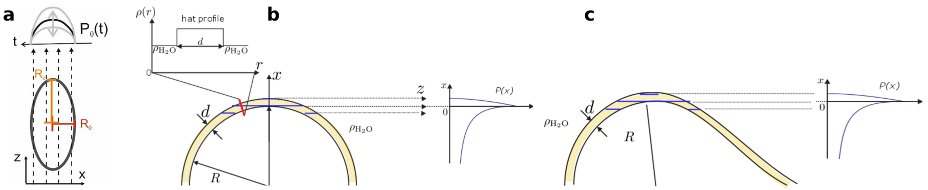

Fig. 3.10: Projection of ellipsoids and shapes with local deviation of the radius of curvature. **a**, Schematic of the projection of an elliptically deformed bubble. While one observes a spherical shape with bubble radius R_0 from the projection image (or equivalently the hologram), the actual elliptical half axis along the optical axis z is $R_z > R_0$. This results in a different prefactor of the projection profile $P(t)$. The functional form of $P(t)$ is preserved. **b, c**, Projection of a spherically bulged slab of thickness d, and radius R. Up to quadratic order in d/R, the shape of the projection profile $P(x)$ in the range $R < x < R + d$ remains constant, i.e. $P(x)$ is only scaled by a prefactor proportional to R. Hence small deviations around the assumed spherical shape would not affect the shape of the radial profile obtained from the inverse Abel transform. This can be shown analytically for a hat profile, and by linearity translates to general analytical radial profiles.

which could be expected for deformed bubbles. In the main text, we therefore suggest experimental geometries which are able to probe also such effects.

3.5.4 Modification of the Tait equation

The Tait equation fits experimental data for pressure values up to 2.5 GPa [RAH47]. For higher pressures however, the shockwave velocity u_s is overestimated [Vog+96]. This leads to an overestimation of the simulated shockwave radii $R_{\mathrm{SW}}(\Delta t)$. Supplementary Fig. 3.13 shows $u_s(p_s)$ calculated using the Tait equation for different values of B compared to the Rice-Walsh equation of state, with validity of up to ~25 GPa [RW57]. As the Rice-Walsh equation of state cannot easily be incorporated into the Gilmore model equation [VBP96], we compensate for this deviation, by treating B as an effective parameter in the Tait equation. Increasing B effectively decreases the shockwave velocity $u_s(p_s)$ for high pressures. It can be interpreted as an increase in the effective bulk modulus of water for high pressures. With an adjustment of B to $2B_0$ ($B_0 = 314$ MPa [Rid88]), we underestimate $u_s(p)$ for low values of p, but get a better agreement with the Rice-Walsh data for higher pressures. As our simulations quickly grow to high pressures, we obtain better agreement of $R_{\mathrm{SW}}(\Delta t)$ with the data for $B = 2B_0$ (cf. Fig. 3.5a and Fig. 3.5a–c). Note that the adjustment of B has strong

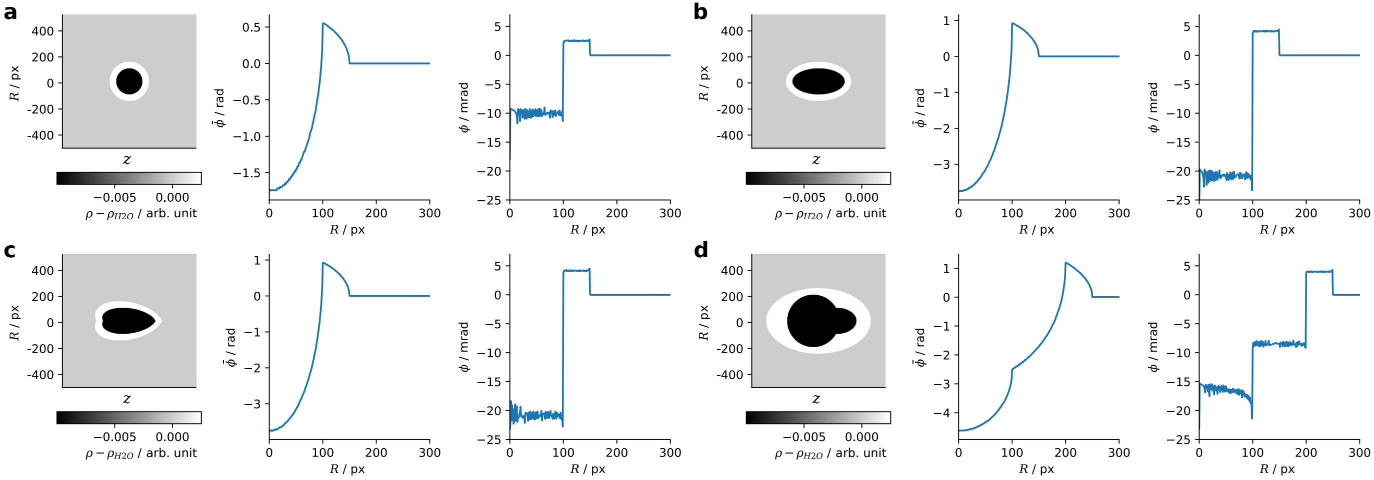

Fig. 3.11: Numerical calculation of radial profiles from bubble phantoms with shape deformations. For each case the phantom (2d) is shown on the left with X-ray optical parameters set to the experimental values, for shockwave (white), and bubble (black), immersed in bulk water (gray). z denotes the direction of propagation of the X-rays. The center shows the corresponding projected phase profile and on the right the radial profile extracted from the inverse Abel transformation is shown, i.e. falsely assuming spherical symmetry. The following cases, including unrealistically high shape distortions, all lead to the same and correct functional form for the radial density profile of the shockwave, here assumed as a flat profile: **a**, Perfect spherical symmetry for reference, **b**, elliptical distorted bubble, **c**, ’bullet’ shape, and **d**, bubble with a bud.

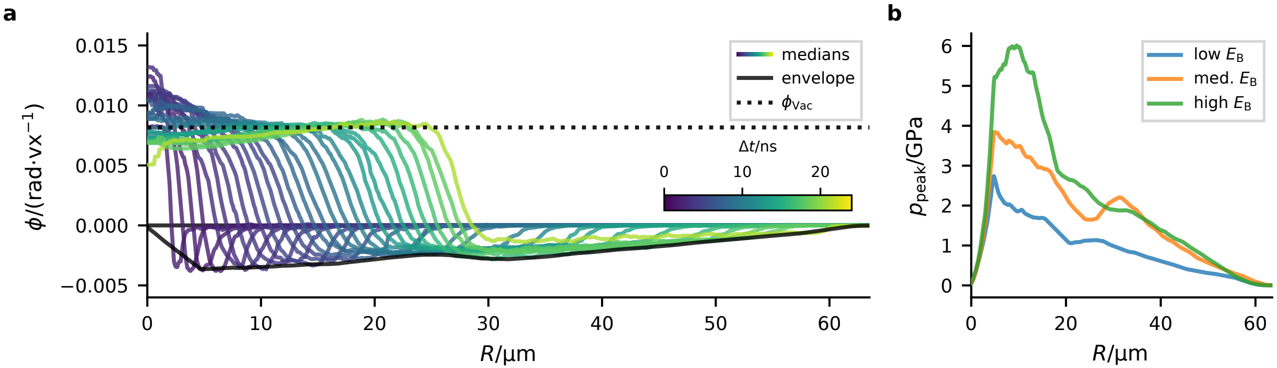

Fig. 3.12: Cavitation dynamics with ellipticity correction. a, Median of the phase profiles for different ranges of the bubble radius R_{B}, showing how the median phase evolves with time ($E_{\mathrm{B}} = 66$–$130\,\mu\mathrm{J}$). In comparison to Fig. 3.4c, the phase profiles have been corrected with the bubbles ellipticity ϵ before calculation of the median. The color represents the median of the time delay Δt. The (smoothed) envelope of the shockwave's phase shift (black) is used to calculate the shockwave's pressure as a function of the distance to the bubble center R. **b**, Peak pressure p_{peak} as a function of the distance to the bubble center R, obtained from the envelope of the ellipticity corrected shockwave's phase shift for energy ranges E_{B} between 7–66 µJ (low E_{B}), 66–130 µJ (med. E_{B}) and 130–250 µJ (high E_{B}).

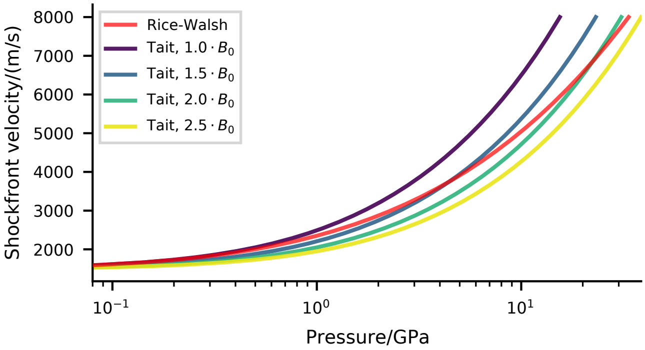

Fig. 3.13: Equations of state. Comparison of the Rice-Walsh equation of state [RW57] to the Tait equation of state with different constants B. The Tait equation of state with $B = B_0$ approximates the Rice-Walsh equation of state well for pressures below $\sim$2.5 GPa [RAH47]. Consequently, the shockfront velocity is overestimated by the Tait equation for higher pressures. We compensate this effect by adjusting the constant B of the Tait equation to $2B_0$.

impact on the trajectory $R_{\mathrm{SW}}(\Delta t)$, whereas $R_{\mathrm{B}}(\Delta t)$ is only slightly changed.

3.5.5 Imaging of the bubble collapse

So far, we have focused on imaging and analysis of the optical breakdown, shockwave emission and the early states of bubble expansion. However, the presented experimental technique is in principle also suited to image the bubble collapse. The present timing scheme does not facilitate a synchronization of the FEL pulse and the bubble collapse, hence does not allow a systematic measurement of the bubble collapse. We find a mean bubble lifetime $\tau = 120\,\mu\mathrm{s}$ with a standard deviation of $\sigma = 24\,\mu\mathrm{s}$ [Ost+21]. With the 10 Hz repetition rate of the XFEL and a 25 % seeding rate of the cavitation bubbles we might image the bubble collapse within a time window of 5 ns by chance, once in 1.5 hours.

In Supplementary Fig. 3.16a–c a cavitation event is depicted where we observed the bubble close to the collapse. Supplementary Fig. 3.16a shows the optical high-speed video, Supplementary Fig. 3.16b the near-field hologram recorded with the parallel X-ray beam (without nanofocusing CRLs) and Supplementary Fig. 3.16c the phase retrieval using the single materials approach [Pag+02]. The X-rays capture the collapsing bubble within the exposure of the fourth frame of Supplementary Fig. 3.16a, with a time delay $\Delta t = 132\,\mu\mathrm{s}$ after seeding. From the bubble lifetime and the delay

Fig. 3.14 ***(next page)*****: Simulations.** Simulated trajectories of bubble wall radius R_B **(a)** and shockwave radius R_SW **(b)**. The data is shown as scatter dots for comparison. The color scales with the bubble's energy (shared colorbar, logarithmic scale). The simulation was run with 2 different sets of parameters to fit to lower energetic cavitation events ($E_\mathrm{B} \approx$ 20–33 µJ) and to fit higher energetic cavitation events ($E_\mathrm{B} \approx$ 111–130 µJ), as well as with two different values for the constant B (see main text). Whereas the bubble wall trajectories fit the data well for both values of B, the shockwave trajectory overestimates R_SW of the data for $B = B_0$. The radius of maximal expansion of the simulations yields a bubble energy of 22 µJ for the low E_B and 91 µJ for the high E_B simulation. **c**, Trajectory of R_B and R_SW for the low E_B simulation. Here, only experimental data in the energy range of $E_\mathrm{B} \approx$ 20–33 µJ is shown. **d**, peak shockwave pressure p_peak in a distance R to the bubble center for three energy ranges of the experimental data (cf. Fig. 3.4d) and the simulations. The pressure profiles of the simulations have been convolved with a Gaussian function (500 nm FWHM) before calculation of the peak pressure p_peak.

between seeding laser and FEL pulse, we estimate that the bubble was probed ~300 ns before the collapse. The parallel beam geometry was chosen in this run to illuminate a larger field of view, so that also large bubbles at such high time delays and collapse rebounds fit into the field of view. Supplementary Fig. 3.16d–f shows a high-energy cavitation event with a high elongation and jetting during the collapse, due to multiple plasma sparks [LK10]. The video of the HS camera is shown in Supplementary Fig. 3.16d with the X-ray flash during the 8th frame at 204 µs after seeding. Supplementary Fig. 3.16e depicts the X-ray hologram and Supplementary Fig. 3.16f the phase retrieval using [Pag+02]. The hologram was recorded after the second collapse during the second rebound. Supplementary Fig. 3.16f clearly shows the torus-like bubble shape with the liquid region in the center, originating from the jet. Furthermore, a liquid bridge can be recognized traversing the torus sideways. This demonstrates that such recordings can image details of non-spherical bubble collapses that are otherwise obscured to optical imaging. The parallel beam geometry comes at the cost of lower resolution and lower quality of the phase retrieval. Nevertheless, we emphasize the versatility of the method and the experimental setup, enabling also single-shot imaging of millimeter-scale involved structures.

However, high-resolution phase contrast images are necessary to image the fine details during the bubble collapse. For this reason, we plan to synchronize the bubble collapse with the FEL pulse by acoustic trapping of the laser-induced cavitation bubbles. The ultrasonic field drives the bubble periodically, with frequencies locked to the FEL's repetition rate, so that the X-ray flash comes at a fixed point of time in the life cycle

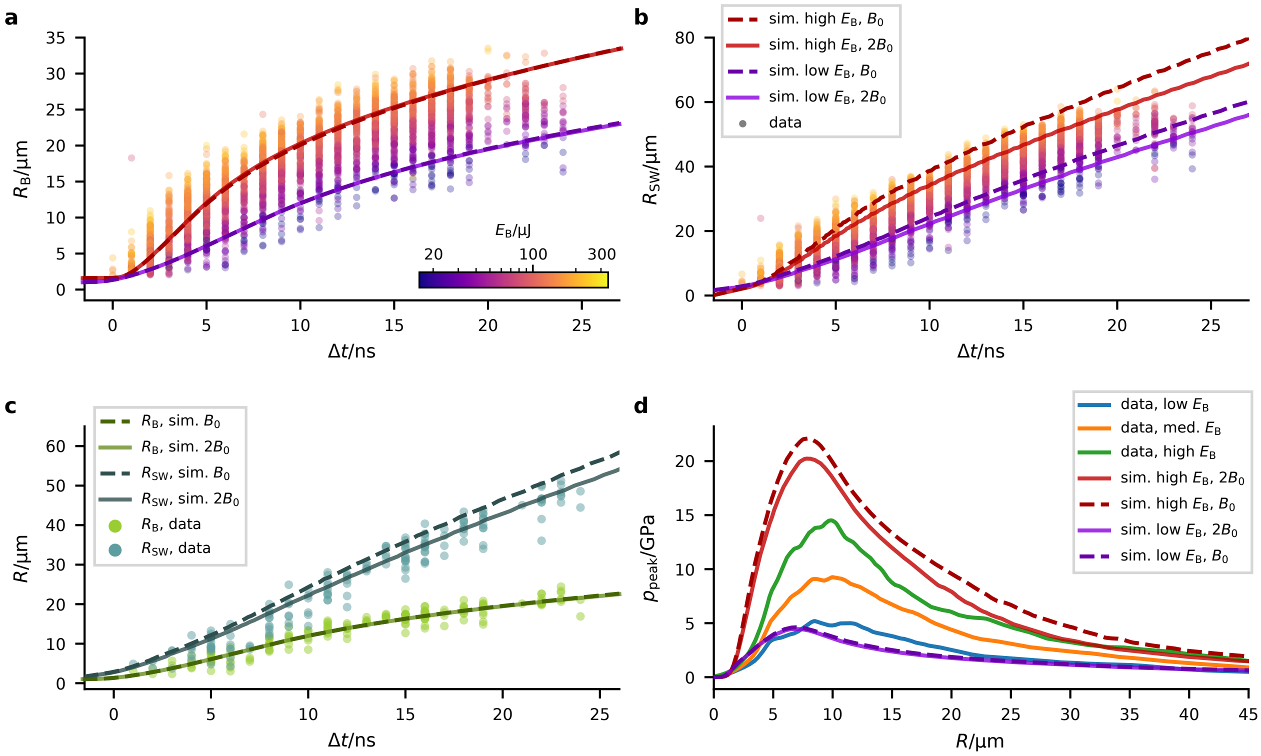

Fig. 3.14: *(caption previous page)*

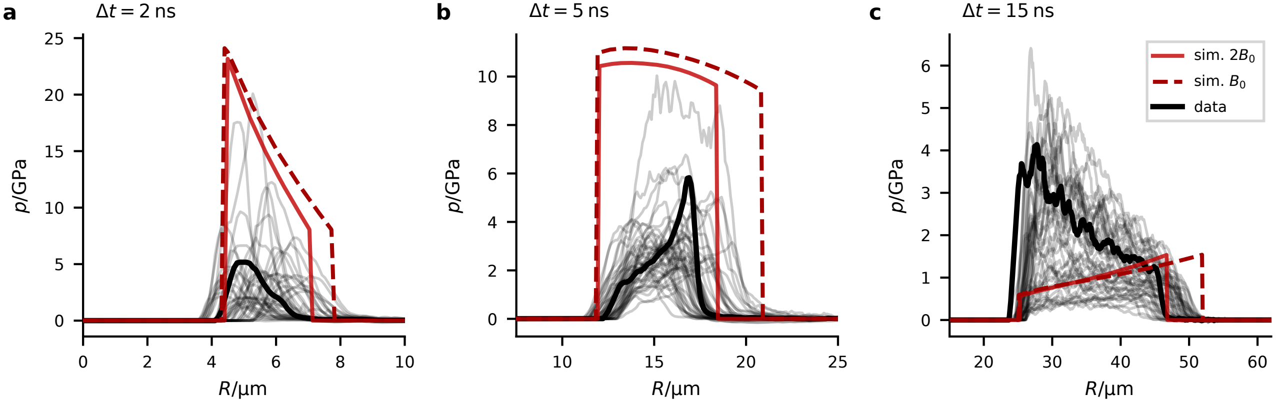

Fig. 3.15: Pressure distribution with compensated ellipticity. a–c, comparison of the measured, ellipticity corrected, shock-wave's pressure profile $p(R)$ with the simulated pressure profiles (high E_B simulation) for three different time delays Δt as indicated in the top left corner. The simulation is shown for both values of B. The bold black curve shows the pressure profiles from Fig. 3.3, the gray curves are a selection of pressure profiles within the energy range $E_\mathrm{B} \approx 111$–$130\,\mu\mathrm{J}$. All experimental pressure distributions have been corrected with the calculated ellipticity factor ϵ.

Fig. 3.16 *(next page)*: Capturing the bubble collapse. a, Optical high-speed measurement of a bubble cycle. The 5th frame was synchronized to the X-ray pulse, with a time delay of $\Delta t = 132\,\mu\mathrm{s}$ to the IR-pump pulse. **b**, Normalized intensity I/I_0 of the X-ray hologram of the collapsing bubble in parallel beam geometry. The 5th frame of the optical images is shown at the same scale for comparison in the inset. **c**, Paganin-type phase reconstruction of the projected phase $\bar{\phi}$ of the collapsing bubble. **d**, optical high-speed measurement of a bubble cycle. The 8th frame was synchronized to the X-ray pulse, with $\Delta t = 204\,\mu\mathrm{s}$. **e**, hologram of the chaotic bubble rebound after the collapse, of the event shown in (d). **f**, Paganin-type phase reconstruction of the chaotic bubble rebound. Scale bars: 750 µm (a, d), 200 µm (b, c, e, f).

of the bubble. In this case, the X-ray flash can be synchronized to the collapse of the bubble with a tunable delay, to measure the collapse dynamics with high-resolution holography setup and the presented method.

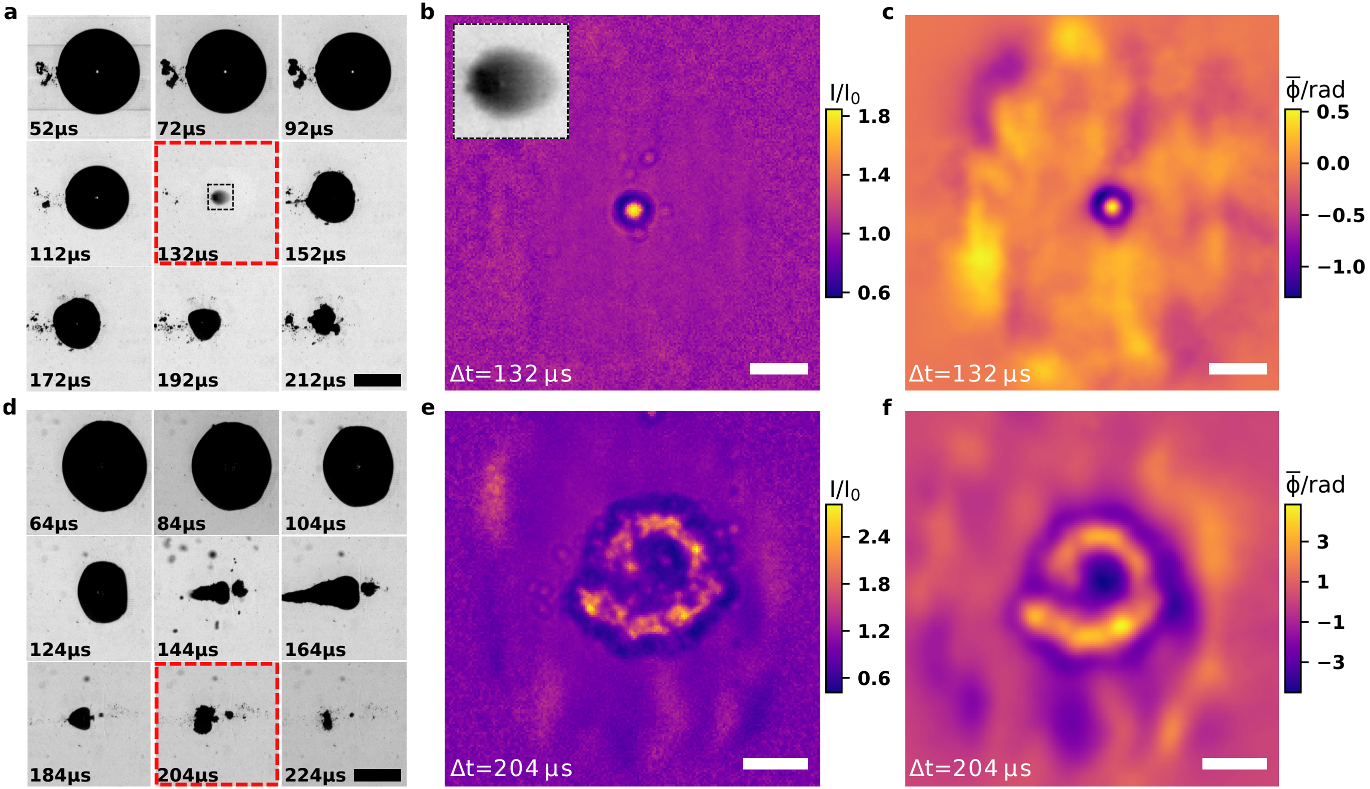

Fig. 3.16: *(caption previous page)*

Structural dynamics of water after dielectric breakdown

4

M. VASSHOLZ, H. P. HOEPPE, J. HAGEMANN, J. M. ROSSELLÓ, M. OSTERHOFF, R. METTIN, J. MÖLLER, M. SCHOLZ, U. BOESENBERG, J. HALLMANN, C. KIM, A. ZOZULYA, W. LU, R. SHAYDUK, A. MADSEN, T. SALDITT

(unpublished manuscript)

We explore the pressure evolution and the dynamics of transient phase transitions in a μ-fluidic water jet after laser-induced dielectric breakdown in a combined approach of nearfield holography with single femtosecond X-ray free-electron laser pulses and X-ray diffraction. To this end, we relate the changes in the arrangement of the water molecules to pressures and compare the non-equilibrium phase transition to results under static pressure. We observe chaotic perturbations with thin filamentation during the gas expansion after dielectric breakdown in nearfield holography and witness a transition of the molecular structure in diffraction. We show how single-pulse holography and diffraction with X-ray free-electron laser radiation complement each other to obtain quantitative information from the microscopic length scale to the molecular level.

4.1 Introduction

X-ray techniques have revealed numerous interesting and surprising insights on the molecular structure of water that help to understand its anomalous behaviour in the thermodynamical response functions. These discoveries are summarized in great detail in various review articles [NP20; NP15; MS98; Deb03]. X-ray diffraction with table-top X-ray tubes has revealed the molecular structure of ice in at least two amorphous forms with different densities, namely high-density [BOM35] and low-density amorphous ice [MCW84]. But not only ice was found to exist in two different density configurations. Neutron scattering experiments reported liquid water in two molecular configurations with different densities [SR00]. In its low-density liquid (LDL) form, water molecules tend to arrange in a tetrahedral structure, whereas for the high-density liquid (HDL) the second coordination shell of water molecules seems to collapse [Ski+14].

The development of X-ray sources with higher brilliance, such as synchrotrons and X-ray free-electron lasers (XFEL), has spurred observations on water in extreme conditions [Sel+14; Per+17; Kim+20a; Kim+20b]. As an example, the exact transition from HDL to LDL was subject to controversial discussion [NP20]. A synchrotron experiment gave strong evidence for a liquid-liquid transition (LLT) between HDL and LDL [Per+17], which has been recently directly observed in an XFEL experiment [Kim+20a]. In addition, the latter experiment gave strong implications for a liquid-liquid critical point [Kim+20a].

Apart from these extreme states in the low temperature regime, the molecular structure of water was investigated for ambient conditions, high temperatures, and high pressures [Wec+09; Kat+10; Str+06; ODG94]. While these experiments show that phase transitions under static conditions can be observed with diffraction experiments with synchrotron and neutron sources, the observation of non-equilibrium phase transitions is limited. The question arises whether the molecular dynamics behave differently when driven in a fast pressure increase when compared to static conditions. XFELs with pulse durations below 100 fs [SSY00] are very well suited to answer this question.

The combination of X-ray holography [Sni+95; Clo+96] with X-ray diffraction proved to be a powerful tool for structural analysis over a broad range of spatial frequencies, for example to quantify the orientation of biological structures in cells [Nic+17]. While X-ray diffraction can give information on the molecular structure or orientation, nanofocus X-Ray nearfield holography (NFH) [Sal+15b; Sch+15] provides details on the microscopic level, with resolutions of down to sub-25 nm [Bar+15b] and field-of-views (FOV) of up to several 100 μm. NFH delivers quantitative contrast, as the phase images $\bar{\phi}$ obtained from holographic phase retrieval [Clo+99] are proportional to the projected electron density $\bar{\rho}_e$ of the sample. Seiboth et al. combined WAXS and X-ray holography at the XFEL to follow the dynamics of laser-induced shocks in germanium in a pump-probe scheme [Sei+18]. However, no quantitative analysis of the phase shift was done on the holograms, i.e. no phase was retrieved.

Compared to synchrotron experiments, holographic phase retrieval approaches at XFELs are especially demanding as the spontaneous nature of the SASE radiation poses an additional challenge for the emtpy-beam correction. An empty-beam-correction approach tailored for SASE fluctuations [Hag+21] has enabled quantitative holographic imaging with single-XFEL pulses of laser-induced dielectric breakdown in water in a μ-fluidic jet [Hag+21] and in bulk water (see chapter 3). With detailed quantitative analysis, the spatial and temporal pressure distribution inside the shockwave of laser-induced cavitation bubbles has been experimentally determined (see chapter 3) for the first time within nanoseconds after seeding. In a first step, the mass density of the compressed water in the shockwave was deduced from the X-ray phase shift, and in a second step, the pressure was calculated from the mass density using equations of state. In this approach, two premises have to be met to deduce the pressure inside the shockwave: (i) a prior assumption is necessary to reconstruct the 3d-shape of the cavitation bubble from a single projection image, and (ii) the calculation of pressure from mass density relies on the validity of equations of state for a broad pressure range.

Here, we combine WAXS and NFH with single XFEL pulses to investigate the dynamics of dielectric breakdown [Bre14] in a μ-fluidic water jet. In contrast to chapter 3 we use the information on the molecular structure obtained from the WAXS data, without prior assumptions, to quantitatively evaluate the pressure dynamics inside the water jet. We relate this information to the mass densities obtained from the quantitative phase retrieval of the holographic images to cover length scales from the molecular level to microscopic ranges.

4.2 Instrumentation and data analysis

The experiments were performed at the Materials Imaging and Dynamics (MID) instrument [Mad+21] of the European X-ray Free-Electron Laser [Tsc+17; Alt+06]. Focused nanosecond infrared (IR) laser pulses were used to induce dielectric breakdown in a μ-fluidic water jet (Fig. 4.1a). A pump-probe scheme with variable time delay Δt [Ost+21] was implemented to record both WAXS and NFH signals. In both configurations, WAXS as well as NFH, the IR laser was focused into the water jet (cf. section 4.5). With 6 ns pulse duration and 17 µJ pulse energy, the IR laser delivered peak intensities of about $\lesssim 3 \times 10^{10}\,\mathrm{W\,cm^{-2}}$. The XFEL was operated in single-bunch mode with 10 Hz repetition rate, at 17.8 keV photon energy, 660 µJ average energy per pulse, and a pulse duration of less than 100 fs [Alt+06; SSY00]. A stack of aberration-corrected, nano-focus compound refractive lenses (CRLs) [Sei+17a; Len+05; Sei+20] was used to focus the XFEL beam to a diffraction-limited focal spot [Sch+01; BS19] of 94 nm (FWHM). In NFH configuration (Fig. 4.1c), the water jet was positioned behind the X-ray focus in the diverging beam. The X-ray holograms were recorded by a sCMOS camera equipped with a fiber-coupled scintillator and was positioned on-axis in the diverging beam at 9.94 m distance behind the focus (Fig. 4.1d), resulting in a geometrical magnification of 36 and an effective Fresnel number of 1.71×10^{-3}. In WAXS configuration (Fig. 4.1a), the water jet was placed in the X-ray focus. Two off-axis charge-integrating hybrid pixel detectors (ePix100 [Dra+14; Kla+19]) recorded scattered photons in a scattering vector range of $q \approx 1.4\,\mathrm{\AA}^{-1}$ to $2.7\,\mathrm{\AA}^{-1}$ (Fig. 4.1b). The detectors were placed in the vertical and horizontal scattering plane, with main scattering components $\vec{q}_v$ and $\vec{q}_h$, respectively. The on-axis X-ray camera was used as an intensity monitor in WAXS configuration. Further details on the experimental setup are given in section 4.5. A detailed description on the timing and instrumentation is given in [Ost+21].

Next, we briefly sketch the processing steps for the phase retrieval of the holographic data. The spontaneous nature of the SASE process does not only result in strong pulse-to-pulse intensity fluctuations, but also in fluctuations of the modal composition of the wavefront, impeding a simple empty-beam division for NFH. We have shown in [Hag+21] that SASE pulses are well described by a low-dimensional configuration space, and more importantly, that for a given hologram an individual empty-beam image can be synthesized by a suitable linear combination of components from a principal component analysis (PCA) of a set of empty-beam images. The phase retrieval (PR) of the holographic images is described in detail in [Hag+21] and can be divided into the following two steps: (1) empty-beam correction with the PCA-based approach, and (2) phase retrieval with the iterative algorithm *alternating projections* (AP) [LBL02; HTS18]. Examples of an empty-beam corrected single-pulse hologram and the retrieved phase $\bar{\phi}$ are shown in Fig. 4.1d, e, respectively. Note that the retrieved phase $\bar{\phi}$ is proportional to the projected electron density of the sample, and thus proportional to the projected mass density of water.

The WAXS detection geometry was calibrated with a polycrystalline $\mathrm{LaB_6}$ sample

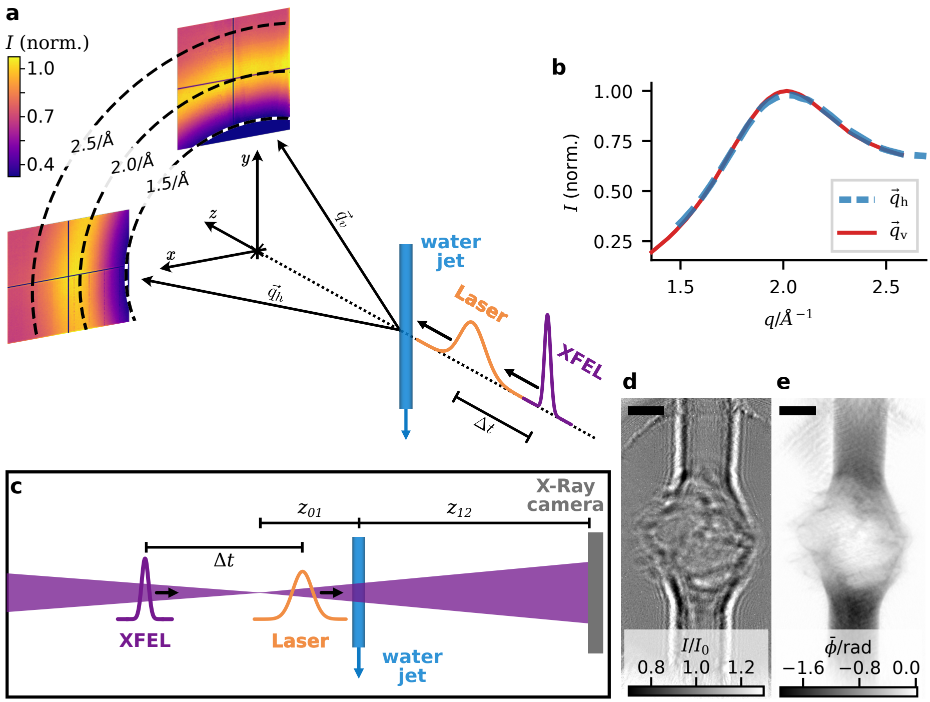

Fig. 4.1: Diffraction from a water jet – experimental setup. (a) A μ-fluidic water jet is excited by a focused nanosecond laser pulse and, after time delay Δt, probed by the XFEL pulse. For X-ray diffraction (WAXS configuration), the foci of the pump laser and XFEL beam are aligned to the same spot in the water jet. The main X-ray scattering contributions in vertical ($\vec{q}_v$) and horizontal ($\vec{q}_h$) direction are acquired on two pixel array detectors. **(b)** Normalized, azimuthally averaged intensity $I(q)$ of the signal for both detectors as shown in (a). **(c)** For X-ray holography, the water jet is illuminated by the diverging X-ray beam. The X-ray holograms are acquired with a scintillation-based camera. **(d)** Empty-beam corrected X-ray hologram of the perturbed water jet with $\Delta t = 9\,\mathrm{ns}$. **(e)** Phase shift $\bar{\phi}$ of (d) after iterative phase retrieval. Scalebar: 20 µm in (d, e).

(cf. Fig. 4.5). The intensity measurements were first corrected for a dark current by pedestal subtraction followed by a gain map correction to take gain variations between individual pixels into account (cf. Fig. 4.6). An X-ray polarization factor was applied to correct for the polarization dependent scattering amplitude (cf. Fig. 4.9). After azimuthal averaging, a low-pass filter suppressed high frequency noise (cf. Fig 4.8). Fig. 4.1a shows the corrected diffraction signal of unperturbed water on both detectors. The azimuthal average of the scattered intensity $I(q)$ (Fig. 4.1b) was normalized to the peak intensity.

The pulse-to-pulse SASE fluctuations do not only complicate the empty-beam correction of NFH, but also the analysis of the WAXS data. Variations in the total intensity are easily corrected using the intensity measured by the on-axis X-ray camera. However, slight fluctuations in the beam pointing of the XFEL result in varying background contributions of different optical elements. To mitigate these effects, the WAXS signal was averaged over multiple pulses, even though the signal-to-noise ratio of a single-pulse diffraction pattern was already sufficient. For further details on the analysis and data processing see methods section 4.5.

4.3 Results

Using the experimental system and data analysis schemes described above, a time-lapse series of (i) phase images and (ii) diffraction patterns was obtained. This data provides a quantitative insight into the the structural dynamics of the water at molecular scales following dielectric breakdown, combined with observations of the mesoscale hydrodynamics. In particular, it allowed us to deduce the non-equilibrium build-up of high pressures in the shockwave.

The pulse-averaged phase shift[1] $\langle\bar{\phi}\rangle$ (Fig. 4.2, color) visualizes the growing perturbation in the water jet after dielectric breakdown in a time series of images. Details on individual perturbations without pulse-averaging become apparent when inspecting the phase shift $\bar{\phi}$ retrieved from single-pulse holograms (cf. Fig. 4.1e). To highlight the variability of the dynamics from an individual perturbation (single-pulse phase shift $\bar{\phi}$), compared to the ensemble dynamics (pulse-averaged phase shift $\langle\bar{\phi}\rangle$), we display the difference phase shift $\Delta\bar{\phi} = \langle\bar{\phi}\rangle - \bar{\phi}$ (Fig. 4.2, gray scale) for a sequence of time delays Δt. A small cavitation bubble is visible in $\Delta\bar{\phi}$ at a time delay of 1 ns, followed by a fast expansion at later time delays Δt. Here, we do not only observe

---

[1] The averaged phase shift $\langle\bar{\phi}\rangle$ contains ~90 phase reconstructions of single-pulse holograms.

the dynamics of the elliptic growth of the perturbation, pushing the outer walls of the water jet apart, but also the fine details of water filamentation. A decrease in the magnitude of the average phase shift $\langle\bar{\phi}\rangle$, and hence a decrease in the projected mass density, starts to become visible at $\Delta t = 3$ ns. For later time delays, the projected mass density decreases further to a cavity with ellipsoidal shape.

Fig. 4.3 shows the diffracted intensity recorded in WAXS configuration for the same time delays as the NFH measurements. The diffraction signal is dominated by the oxygen atoms in the water molecules, with only very weak contributions from the hydrogen atoms. The diffracted intensity $I(q)$ is proportional to the scattering of a single oxygen atom, i.e. the squared form factor $f^2(q)$, and the coherent scattering of the oxygen atoms, described by the structure factor $S(q)$, hence $I(q) \propto f^2(q)S(q)$ [AM11]. The Fourier transform relates the structure factor $S(q)$ to the pair distribution function $g(r)$, describing the structure of the liquid phase in real space [AM11]. A change in the measured diffracted intensity $I(q)$ directly reflects changes in the structure factor $S(q)$ by short range liquid coordination of the water molecules. A time series of the diffracted intensity of the perturbed water jet I_{on} and the difference intensity $I_{\text{on}} - I_{\text{off}}$ between perturbed and unperturbed water is depicted in Fig. 4.3. Both scattering directions $\vec{q}_h$ and $\vec{q}_v$ show similar diffracted intensities, as expected based on the isotropic distribution of the water molecules, since the laser field is not intense enough to change the orientation of water molecules. The first slight shift in the diffracted intensity becomes apparent at a time delay of 2–3 ns and is clearly visible for time delays $\Delta t \geq 3$ ns. The magnitude of the main diffraction peak at $q \approx 2.0\,\text{Å}^{-1}$ decreases, whereas a second maximum appears at $q \approx 2.5\,\text{Å}^{-1}$, indicating a change in the molecular distances due to rearrangement of the molecules. The latter peak reaches its maximum intensity at about $\Delta t \approx 6$ ns, whereas the initial peak vanishes roughly at the same time delay. For later time delays, the overall diffracted intensity in the measured q-range shrinks. The vanishing initial peak indicates that the amount of water molecules in its initial ambient conditions (atmospheric pressure, room temperature) decreases, and more water molecules rearrange under different thermodynamic conditions, represented by the second peak. The decline in the total scattered intensity is most likely caused by an overall reduction of water along the beam path.

Comparing the diffraction signal with the NFH data, first changes are observed in the averaged signal at around $\Delta t = 2$ ns to 3 ns. The single-pulse holograms, however, show first changes already from $\Delta t = 1$ ns onward. There are two reasons for this: (1) The seeding rate at small Δt is lower, due to a spread of the time point of seeding within the beginning of the 6 ns-long pulse of the pump laser, i.e. not all cavitation

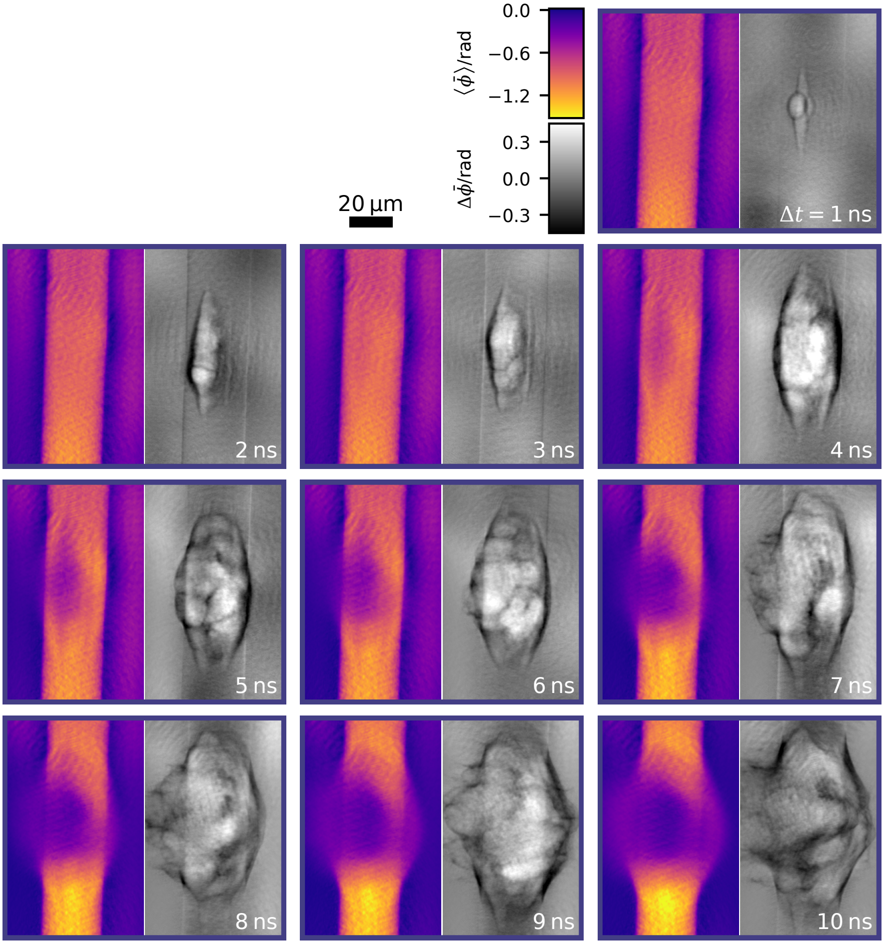

Fig. 4.2: Time series of phase-shift images from X-Ray holography. Pulse-averaged phase shift $\langle\bar{\phi}\rangle$ (color) and an exemplary difference phase shift $\Delta\bar{\phi} = \bar{\phi} - \langle\bar{\phi}\rangle$ (gray scale) for multiple pump-probe delays Δt after laser irradiation. The time series shows the growth of the perturbation in the water jet after dielectric breakdown.

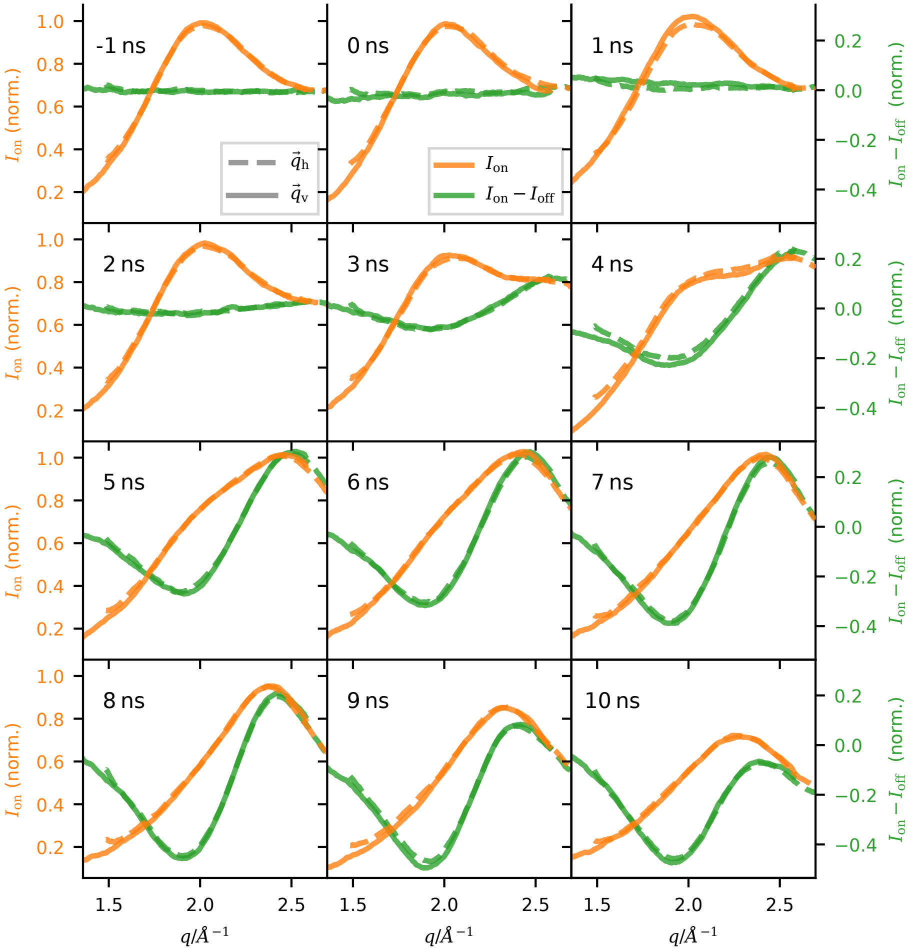

Fig. 4.3: Time series of the diffracted intensity. Diffracted intensity of the perturbed water jet (I_on, left ordinate, orange) and difference of the diffracted intensity with and without laser irradiation ($I_\mathrm{on} - I_\mathrm{off}$, right ordinate, green) for different values of the pump-probe delay Δt. Both detectors ($\vec{q}_v$, solid; $\vec{q}_h$, dashed) showed a similar change in the diffracted intensity. Time delays as in Fig. 4.2.

bubbles are seeded in the very early beginning of the laser pulse. (2) Variations in the position of the perturbation are on the same length scale as the perturbation itself, since the perturbation is still quite small for small Δt. In the NFH data, the decrease in the magnitude of the averaged phase-shift for $\Delta t \gtrsim 3$ ns implies a reduction of the projected mass density within the region of the perturbation. The decreasing number of water molecules along the beam path should manifest itself in a reduction of the total scattered intensity in the WAXS data, however, this decrease becomes clearly visible only at $\Delta t \gtrsim 8$ ns. This might be caused by the limited measured q-range.

In principle, the calculation of the pair distribution function $g(r)$ as the inverse Fourier transform of $S(q)$ would enable us to deduce thermodynamical quantities from the molecular arrangement in real space. This inversion, however, requires $S(q)$ to be measured over a large q-range, impeding the direct inversion of the present data. We therefore compared $S(q)$ obtained from the present experiment to published structure factors of water measured for different pressures and temperatures [Wec+09; Kat+10] to access the pressure dynamics in the water jet after dielectric breakdown. Both studies measured the diffraction of water under well-defined static pressure and temperature conditions in thermal equilibrium, using diamond anvil cells and synchrotron radiation. Weck et al. obtained data up to a pressure of 4.1 GPa (cf. Fig. 4.4a), whereas Katayama et al. measured up to a maximum pressure of 17 GPa. Their data shows a shift of the left-most peak (the peak at lowest q) of $S(q)$ towards higher values of q for increasing pressures p (cf. Fig. 4.4a). Using the data of [Wec+09; Kat+10], we extracted the position q_p of this peak from $S(q)$ for different pressures p and obtained an estimate of the functional relation q_p vs. p by fitting a power-law function to the data (cf. Fig. 4.4b and methods section 4.5 for more details). We did not take the influence of the temperature into account, as it has a negligible influence compared to the pressure (cf. data in [Kat+10]). The deduced power-law fit gives us a valid estimation of $q_\mathrm{p}(p)$ for values of $p \gtrsim 0.4$ GPa and thus enables us to determine pressure values from our data here with sufficient accuracy, despite its limited q-range.

Fig. 4.4c shows the structure factor $S(q)$ obtained from our measurements for different time delays Δt (cf. Fig. 4.10 for the full time series). We have calculated $S(q)$ from the diffracted intensity $I_\mathrm{on}(q)$ by division of the squared atomic scattering factor $f^2(q)$ for O^{2-} ions [Bro+04]. The structure factor was normalized to the maximum value of unperturbed water. At ambient conditions ($\Delta t \leq 0$ ns) we observed indications for the typical doublet structure (cf. Fig. 4.4a, c), albeit not entirely covered by the measured q-range. For intermediate time delays ($\Delta t \approx 4$ ns), the main peak of $S(q)$ shifts towards higher q, but a shoulder remains at the position of the initial maximum

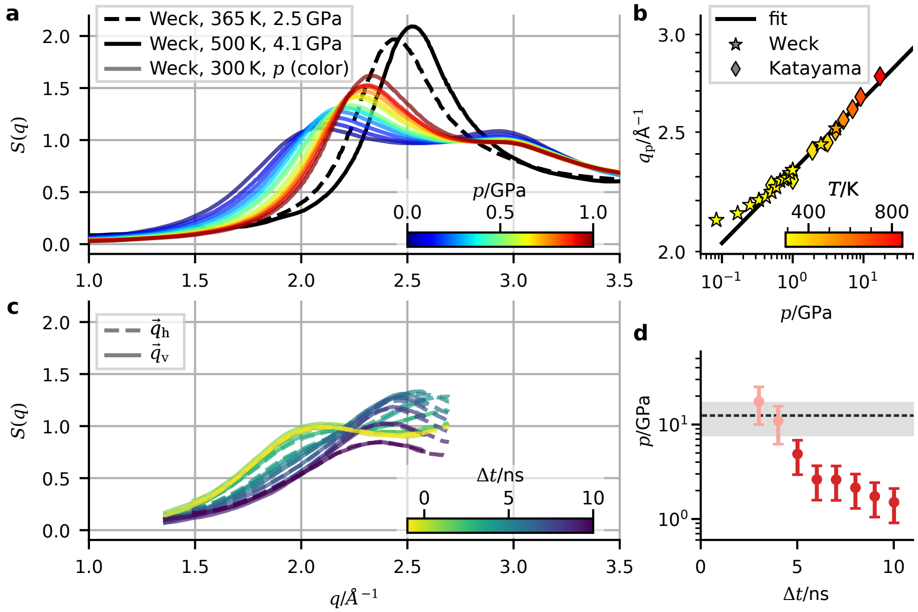

Fig. 4.4: Dynamics of the structure factor. **(a)** Structure factor $S(q)$ of water for different static pressure values p from Weck et al. [Wec+09]. **(b)** Position q_p of the main peak of $S(q)$ for different pressure values p on a double logarithmic scale. The peak position q_p was extracted from data of Weck et al. [Wec+09] (a) and Katayama et al. [Kat+10]. The power-law fit (black) yields a good approximation for pressure values of $p \gtrsim 0.4\,\mathrm{GPa}$. Only values with $p \gtrsim 0.4\,\mathrm{GPa}$ have been used for fitting. **(c)** Time evolution of the structure factor $S(q)$ of the water jet after dielectric breakdown obtained from our WAXS measurements $I(q)$ (cf. Fig. 4.3). $S(q)$ is normalized to the maximum value of $S(q)$ for unperturbed water (negative Δt). **(d)** Pressure evolution of the water jet after dielectric breakdown. The pressure values were calculated from the position q_p of the main peak of $S(q)$ from (c), using the power-law fit from (b). The error is dominated by the fit errors (error bars). The pressure values for $\Delta t = 3\,\mathrm{ns}$ and $4\,\mathrm{ns}$ (light red) were obtained from an extrapolation of the data to the peak position q_p, as q_p was outside or close to the edge of the measured q-range. The black-dashed line indicates the pressure value corresponding to the maximum q value within the measured range, the corresponding error interval is shown in gray.

($q \approx 2.05\,\mathring{A}^{-1}$), indicating a mixture of water at ambient conditions and water at higher pressures p. This observation agrees well with the holographic data, as the region of lower phase shift magnitude in $\langle \bar{\phi} \rangle$, corresponding to a lower mass density, covers roughly half of the diameter of the water jet for $\Delta t = 4\,\mathrm{ns}$. For longer time delays ($\Delta t \approx 6\,\mathrm{ns}$), the contribution of water at ambient conditions quickly vanishes and the structure factor is dominated by water at higher pressure. Again, this observation is supported by the holographic data, where the initial jet completely vanishes at a time delay between 6–7 ns leaving a diffuse cloud of lower mass density. At this delay, the main peak of $S(q)$ starts to shift towards lower values of q. The transition from the typical doublet structure to a single dominating peak can be attributed to a transition from a tetrahedral arrangement of the water molecules towards the molecular structure of a simple liquid, as reported before [SR00; Kat+10]. We extracted the peak position q_p from our measurements of $S(q)$ and used the power-law fit to calculate the pressure p for different time delays Δt (see methods section 4.5). For the time delays 3 ns and 4 ns the peak position q_p was outside or close to the boundary of the measured q-range of $S(q)$. We therefore manually extrapolated q_p for these two time delays. The resulting pressure evolution (Fig. 4.4d) shows a peak pressure of $\sim$10 GPa which quickly decays within 7 ns resulting in a pressure of $\sim$1.5 GPa. Note the impressive pressure differences of five orders of magnitude within the thin water jet at early time delays where parts of the jet are still at ambient conditions and parts of the perturbation are at $\sim$10 GPa. This observation is well supported by the NFH data (cf. Fig. 4.2).

4.4 Summary and conclusion

We have shown that single-pulse holography and WAXS at XFELs complement each other to obtain information over multiple length-scales, with time resolutions in principle only limited by the pulse length of the XFEL. Importantly, the molecular rearrangements and hydrodynamic effects at the mesoscale become jointly accessible. Similar to chapter 3, we were able to obtain images with quantitative contrast and fields of view on the order of $\sim$100 µm with single-pulse X-ray holography. The additional diffraction measurements gave access to the molecular structure, which we related to quantitative pressure values. In contrast to chapter 3, this approach thus enabled us to determine the pressure without any 3d inversion of the projected phase images. Importantly, the pressure values obtained from the diffraction data agree well with the pressure dynamics of cavitation bubbles after dielectric breakdown described in chapter

3. By comparing our data to data from literature measured at static pressures, we were able to attribute the change in the structure factor $S(q)$ after dielectric breakdown, resulting in a transition of the molecular structure from a tetrahedral arrangement to the molecular structure of a simple liquid [SR00; Kat+10].

For a direct calculation of the molecular arrangement described by the pair distribution function $g(r)$, measurements with a wider q-range are necessary. To this end, either the diffraction detectors could be replaced by detectors with a larger detection area (e.g. AGIPD-detector [All+15]) or a higher photon energy could be used. Comparing $g(r)$ to molecular dynamics simulations can further provide a tool to obtain a more complete picture of the thermodynamical state, including pressure as well as temperature. Moreover, the simultaneous observation of the macroscopic mass density by holography and the molecular arrangement and density by calculation of $g(r)$ from the diffraction data could provide a means to detect local 'defects' in the liquid structure or presence of domain boundaries. This is of particular interest for the observation of water in different density configurations and its transitions (LDL to HDL).

In this study the signal-to-noise ratio of single-pulse WAXS proved to be sufficient for a calculation of $S(q)$, even though background scattering prevented us from an analysis of the WAXS intensity on a single-pulse basis. With a better control of the background scattering, single-pulse diffraction [BFH18] would thus deliver insights in pressure dynamics without ensemble averaging. This would enable to determine $g(r)$ with a time resolution only limited by the pulse length of the XFEL (less than 100 fs), providing the possibility of movies with molecular time resolution [NM12]. This is of particular interest for the observation of molecular rearrangements during the early plasma states of cavitation after dielectric breakdown. Experiments with better time resolution would additionally require to use a pump-laser with pulse durations of femtoseconds.

To conclude, we have combined two X-ray methods at the XFEL to study the dynamics of water after dielectric breakdown. This allowed us to relate structural information at the molecular scale and corresponding thermodynamical states to quantitative images at microscopic length scales. The quantitative character on length scales from the molecular to microscopic level and the possibility to observe ultrafast dynamics, make this method a promising tool for the observation of fast dynamics in strongly driven matter.

Acknowledgments: M.V. and T.S. are members of the Max Planck School of Photonics supported by BMBF, Max Planck Society, and Fraunhofer Society, which has also funded consumables and instrumentation for the cavitation and optical setup. We acknowledge funding of the nanofocusing setup at MID by BMBF project 05K13OD2 *Erzeugung und Charakterisierung von nanofokussierten XFEL-Pulsen zur Abbildung ultraschneller Prozesse in Materie* and for the IR-laser by BMBF project 05K16RF2 *Mikroskopische Flüssigkeitsstrahlen zur Untersuchung der Dynamik und Kinetik struktureller Nichtgleichgewichtsphasenübergänge am Europäischen Freie-Elektronen-Laser*. We thank Peter Luley and Jan Goemann for technical help. The authors thank the European XFEL in Schenefeld, Germany for granting beam time for this project. The engineering team and technicians at the MID instrument are gratefully acknowledged for help in setting up the experiment. This research was supported in part through the Maxwell computational resources operated by DESY.

4.5 Methods

4.5.1 Experimental details

XFEL specifications: The experiments have been performed at the Materials Imaging and Dynamics (MID) instrument [Mad+21] at the European X-ray Free-Electron Laser [Tsc+17; Alt+06]. The linear accelerator of the XFEL accelerated the electrons to an energy of 16.5 GeV into the 175 m-long undulator. A repetition rate of 10 Hz with one pulse per train was used. The undulator delivered photons with an energy of 17.8 keV. The resulting SASE pulses had a pulse width of less than 100 fs [Alt+06; SSY00] and an average pulse energy of 660 μJ.

X-ray optics: A stack of 50 beryllium compound refractive lenses (CRLs) [Len+05], aberration corrected by a customized phase plate [Sei+20; Sei+17a], focused the XFEL pulse to an diffraction limited focal spot of 94 nm [Sch+01]. The CRL stack had a focal length of 475 mm, with a numerical aperture of 2.7×10^{-4}. For further details on the experimental parameters see [Ost+21], and [Hag+21] for a detailed characterization of the illumination.

X-ray detectors: An Andor Zyla camera (Zyla 5.5, Andor, Abingdon, United Kingdom) was used for the holography measurements. The camera had a LuAg:Ce scintillator (thickness 20 µm), which was coupled to the sCMOS chip with a fiber-optic plate with a pixel size of 6.5 µm. The sample to detector distance was $z_{12} = 9670$ mm. An 8 m long evacuated flight tube reduced air absorption between sample and detector.

For the diffraction measurements two ePix100 detectors [Dra+14; Kla+19] were used. The ePix100 is a charge-integrating hybrid pixel detector and consisted of four modules with 384×352 pixels each. The pixel size was 50 µm. The distance between the water jet and the ePix detectors was 250 mm and the detectors were arranged in an angle of $\sim$12.5° towards the X-ray focus.

X-ray holography: For the holographic measurements, the water jet was placed in a defocus position of $z_{01} = 271.3$ mm behind the CRL focus, resulting in a geometrical magnification of $M = 36$, an effective pixel size of 177 nm, and an effective Fresnel number of $F = 1.71 \times 10^{-3}$. See [Hag+21] for further details.

Laser and laser optics: The pump laser (Nano L 200-10, Litron, Lasers, Rugby, United Kingdom) had a wavelength of 1064 nm, pulse length of 6 ns, and a maximum pulse energy of 200 mJ. An internal attenuator reduced the pulse energy to 17 mJ. The focusing optics had a numerical aperture of 0.2 The focal spot was expected to exceed the diffraction limited spot size of 1.7 µm (radius $1/e^2$-intensity beam waist) due to aberrations from a through-hole mirror between focusing lens and water jet. The through-hole mirror was used to get a co-linear alignment of the pump laser and the X-ray beam.

µ-fluidic water jet: A µ-fluidic jet (Microliquids GmbH, Göttingen, Germany) with a nozzle diameter of 40 µm was used. The jet nozzle creates a laminar water flow and is connected to a pump (PU-2080, JASCO GmbH, Pfungstadt, Germany) with a flow rate of 20 mL min^{-1}. We used de-ionized water.

Timing: The timing scheme and equipment is described in great detail in [Ost+21]. Here, we will only summarize key parameters. A low jitter delay generator (DG535, Stanford Research Systems, Sunnyvale, CA, USA) controls the pump-probe delay between the XFELs master clock and the Pockels cells of the pump laser. A second delay generator (DG535) was used to keep the delay between the laser's flash lamp and Pockels cell constant at 160 µs for maximum laser output.

Data acquisition WAXS: To avoid artefacts from a systematic drift in any optical component, we measured the same time delay Δt multiple times in a randomized order. To this end, we acquired 10 measurement blocks for each Δt. One block contained $\sim$50 frames. In between these blocks, we acquired $\sim$40 frames of reference signal without pump-laser output. In total we acquired 210 of these blocks for delays between -10 ns and 10 ns in steps of 1 ns and 10 blocks for each delay.

4.5.2 Data processing – diffraction data

The WAXS detection geometry was calibrated with a polycrystalline LaB_6 sample (cf. Fig. 4.5). The intensity measurements were first corrected for a dark current by pedestal subtraction followed by a gain map correction to take gain variations between individual pixels into account (cf. Fig. 4.6). An X-ray polarization factor was applied to correct for the polarization dependent scattering amplitude (cf. Fig. 4.9). After azimuthal averaging, a low-pass filter suppressed high frequency noise (cf. Fig 4.8). Fig. 4.1a (main manuscript) shows the corrected diffraction signal of unperturbed water on both detectors. The azimuthal average of the scattered intensity $I(q)$ (Fig. 4.1b) was normalized to the peak intensity.

Calibration of the detection geometry: The detection geometry was calibrated with powder diffraction measurements of a polycrystalline LaB_6 sample. Fig 4.5a, b clearly shows the $(1\,0\,0)$, $(1\,1\,0)$ and $(1\,1\,1)$ diffraction ring of the LaB_6 sample on the $\vec{q}_h$ and $\vec{q}_v$ detector, respectively. We fitted three circles with common center position to the diffraction rings on both detectors to determine the detection geometry with respect to the diffraction center. The result is shown in Fig. 4.5c. With this diffraction center, the azimuthal average of the detected intensities yields $I(q)$ (Fig. 4.5d). The calculated positions of the $(1\,0\,0)$, $(1\,1\,0)$ and $(1\,1\,1)$ diffraction peaks for LaB_6 with a lattice constant of 4.16 Å [MAT13] are shown.

Note that the images in Fig 4.5a, b are not background corrected, only the pedestal was subtracted, such that they give a good impression on the background intensity due to scattering at optics and other elements. For example, the vertical blue line in Fig 4.5b results from a shadowing of the background scattering at the nozzle of the µ-fluidic jet.

Detector pedestal and gain-map correction: The pixels of the ePix100 detectors accumulate charge linear to the photon energy incident during the acquisition. Each

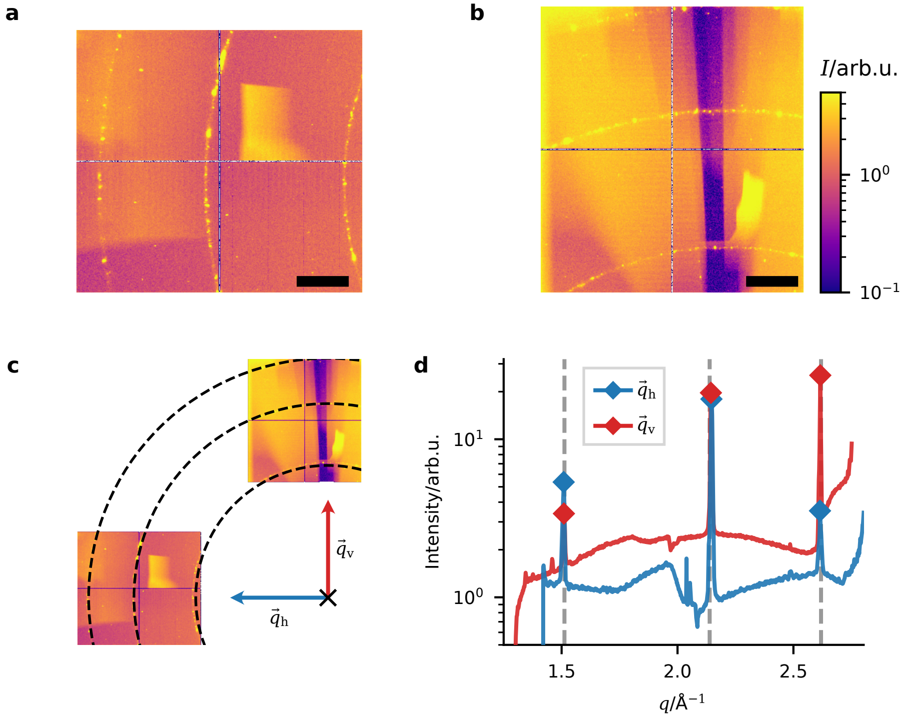

Fig. 4.5: Calibration of the detection geometry. (a, b) Detected intensity of polycrystalline LaB_6 sample after pedestal subtraction for the $\vec{q}_h$ and $\vec{q}_v$ detector, respectively. The powder diffraction rings of the LaB_6 structure are clearly visible on both detectors. In addition, the images give a good impression of the strong background scattering present in the experiments. **(c)** Optimized geometry of both detectors. The circles (black, dashed) correspond to the circles fitted to the diffraction rings, to calibrate the detection geometry. **(d)** Diffracted intensity after azimuthal integration of (a, b). The vertical lines (gray, dashed) indicate the position of the LaB_6 diffraction peaks from literature [MAT13]. The diamonds mark the experimentally determined peak positions. Scalebars: $0.2\,\text{Å}^{-1}$ in (a, b).

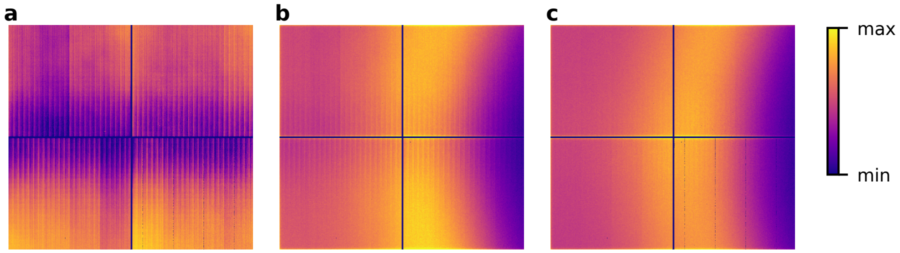

Fig. 4.6: Gain-map correction of the ePIX100 detectors. The gain map **(a)** represents the conversion gain per incident 17.5 keV photon for each individual pixel. Strong variations appear between adjacent pixel columns and sub modules of the detector chip and in vertical direction towards the intermodular gap. **(b, c)** Normalized intensity of water diffraction at the $\vec{q}_h$ detector without and with gain correction, respectively. In (a) the color scales linearly with the gain in a range of 250–350 ADU ph^{-1}, and in (b, c) with the normalized intensity in a range of 0.3–1.6 .

pixel has to some extent its own readout electronics, leading to different gain factors g_{ij} and pedestals p_{ij} (dark current). The pedestal can easily be corrected by a subtraction of dark images. The correction of different gain factors requires the calculation of a gain map.

With monochromatic radiation and low incident flux, the gain map can be calculated by determination of the single photon charge value from pixel-wise histograms. Fig. 4.6a shows the gain map of the $\vec{q}_h$ detector with gain variations of $\sim$15 %. The gain-map-corrected intensity measurement shows homogeneous scattering intensity along the diffuse diffraction ring of water, whereas intensity variations are visible in the uncorrected image (cf. Fig. 4.6b, c).

Correction of pulse-to-pulse intensity fluctuations: The SASE process leads to strong pulse-to-pulse intensity fluctuations. As the total scattered intensity measured at the ePix100 detectors was not constant with Δt, an external intensity reference was needed. To this end, we corrected each single-pulse diffraction signal by the total intensity measured with the on-axis Zyla camera.

Background subtraction and signal calculation: The signal of our interest is the combined signal of the laser-induced perturbation and the unperturbed water jet $\Sigma_{\text{pertub}} + \Sigma_{\text{jet}}$. The easiest way to obtain this combined signal would be to measure the intensity with pump laser and water jet I_{on} and the background intensity with neither pump laser nor water jet active I_{BG} and simply deduce $\Sigma_{\text{pertub}} + \Sigma_{\text{jet}} = I_{\text{on}} - I_{\text{BG}}$. We have to consider, however, that the background intensity is not constant over time due to drifts, so that I_{BG} would have to be measured directly before or after the pump-probe experiment. As we lack this direct measurement of the background, we complemented our overall intensity I_{on} with the intensity obtained in between pump-probe intervals I_{off} after switching off the pump laser (cf. section 4.5.1), but leaving the water jet running. In an independent measurement we obtained the intensity with water I_{off} and the background intensity I_{BG} in subsequent measurements. We thus end up with $\Sigma_{\text{pertub}} + \Sigma_{\text{jet}} = I_{\text{on}} - I_{\text{off}} + \Sigma_{\text{jet}} = [I_{\text{on}} - I_{\text{off}}]_{t_1} + [I_{\text{off}} - I_{\text{BG}}]_{t_2}$, where t_1 and t_2 indicate the different points in time of acquisition.

Detector mask: Some regions on the ePix100 detectors experienced strong pulse-to-pulse fluctuations in the scattering background or pedestal. These areas have been excluded from the analysis (cf. Fig. 4.7).

Signal filtering: The $I(q)$ intensity measurements are filtered by a Savitzky-Golay filter (*savgol_filter* of SciPy's signal module (v. 1.5.4) [Vir+20], with parameters *polyorder*: 0, *window_length*: 51). The window length of 51 pixels corresponds to a length in q of $\sim$0.09 Å^{-1}. Fig. 4.8 shows a comparison of filtered and unfiltered $I(q)$ for three values of Δt.

Polarization correction: The amplitude of the scattered field depends on the polarization of the incoming X-ray wavefield. For horizontally polarized X-rays, the full scattering amplitude would only be observed along the vertical axis, i.e. for values of $\vec{q}$ without any contribution in the horizontal direction $\vec{q}_h$. The polarization factor and polarization correction for area detectors is well described in [Jia15]. Let $2\Theta_h$ and $2\Theta_v$ be the scattering angle in the horizontal and vertical plane, respectively. The polarization factor P_h for horizontally polarized X-rays is then given by [Jia15]

$$P_h = 1 - \cos^2(2\Theta_v)\,\sin^2(2\Theta_h)\,.$$

We assume horizontal polarization of the X-rays generated within the undulator. Fig. 4.9 shows the polarization factor for the $\vec{q}_h$ detector and the influence on the diffracted intensity $I(q)$.

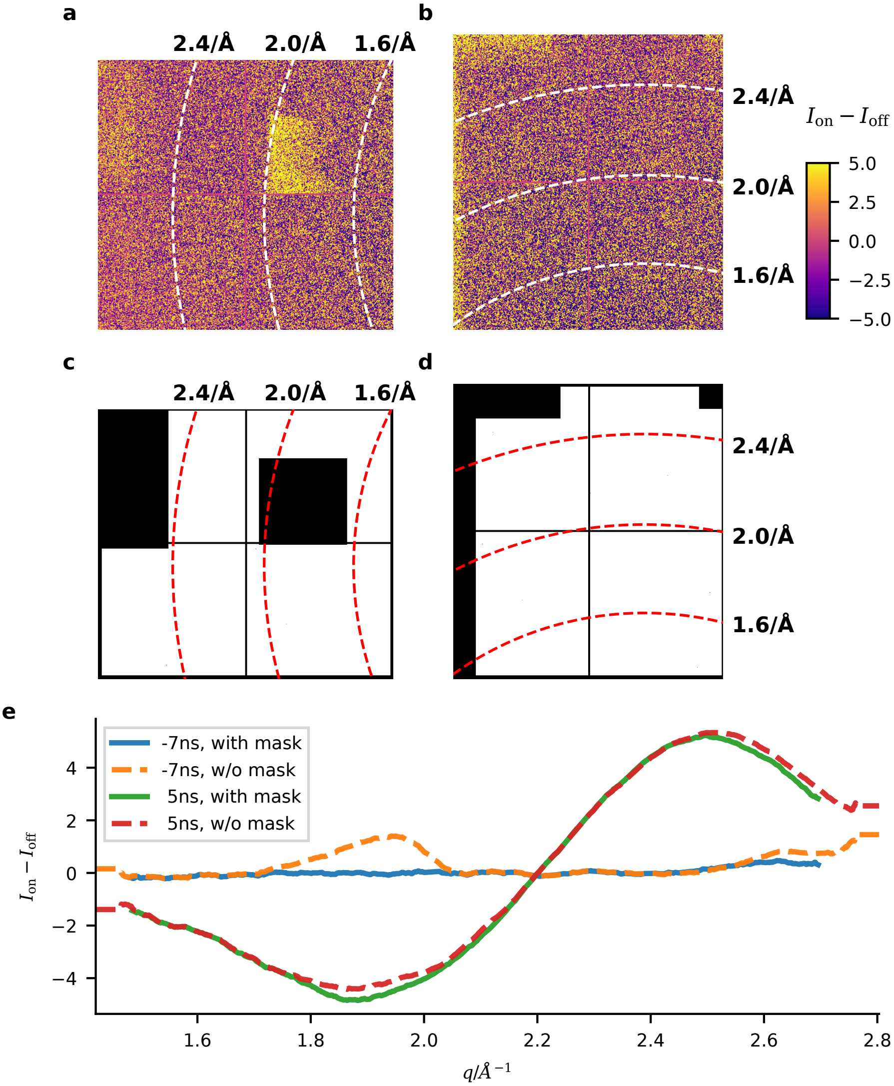

Fig. 4.7: Masked areas on the diffraction detectors. Areas with strong fluctuations of the background scattering or pedestal are excluded from further analysis. **(a, b)** show the difference intensity $I_{\text{on}} - I_{\text{off}}$ for $\Delta t = -7$ ns (unperturbed water) measured by the $\vec{q}_h$ and $\vec{q}_v$ detector, respectively. Regions with strong background fluctuations are excluded from further analysis, indicated by the black regions in **(c, d)** for the $\vec{q}_h$ and $\vec{q}_v$ detector, respectively. **(e)** Angularly averaged and filtered intensity $I(q)$ of the $\vec{q}_h$ detector for two delays Δt with and without mask (c). The difference intensity in (a, b) and (c) scales in arbitrary units.

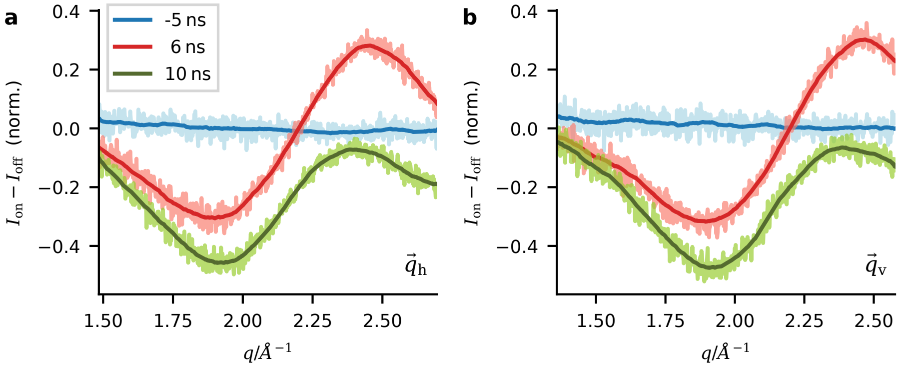

Fig. 4.8: Signal filtering. Comparison of unfiltered (light colors) and filtered (dark colors) intensity difference $I_{\mathrm{on}} - I_{\mathrm{off}}$ for three values of Δt. The Savitzky-Golay filter reduces high-frequency noise but leaves the low-frequency variations unchanged. **(a, b)** $\vec{q}_h$ and $\vec{q}_v$ detector, respectively.

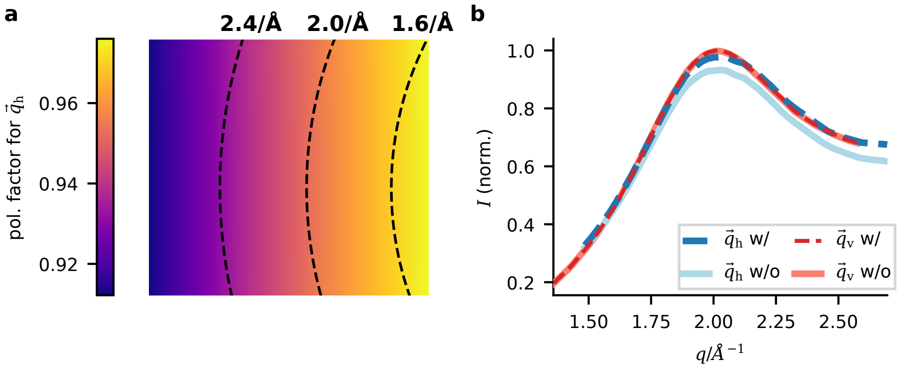

Fig. 4.9: Polarization correction. (a) Polarization factor for the $\vec{q}_h$ detector with its main scattering contribution parallel to the X-ray polarization. **(b)** Normalized intensity of water diffraction with and without polarization correction for both detectors. The polarization factor deviates by less than 0.01 from unity on the $\vec{q}_v$ detector with its main scattering contribution perpendicular to the X-ray polarization.

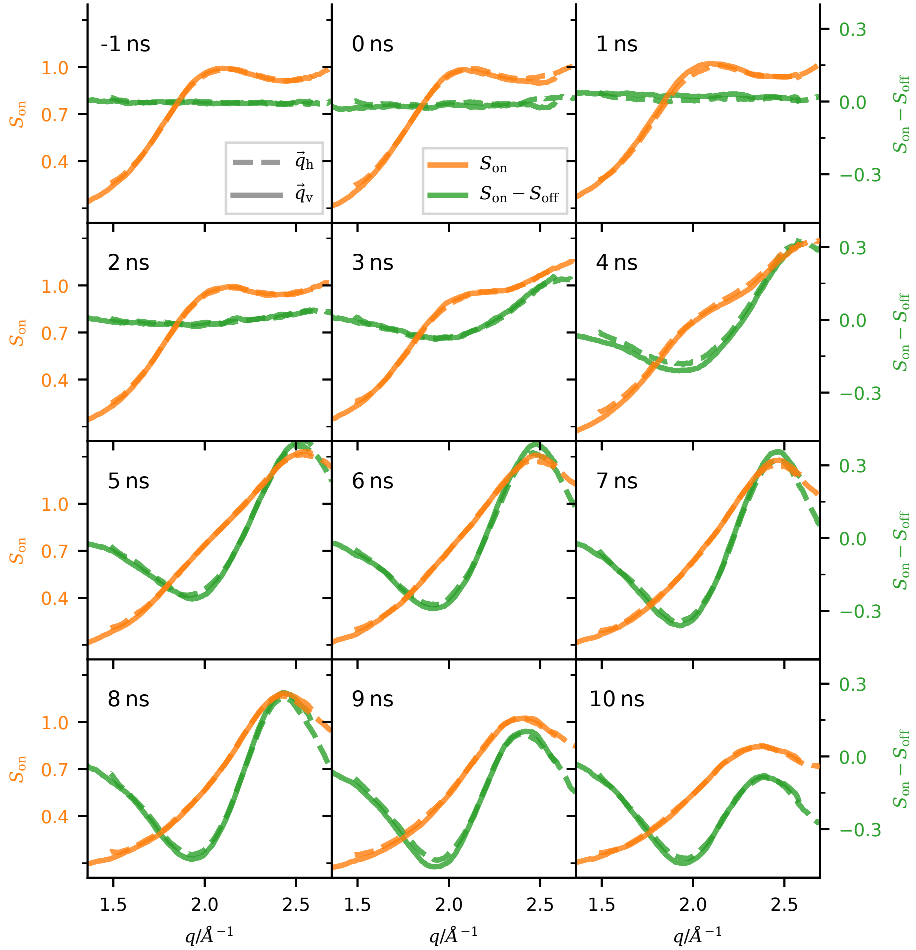

Fig. 4.10: Time series of the structure factor. Normalized structure factor of perturbed water with pump-laser irradiation (S_on, left ordinate) and the difference structure factor between perturbed and unperturbed water $S_\mathrm{on} - S_\mathrm{off}$ (right ordinate) for different pump-probe delays Δt. The structure factor is normalized to the maximum value of unperturbed water.

Power-law fit for pressure determination from the peak positions of the structure factor: To relate the position q_p of the left-most peak of the structure factor $S(q)$ to specific pressure values, we used a power-law fit to describe the peak position q_p as a function of the pressure p, which we extracted from the structure factors reported by Weck et al. [Wec+09] and Katayama et al. [Kat+10]. To this end, we first digitized $S(q)$ from the manuscripts using [Roh20] and determined the peak position q_p. We fitted the following function to the data in Fig. 4.4b with pressures $p \geq 0.4\,\mathrm{GPa}$

$$\log_{10}\left(q_\mathrm{p}/\mathrm{\AA}^{-1}\right) = m \cdot \log_{10}\left(p/\mathrm{GPa}\right) + b.$$

The least-square fit converged for the values $m = 0.059(2)$ and $b = 0.3665(9)$. With this fit we calculated the pressure evolution $p(\Delta t)$ from the peak positions q_p of the structure factor (cf. Fig 4.4c, d and Fig. 4.10) determined from our intensity measurements. The error of the pressure values is dominated by the fit errors.

4.5.3 Data processing – holography

The data processing, empty-beam correction and phase retrieval of the X-ray holograms is described in great detail by Hagemann et al. in [Hag+21]. Here, we will only briefly sketch the involved steps.

Empty-beam correction: A series of empty-beam images ($\sim$150 images) is acquired directly before and after the measurement of the holograms with the pump laser switched on. The empty-beam correction is based on the components of a principal component analysis (PCA) of the empty-beam series. For each hologram, a reference image is calculated from the first 30 components of the PCA, which is then used for empty-beam division. This approach was first described for data acquired at synchrotrons [Van+15] and was adapted to data from XFELs in [Hag+21].

Phase retrieval: The object's phase shift, encoded in the empty-beam corrected X-ray holograms, is retrieved by the iterative phase retrieval algorithm *alternating projections* (AP) [LBL02; HTS18]. The algorithm projects the object's guess alternatingly onto a measurement constraint, the intensities of the empty-beam corrected hologram, and a sample constraint, the spatial limitation of the object by a compact support. Two additional sample constraints are used: The range constraint, limiting the phase shift to $\bar{\phi} \in [-10, 0]$ rad, and the homogeneous object constraint with prior knowledge of the δ/β-ratio of water, where δ and β is given by the refracting and absorbing part of the index of refraction $n = 1 - \delta + i\beta$. The phase retrieval is then divided into two stages: In a first stage, the support for the sample constraint is determined, with a maximum number of 500 iterations. In a subsequent second stage, this support is used to calculate the object's phase shift with a maximum of 4000 iterations.

Conclusion and outlook

5

In the present work we have reported on experiments involving the full range of available X-ray sources. On the side of table-top experiments, we have presented a novel approach to substantially improve brightness and lateral coherence when generating X-rays in a laboratory setting. On the other hand, we have exploited the tremendous peak brilliance offered by an XFEL to observe the fast dynamics of non-equilibrium phase transitions in water after dielectric breakdown with single-pulse X-ray nearfield holography and X-ray diffraction. With this combined approach we were able to obtain quantitative information from the microscopic length scale to the molecular level with a time resolution, which was only limited by the pulse duration of the optical pump laser.

Brightness of the waveguide source: In chapter 2, we have reported on a novel X-ray source concept to generate spatially coherent X-rays directly inside a planar X-ray waveguide. The mode densities of the waveguide influenced the angular emission spectrum of both the characteristic radiation and bremsstrahlung. We estimated the brightness of such a waveguide source to 5×10^{11} ph mrad^{-2} mm^{-2} per characteristic K lines, when operated at optimal conditions. The estimated brightness of our waveguide source exceeds the gallium K-line brightness of a liquid-metal jet X-ray tube which was measured to be $\sim 1 \times 10^{10}$ ph mrad^{-2} mm^{-2} for the K$_\alpha$ line [Ote+08] and rivals with the brightness of an inverse-Compton-scattering (ICS) X-ray source of $\sim 4 \times 10^{11}$ ph mrad^{-2} mm^{-2} at a spectral bandwidth of $\Delta E_{\mathrm{ph}}/E_{\mathrm{ph}} \approx 3$–$5\,\%$ [Hor+19; Egg+16]. Note that the latter source is lab-sized as it consists of a compact storage ring with a circumference of 4.6 m, whereas the liquid-metal jet and waveguide source are very compact and table-top systems.

This comparison is quite remarkable as the estimation of the brightness for the waveguide source was based on the current waveguide design and did not include any further optimization of the structure. An optimization could include the design of waveguides with higher quality factor Q by an advanced choice of the layer materials as well as an improved heat management. The heat dissipation is a crucial part in

X-ray tubes as it limits the maximum power density of the electron beam [Beh16]. The high thermal conductivity of diamond is exploited for X-ray tubes with anodes in transmission geometry, where a thin metal layer of $\sim 0.5\,\mu\mathrm{m}$ thickness is deposited on a diamond substrate (e.g. [Nac+14]), as well as for self-absorption-reduced X-ray anodes [YKL16]. In the latter case the Heel effect [Beh16], describing self-absorption inside the anode, is reduced by embedding metal lamellae in a diamond matrix. Our current waveguide design uses a silicon substrate. The substrate can be replaced with synthetic diamond without influencing the optical properties of the waveguide. In addition, with only little changes to the optical properties, the carbon guiding layer can be replaced by synthetic diamond as well. This would increase the thermal conductivity by approximately a factor of 10 for both, the substrate and the guiding layer [Lid+95]. A 10-times better thermal conductivity is directly related to the possibility to increase the surface power density of the electron beam by a factor of 10, when operated at the same temperature [GWA86]. Diamond substrate and diamond guiding channel thus promise a brightness increase by a factor of 10 compared to our estimation.

Pulsed laser-plasma sources for X-ray generation in waveguides: The waveguide anode is not restricted to electron beams from simple electron guns. A promising possibility to generate short X-ray pulses with high lateral coherence and high brightness would be to use the waveguide as a solid target in a laser-plasma X-ray source by focusing a short laser pulse to the surface of the waveguide. Solid-target laser-plasma X-ray sources [Rou+94] exploit the acceleration of electrons in a plasma by an ultrashort laser pulse when focused onto the surface of the target. In a first step, an early part of the laser pulse generates a plasma on the surface of the target. The laser pulse further accelerates the plasma electrons, so that these hot electrons penetrate the target, leading to the generation of bremsstrahlung and characteristic radiation [Gib05]. This last step is similar to the processes in anodes of X-ray tubes. Nevertheless, in contrast to X-ray tubes there is no cut-off energy of the electron spectrum. The energy distribution of the hot electrons shifts towards higher energies for increasing laser intensities [Sal+02]. This imposes an optimum intensity I_{opt} for K_α generation [Rei+00], as the K_α photons are generated in deeper layers of the solid target for higher electron energies and thus experience stronger self-absorption [Sal+02]. As a consequence, an increasing pulse energy of the laser with constant focus size leads to a saturation of the K_α intensity in reflection geometry and thick targets, and even to a decreasing intensity in transmission geometry with thin targets [Sal+02]. On the other hand an increasing pulse energy at constant intensity I_{opt} and thus with increasing focus size leads to an increase in K_α emission. However, the increasing laser spot and thus the larger X-ray source spot reduces the K_α brightness increase. A planar waveguide as laser-plasma target can decouple the X-ray source spot and the laser spot along one dimension (cf. Fig. 2.7). At increasing pulse energies, this could allow optimization of the laser intensity, by e.g. a line focus, without increasing the X-ray source spot. This would directly enhance the brightness of the X-ray source. The target material is ablated in the process of plasma generation, however, so that the target needs to be replaced in between laser pulses. In the case of planar waveguides this could be implemented by scanning the waveguide structure through the laser focus. When using the waveguide beam leaving the structure through the top layer by resonant beam coupling, a planar waveguide with a wafer size of 20 mm × 100 mm could provide on the order of 10^5 pulses depending on the size of the laser focus[1].

The pulse duration of the X-ray flash generated in a laser-plasma source depends strongly on the thickness of the target. A thick target can produce a long afterglow of up to several picoseconds even if the laser pulse is much shorter, until all the electrons have been decelerated to a kinetic energy below the K-shell ionization energy. For a target thickness of up to $\sim 3\,\mu\mathrm{m}$ about 90 % of the radiation can be emitted within the first ~100 fs [Rei+00; Rei+01]. The total thickness of all layers of planar X-ray waveguides and waveguide arrays is below $\sim 3\,\mu\mathrm{m}$. The substrate supporting the waveguide is however substantially thicker. To obtain short X-ray pulses without a long afterglow from such a target one has to reduce the contribution of the substrate. A material with low atomic number leads to a characteristic radiation below the hard X-ray regime and a less efficient generation of bremsstrahlung in the high photon energy range [Beh16] and thus reduces the afterglow in the hard X-ray regime. Silicon and especially diamond as substrate material are a proper choice with a K_α energy of 1.7 keV and 0.3 keV [Sch+11], respectively. Furthermore, when using the modes leaving the waveguide through resonant beam coupling, the grazing observation angle leads to severe self-absorption inside the substrate and additionally reduces the afterglow from the substrate. In conclusion, laser-plasma X-ray generation inside waveguides could improve the brightness of laser-plasma X-ray sources.

Beyond planar structures: So far we have only demonstrated X-ray generation in a planar (1d) waveguide. The radiation emitted from these structures has high lateral coherence in one direction only. Depending on the application this is not necessarily a

---

[1] Here we estimated the distance between adjacent pulse positions on the target to be 400 μm along the direction of the line focus and 50 μm in the perpendicular direction

disadvantage. X-ray diffraction at surfaces or stacks of membranes [Sal+03; NGS06] for example, only requires coherence along one dimension. Also for X-ray tomography, we have developed a scheme for acquisitions with anisotropic sources in a previous work [Vas+16]. Using X-ray generation in a waveguide, there are several possibilities, how the spatial coherence could be enhanced in the orthogonal direction. Two approaches easy to implement are (i) to use an electron line focus and observe in the direction parallel to the line focus or (ii) to use one-dimensional X-ray optics or slits to narrow the source spot.

As discussed in chapter 2 also the use of channel (2d) waveguides is possible, promising even higher gains. The technical realization is quite sophisticated, however. Similar to the planar waveguide case, an additional material needs to be embedded in the guiding core to generate X-rays directly inside the core of a 2d waveguide. This process is challenging as 2d waveguides are commonly manufactured by etching channels into silicon [Neu+14; CHS15]. A possible alternative would be to fill the channel with a polymer and embed a metal inside this polymer. As for planar waveguides, X-rays can also be generated in the cladding of a channel waveguide, which seems straightforward to implement. A challenge arises from the commonly used cladding material silicon, which has a K_α energy below the hard X-ray regime, so that it needs to be replaced by a material with higher atomic number but similar properties for etching and bonding. Candidates are for example germanium [Hof+16] or probably gallium arsenide, due to the availability of wafers with high surface quality. Another approach to fabricate channel waveguides, well suited for the generation of X-rays in the cladding, would be to deposit a thin layer of metal inside the channels etched in silicon. In early designs of channel waveguides, a thin line of polymer was embedded in a metal cladding [Pfe+02; Jar+05], a concept that seems very attractive for generating X-rays in the cladding.

Once the technical challenges for channel waveguides are solved, X-ray generation in waveguides beyond straight channels like tapered channels [CHS15], beamsplitters [HS16], split-and-delay lines or bent channels [Sal+15a] can provide entirely new possibilities for source designs. This toolbox of optics on a chip can be especially interesting for quantum optical experiments with hard X-rays at table-top instruments. Also the coherent preparation of the incoming electron beam could add an interesting element to these types of experiments in 1d or 2d waveguides.

Stimulated emission in waveguides: The excitation of X-ray fluorescence inside a waveguide by an ultrashort and highly intense XFEL pulse could be interesting in terms of stimulated emission and population inversion. Population inversion has been first observed for soft X-rays for the K_α transition in neon [Roh+12]. A recent work proposed the design of a population inversion hard X-ray laser pumped by an XFEL [Hal+20], for further reading see [Roh17]. Let us assume a planar waveguide with a thin ∂-layer of metal in the center of the guiding core and an XFEL pulse coupled resonantly to the zeroth mode, resulting in a field magnification inside the waveguide. As we have shown, X-ray fluorescence excited inside the waveguides has similar properties as characteristic radiation generated inside the same structures. With a photon energy of the XFEL pulse slightly above the K-edge of the ∂-layer, a high number of metal atoms can experience K-shell ionization. With a lifetime of $\sim$1 fs, the excited atoms will emit a fluorescent photon from which a fraction, as we have shown, is coupled into the zeroth mode of the waveguide again. The fluorescent photons in the zeroth mode propagating into the same direction as the XFEL beam will co-propagate with the XFEL pulse, will hit atoms with excited K-shell, and induce the stimulated emission of a photon. This means that a pulse with very narrow bandwidth obtained from stimulated emission builds up behind the XFEL pulse. Population inversion in such a system might require an XFEL intensity increase above the damage threshold of the waveguide. Following the concept of diffract before destroy from X-ray diffraction with XFEL radiation [Neu+00], the destruction process, however, is slower than the build-up of the population inversion and the emission of the stimulated X-ray pulse.

X-ray holography with single XFEL pulses: In chapter 3 and 4 we have exploited the capabilities of X-ray sources with highest peak brilliance available today to observe fast dynamics with high temporal and spatial resolution. We have investigated the dynamics of the transient phase transition after dielectric breakdown in bulk water with holography and in a μ-fluidic water jet with a combined approach of holography and X-ray diffraction.

We were able to calculate the density and pressure distribution of the shockwave surrounding the cavitation bubbles from the X-ray holograms that we obtained with each individual XFEL pulse. The time resolution was thus only limited by the pulse length of the nanosecond pump laser.

Spatial resolution: A spatial resolution better than 460(20) nm (HWHM) was obtained in the retrieved phase images (cf. Fig. 3.8) , which is already superior to the resolution at optical wavelengths with working distances long enough for the geometric constraints imposed by the water cuvette. Estimating the achievable resolution from the largest scattering angle in the holographic intensity yields $\sim$370 nm (HWHM), so that we do not reach the theoretical expectation given by the diffraction-limited CRL focus of 78 nm (FWHM). The detector provides a modulation transfer function of $\sim$2 px/half cycle and thus a resolution of $\sim$200 nm after consideration of the cone-beam magnification. To be able to create a diffraction limited source spot, the CRLs need to be illuminated with full lateral coherence over the geometric aperture of 300 µm. With the given design parameters of the European XFEL [Alt+06] this requirement should be fulfilled. The machine has been operated, however, for the first time at this high photon energies so that not all beam parameters might have been fully characterized. Various optics in the beampath between the instrument and the undulator [Mad+13] can introduce aberrations to the XFEL beam, which lead to a broadening of the focus and to a degradation of the resolution.

Nevertheless, we do not expect these aberrations to play a major role. We have to consider, however, that the SASE radiation consists of different longitudinal modes with different energies [SSY00]. CRLs are chromatic optics, so that different photon energies are focused with a different focal length. The focal length f is proportional to the inverse of the decrement δ of the refractive index $f \propto \delta^{-1}$ [Sch+01] and the decrement scales with $\delta \propto E_{\mathrm{ph}}^{-2}$ [AM11]. Hence, for small variations ΔE_{ph} in the photon energy we get a deviation Δf of the focal length of approximately $\Delta f/f \approx 2\Delta E_{\mathrm{ph}}/E_{\mathrm{ph}}$. With a spectral bandwidth of the SASE2 undulator of the European XFEL of approximately $\Delta E_{\mathrm{ph}}/E_{\mathrm{ph}} \approx 4\times10^{-3}$ at the photon energy used in the experiment and a focal length of 298 mm, this results in a deviation of the focal length of about $\Delta f \approx 2.4$ mm, which is almost 15-times the Rayleigh length of 160 µm. The beam diameter at $\Delta f/2 \approx 1.2$ mm defocus is already larger than $\sim$600 nm (FWHM), compared to 78 nm at the focal point. The superposition of the different longitudinal modes of the XFEL radiation thus results in a substantial broadening of the X-ray focus and consequently to a degradation of the holographic resolution.

The use of an X-ray waveguide could help to improve the resolution in X-ray holography with single XFEL pulses. The secondary source created by a channel waveguide ($\sim$50 nm diameter) placed in a larger prefocus ($\sim$1 µm focus size) is rather insensitive to the modal composition and aberrations in the prefocus, as long as the radiation is coupled into a single waveguide mode. This is the case as long as the angular spread of the incoming radiation lays well within the angular acceptance of the waveguide mode of about $\sim$0.1 mrad. This condition on the pointing stability of the X-ray beam is a prerequisite to perform experiments with such a long undulator-to-experiment distance. In contrast to CRLs, X-ray waveguides are an achromatic optic so that different longitudinal modes have the same source spot. With source spot sizes of down to sub-10 nm [Krü+12] X-ray waveguides could further improve the numerical aperture and thus the quality and resolution of nearfield holography with XFEL radiation.

Radially fitted phase: We have presented a new phase-retrieval algorithm, the *radially fitted phase* (RFP), for X-ray nearfield holography, that is tailored for radially symmetric holograms. The algorithm results in a higher resolution compared to the iterative AP algorithm (cf. Fig. 3.8). This might be a result of the increased signal-to-noise ratio (SNR) after azimuthal averaging of the hologram. The algorithm promises to be especially robust in low-photon-flux applications with low SNR. Furthermore, the formulation as a cost-function minimization provides flexibility to add regularisation or prior object knowledge. For known symmetry of the objects, e.g. spherical symmetry, the projection of the 3d phase distribution, i.e. of the 3d electron density, can be implemented within the algorithm, so that the algorithm retrieves the 3d phase instead of the projected phase. This has advantages for the application of object constraints, as a variety of constraints can be applied to the 3d phase only [RS16], such as the dual material constraint. It is important to notice however, that the algorithm converged without any regularisation in the case of the cavitation bubbles.

Automatized bulk analysis: The processing chain of the cavitation bubbles used in this thesis was fully automatized (cf. section 3.4). The flat-field correction was performed on the bulk dataset, followed by the calculation of the bubble center by an approach based on the Radon transform. This step already included a classification of the radial symmetry of the object, rejecting objects with multiple bubbles in the field of view. With the knowledge of the bubble center the azimuthal average of the intensity was calculated, followed by the RFP phase retrieval to obtain the projected phase shift of the object. A second classification step rejected floating gas bubbles by detecting the missing shockwave. After inversion of the projection the reconstructed 3d phase distribution gave access to the 3d mass density and the pressure of the shockwave, with the latter requiring the knowledge of the equation of state. All theses steps involved only an initial choice of parameters and were subsequently run automatically on the bulk data.

X-ray diffraction: We have measured spherical cavitation bubbles in bulk water with well-defined gas-to-shockwave and shockwave-to-equilibrium water interfaces in chapter 3. In chapter 4, we have measured perturbations after dielectric breakdown in a μ-fluidic water jet. Due to the boundary conditions imposed by the water jet, these perturbations did not form cavitation bubbles with well-defined interfaces, but rather chaotic perturbations with strong filamentation and without clearly defined bubble wall and shockwave edge. The same experimental approach for X-ray diffraction, as presented in chapter 4, can as well be used for measurements of cavitation bubbles in bulk water with well-defined interfaces, e.g. in a water-filled cuvette as in chapter 3. In such a configuration it would be possible to probe well-defined positions of a shockwave with a sub-100 nm X-ray focus in diffraction geometry to study the spatial distribution of the molecular structure inside the shockwave, inside the cavitation bubble, or at an interface. To this end, it would be beneficial to acquire the holographic and diffraction data simultaneously on a single-pulse basis. A possible approach would be to use optics with multiple foci to, at the same time, measure in focus for WAXS and in the diverging beam for holography, as it has been demonstrated in [Sch+15].

With the methods of chapter 3 and 4 there are now all tools at hand to study the interesting states of early cavitation bubble nucleation during and immediately after the plasma formation, as well as the state of maximum compression during the violent bubble collapse. The combination of holography and diffraction is especially powerful for these two bubble states, as it allows to observe both the changes in the molecular structure as well as the changes in mass density and pressure on the microscopic scale. Whereas it is sufficient for the observation of the early bubble nucleus to improve the temporal resolution by using a pump laser with femtosecond pulses, the observation of the collapse requires either an accurate prediction or an enforcement of the moment of the collapse. The acoustic stabilisation of a cavitation bubble, for example, can provide control over the point in time of the collapse [LK10].

In the XFEL experiments we have demonstrated the capabilities of X-ray sources with highest peak brilliance. Laboratory and table-top X-ray source are multiple orders of magnitude below the brilliance of synchrotrons and peak brilliance of XFELs. Nevertheless, due to the high availability and easy accessibility of table-top sources, X-ray experiments on the laboratory scale are a crucial part of structural analysis with X-rays. Even though the concept of X-ray generation in waveguides will not be able to close the gap to large-facility sources, we are confident that the improvements in brightness can substantially advance experiments on the laboratory scale under static and time-resolved conditions.

Appendix A

A.1 Selection of source code for chapter 3

Source code for *Python 3.7*.

A.1.1 Discrete Hankel transform

Numerical implementation of discrete Hankel transform following [BC15]:

```python
import numpy as np
import scipy.special

def hankelMatrix(N, n=0):
    '''
    returns a N x N matrix for discrete Hankel transfrom of n-th order.

    N: number of pixels
    n: order of Hankel transform

    The Hankel matrix is self-inverse! I.e. HH = Id
    For forward and backward Hankel transfrom different prefactors have to
      be considered!

    As in: N.Baddour and U.Chouinard. J. Opt. Soc. Am. A 32.4 (2015), pp
    -.611622. doi: 10.1364/JOSAA.32.000611.
    '''
    jn = np.array(scipy.special.jn_zeros(n, N + 1))

    k = np.expand_dims(np.arange(N), axis=0)
    m = np.expand_dims(np.arange(N), axis=1)

    jN = jn[-1]

    Y =  scipy.special.jn(n, jn[m] * jn[k] / jN) # matrix
    Y *= 2 / (jN * scipy.special.jn(n + 1, jn[k]) ** 2)  # prefactor

    return Y
```

```

def hankelFreq(N, n=0, kmax=0.5):
    '''
    Returns the Hankel space (frequency) sampling grid for the inverse discrete
    Hankel transfrom (of order n) of a signal with N pixels.
    kmax is the maximum sampling frequency in dimensionless units, i.e.
    minimal sampled realspace oscillation 2px -> max. sampled frequency 1/(2px)
    -> 0.5 dimensionless
    '''
    jn = np.array(scipy.special.jn_zeros(n, N + 1))
    return jn[:-1] * kmax / jn[N]

def hankelSamples(N, n=0, kmax=0.5):
    '''
    Returns the real space sampling grid for the forward discrete Hankel
    transfrom (of order n) of a signal with N pixels.
    kmax is the maximum sampling frequency in dimensionless units, i.e.
    minimal sampled realspace oscillation 2px -> max. sampled frequency 1/(2px)
    -> 0.5 dimensionless
    '''
    jn = np.array(scipy.special.jn_zeros(n, N))
    return jn / (kmax*2*np.pi)

def hankelTransform(f, n, hankelMat=None, kmax=0.5):
    '''
    Calculates the discrete Hankel transform of order "n" of the signal "f".
    "f" needs to be sampled on a Hankel grid (see function hankelSamples) and f has to
    decay to zero when reaching its boundary.
    If Hankel matrix "hankelMat" is given, the given order "n" has to match the order of
    the given Hankel matrix for correct scaling.
    For multiple calculations providing "hankelMat" results in speedup.

    Example:
    import numpy as np

    n = 512 # length of signal
    R = 100 # radius of sphere

    sphere = np.zeros((n,))
```

```
    r = hankelSamples(R) # samples on Hankel grid
    sphere[:R] = np.sqrt(R**2-r**2) # projected sphere at hankel grid positions

    F = hankelTransform(sphere, 0) # calculate Hankel transform.
    '''
    if hankelMat is None:
        hankelMat = hankelMatrix(len(f),n)

    k = kmax*2*np.pi
    N = hankelMat.shape[0]+1
    jN = scipy.special.jn_zeros(n, N)[-1]

    R = jN/k

    F = 2*np.pi*R**2/jN * np.matmul(hankelMat, f)

    return F

def inverseHankelTransform(F, n, hankelMat=None, kmax=0.5):
    '''
    Calculates the discrete inverse Hankel transform of order "n" of the signal "F".
    "F" needs to be sampled on a Hankel grid (see function hankelFreq) and "F" has to
    decay to zero when reaching its boundary.
    If Hankel matrix "hankelMat" is given, the given order "n" has to match the order of
    the given Hankel matrix for correct scaling.
    For multiple calculations providing "hankelMat" results in speedup.
    '''
    if hankelMat is None:
        hankelMat = hankelMatrix(len(F),n)

    k = kmax*2*np.pi
    N = hankelMat.shape[0]+1
    jN = scipy.special.jn_zeros(n, N)[-1]

    R = jN/k
    f = jN/(R**2*np.pi*2) * np.matmul(hankelMat, F)

    return f
```

A.1.2 Fresnel-type propagator for radially symmetric wavefields

Fresnel-type propagator for radially symmetric wavefields using the discrete Hankel transform (cf. section A.1.1):

```
import sys
import irpptb.transforms.hankel as hankel
import numpy as np

def propKernRadialSymmetric(F, n):
    '''
    Propagation kernel in Hankel space for radial symmetric
    propagation.
    F: Fresnel number
    n: number of pixels
    '''

    hFreq = hankel.hankelFreq(n)
    kern = np.exp(-1j*np.pi/F*(hFreq**2))
    return kern

def propMatrixRadialSymmetric(F,n):
    '''
    Propagation matrix for radial symmetric propagation.
    The signal for propagation needs to be sampled on Hankel grid.
    F: Fresnel number
    n: number of pixels
    '''
    propKern = propKernRadialSymmetric(F,n)
    hankelMat = hankel.hankelMatrix(n, n=0)

    tmp = propKern[:,None]*hankelMat
    propMatrix = np.matmul(hankelMat,tmp)
    return propMatrix

def propagateHankelFresnel(psi, F, npad=None, propagationMatrix=None):
    '''
    Propagates radial symmetric signal "psi" with Fresnel number "F".
    psi: complex wavefield sampled on Hankel grid. Oszillations of
    psi has to vanish when reaching its boundary (i.e. psi[-1] = 1)
    F: Fresnel number
    npad: number of pixels for padding
    propagationMatrix: precalculated propagation Matrix for radial
    symmetric Hankel-Fresnel propagation. if propagationMatrix is provided
     the given Fresnel number F is ignored
    '''
```

```
    dpsi = psi - 1

    if npad is not None:
        dpsi = np.pad(dpsi,(0,npad),mode='constant', constant_values=0)
        npad = -npad

    n = len(dpsi)

    if propagationMatrix is None:
        propagationMatrix = propMatrixRadialSymmetric(F,n)

    psiDet = np.matmul(propagationMatrix,dpsi)+1

    return psiDet[:npad]
```

A.1.3 Radially fitted phase

Phase retrieval for radially symmetric objects via *Radially fitted phase* (cf. section 3.4). Uses the Fresnel-type propagator of the section A.1.2:

```
import numpy as np
from scipy.optimize import minimize

def sqDifference(projectedPhase, Imeas, kappa, propHankelMat, alphaTV):
    '''
    Cost function of radially fitted phase which needs to be minimized.
    Calculates the L2 difference between the angular intensity of the
     propagated projected phase and the given measured intensity Imeas.
    projectedPhase: projected phase profile sampled on Hankel grid
    Imeas: measured intensity (angular average) sampled on Hankel grid
    kappa: beta/delta ratio of the material
    propHankelMat: Hankel-Fresnel-type propagation matrix
    alphaTV: regularisation parameter for Total Variation regularisation.
    '''
    n =projectedPhase.shape[0]
    npad = propHankelMat.shape[0]-n
    ptmp = np.pad(projectedPhase, (0,npad), mode='constant')

    # calculate exit wave in object plane:
    psiObj = np.exp((kappa+1j)*ptmp) - 1

    # propagate to detector and calculate intensity
    psiDet = np.matmul(propHankelMat, psiObj) + 1
    Idet = np.abs(psiDet)**2
```

```python

    # add TV norm if alphaTV>0
    TV = 0
    if alphaTV!=0:
        TV = (np.abs(projectedPhase[:-1]-projectedPhase[1:])).sum()

    # calculate L2 difference between propagated intensity and measured intensity
    diff = ((Imeas-Idet)**2).sum()
    return diff + alphaTV*TV

def radiallyFittedPhase(Ihankel, propHankelMat, kappa, Rguess, TValpha, initialGuess = None, tolerance=1e-15):
    '''
    Phase retrieval radially fitted phase:
    Ihankel: measured intensity (angular average) sampled on Hankel grid
    propHankelMat: Hankel-Fresnel-type propagation matrix
    kappa: beta/delta ratio of the material
    Rguess: guess for radius of shockwave wall (not used if initialGuess is given)
    TValpha: regularisation parameter for Total Variation regularisation.
    initialGuess: initial guess of projected phase profile
    tolerance: target tolerance of optimizer
    returns: optimized projected phase
    '''
    # if no initial guess is given, init with exemplary cavitation bubble
    if initialGuess = None:
        initialGuess = np.zeros(Rguess)
        ph_sw = -0.0015
        ph_bubble = 0.01-ph_sw
        R = int(0.45*Rguess)
        R2 = R*2
        initialGuess[:R]  = 2*np.sqrt(R**2-np.arange(R)**2)*ph_bubble
        initialGuess[:R2] += 2*np.sqrt(R2**2-np.arange(R2)**2)*ph_sw

    # minimize cost function sqDifference
    rekt =  minimize(sqDifference, initialGuess, args=(Ihankel, kappa, propHankelMat, TValpha), tol=tolerance, options={'maxiter': 3000}, method='BFGS')

    # return result
    return rekt
```

A.1.4 Radon-transform-based center finder

Calculates the center of an object with radial symmetry in an image and gives an estimate of how well radial symmetry is fulfilled. *calcCenterShift* uses an approach based on the Radon transform to calculate the center. *iterativeRadonShift* uses an iterative approach. This approach iterates between the center calculation by *calcCenterShit* and a registration of the shift between image and the reprojection of the aligned sinogram.

```
import numpy as np
from numpy.fft import fftfreq

import sys, os
sys.path.append(os.getenv('HOME')+'/lib/ptb')

from pyfftw.interfaces.numpy_fft import fft, ifft, fftshift, ifftshift,
    fft2, ifft2

from irpptb.imageProcessing.alignment import dftregistration
''' dftregistration:
dftregistration registers subpixel shifts between images. Python
implementation adapted from Manuel Guizar-Sicairos, Samuel T. Thurman, and
     James R. Fienup,
Efficient subpixel image registration algorithms, Opt. Lett. 33, 156-158
    (2008).
'''

from irpptb.imageProcessing.alignment import circshift
''' circshift:
shifts an n-dimensional array with sub-pixel accuracy along a given vector
array: n-dimensional numpy array
shift: vector with length n, the i-th axis of the input array is shifted
    by the i-th element of the vector shift, if shift is an integer
    number no interpolation is done.
'''
from scipy.optimize import curve_fit

from skimage.transform import radon
from scipy.interpolate import interp1d

def calcCenterShift(img, nAngles=101, upsfac=5):
    '''
    calculate shift of image img to center the bubble in the image.
    This function uses a Radon transform base approach and registers
    subpixel
    shifts between subsequent angles in the sinogram.
```

```
    The determination of the shifts in the sinogram is used to calculate the
    center of the bubble.
    img: image containing the bubble
    nAngles: number of angles for Radon transform
    upsfac: upsampling factor for dftregistration (subpixel accuracy)
    '''
    def cosfit(angle, scale, phi_offset, y_offset):
        return scale*np.cos((angle+phi_offset)/180*np.pi)+y_offset
    angles = np.linspace(0,360,nAngles)

    # perform radon transform
    rt = radon(img,theta=angles, circle=True)
    ftRT = np.expand_dims(fft(fftshift(rt,axes=0), axis=0),axis=0)

    shift = np.zeros((nAngles,))

    # register shifts between subsequent angles in the sinogram
    for i in range(nAngles):
        i2 = np.mod(i+1, nAngles) # periodic boundary
        shift[i] = dftregistration(ftRT[:,:,i], ftRT[:,:,i2], usfac=upsfac)[1]

    shift_abs = np.array([shift[:i].sum() for i in range(1,nAngles)])

    anglesFit = angles[:-2]+angles[1]/2

    miny = shift_abs.min()
    maxy = shift_abs.max()
    indAtMax = np.argmax(shift_abs[:-1])

    # determine initial values for cosine fit to the shifts
    A0 = (maxy-miny)/2;
    y0 = (maxy+miny)/2;
    phi0 = np.mod(anglesFit[indAtMax]+180, 360);

    # fit cosine function to the shifts
    try:
        p, pcov = curve_fit(cosfit, anglesFit, shift_abs[:-1], p0=[A0,phi0,y0], bounds=((0, 0, -np.inf),(np.inf,360,np.inf)))
    except:
        p = np.zeros((3,))

    # calcualate the L2 error
    sumSqError = ((shift_abs[:-1]-cosfit(anglesFit,*p))**2).sum()
```

```python

    # prepare to return result
    fitres = p
    shiftx =  fitres[0]*np.cos(fitres[1]/180*np.pi)
    shifty =  fitres[0]*np.sin(fitres[1]/180*np.pi)

    center_shift = np.array((shifty, shiftx))

    sumShift= shift.sum()

    result = {}

    result['sumShift'] = sumShift
    result['sumSqError'] = sumSqError
    result['centerShift'] = center_shift
    result['radonTransform']  = rt
    result['shift_abs'] = shift_abs
    result['fitParams'] = p

    return result

def iradonFourierInversion(sinoSum, r_fftshifted=None):
    '''
    efficient inverse Radon transform based on the Fourier inversion for
    radial symmetric objects.
    sinoSum: sinogram for one angle
    r_fftshifted: precalculated 2d array of radius coordinates

    '''
    n = sinoSum.shape[0]
    nh = n/2

    a = fftshift(np.linspace(-nh,nh,n))

    # calculate 2d map of r = sqrt(X^2+Y^2)
    if r_fftshifted is None:
        x = np.expand_dims(a,axis=0)
        y = np.expand_dims(a,axis=1)
        r_fftshifted = np.sqrt(x**2+y**2)
        r_fftshifted[r_fftshifted>nh] = nh

    # interpolate 1d sinogram into 2d
    ftSino = fft(fftshift(sinoSum))
    ifun = interp1d(a,ftSino)

```

```
    # Fourier inversion of radon transform
    FimIradon = ifun(r_fftshifted)
    imIradon = np.real(ifftshift(ifft2(FimIradon)))
    return imIradon

#### iterative Radon Center Shift:
# img has to decay to 0
def iterativeRadonShift(I0, nAngles=101, nIterations=3):
    '''
    find center of bubble in an interative approach.
    This function iterates multiple times over calcCenterShift and a
    subsequent alignment of the image to the reprojected Radon image.
    '''
    def cosfit(angle, scale, phi_offset, y_offset):
        return scale*np.cos((angle+phi_offset)/180*np.pi)+y_offset
    n= I0.shape[0]

    if np.mod(n,2)==1:
        print('dftregistration only accepts input with even dimensions.
    skipping')
        return -1

    # allocate arrays
    cenShiftRadon = np.zeros((nIterations,2))
    cenShiftReproj = np.zeros((nIterations,2))
    In_preReproj = np.zeros((nIterations,n,n))
    In = np.zeros((nIterations,n,n))

    angles = np.linspace(0,360,nAngles)


    totalShift = np.zeros((2,))

    # iterate
    for i in range(nIterations):

        # calculate shift with radon transform based approach
        resRadon = calcCenterShift(I0,nAngles,upsfac=5)

        rt = resRadon['radonTransform']
        cenShiftRadon[i,:] = resRadon['centerShift']
        shift_abs = resRadon['shift_abs']

        # shift each angle of the sinogram by the calculated shift
```

```
        rt_shifted = np.array([circshift(rt[:,j+1], [shift_abs[j]+cenShiftRadon[i,1]]) for j in range(shift_abs.shape[0]-1)])
        # calculate the mean of the shifted sinogram
        rt_shiftSum = np.flipud(np.rot90(rt_shifted)).mean(1)

        # shift the image
        IShifted = circshift(I0, cenShiftRadon[i,:])

        totalShift += cenShiftRadon[i,:]

        # reproject the mean sinogram
        imIradon = iradonFourierInversion(rt_shiftSum)

        # calculate the the shift between image and reprojected mean sinogram
        ft1 = fft2(fftshift(imIradon))
        ft2 = fft2(fftshift(IShifted))
        cenShiftReproj[i,:] = dftregistration(ft1, ft2, usfac=5)
        totalShift += cenShiftReproj[i,:]

        In_preReproj[i,:,:] = IShifted

        In[i,:,:] = circshift(IShifted, cenShiftReproj[i,:])

        I0 = In[i,:,:]

    # prepare result
    rt_shifted = radon(I0, angles[:-1],)
    rt_shiftSum = rt_shifted.mean(1)

    imIradon = iradonFourierInversion(rt_shiftSum)

    diffL2 = ((I0-imIradon)**2).sum()
    diffL1 = (np.abs(I0-imIradon)).sum()

    result = {}

    result['sumShift'] = resRadon['sumShift'].copy()
    result['sumSqError'] = resRadon['sumSqError'].copy()
    result['centerShift'] = totalShift
    result['centerShift_nonIterative'] = cenShiftRadon[0,:]
    result['shiftHistory_reproj'] = cenShiftReproj
    result['shiftHistory_radon'] = cenShiftRadon
    result['radonTransform']  = rt_shifted
    result['shift_abs'] = shift_abs.copy()
```

```

    result['diffCenterSymmL2'] = diffL2
    result['diffCenterSymmL1'] = diffL1

    return result
```

Bibliography

[Ada03] B. Adams. *Nonlinear Optics, Quantum Optics, and Ultrafast Phenomena with X-Rays: Physics With X-Ray Free-Electron Lasers*. Springer Science & Business Media, 2003. ISBN: 978-1-4020-7475-2.

[Ada+13] B. W. Adams, C. Buth, S. M. Cavaletto, J. Evers, Z. Harman, C. H. Keitel, A. Pálffy, A. Picón, R. Röhlsberger, Y. Rostovtsev, and K. Tamasaku. "X-ray quantum optics". In: *Journal of Modern Optics* 60.1 (2013), pp. 2–21. DOI: `10.1080/09500340.2012.752113`.

[All+15] A. Allahgholi et al. "AGIPD, a high dynamic range fast detector for the European XFEL". In: *J. Inst.* 10.01 (2015), pp. C01023–C01023. DOI: `10.1088/1748-0221/10/01/C01023`.

[AM11] J. Als-Nielsen and D. McMorrow. *Elements of modern X-ray physics*. John Wiley & Sons, 2011.

[Alt+06] M. Altarelli et al. *XFEL: The European X-Ray Free-Electron laser: Technical Design Report*. Tech. rep. DESY 2006-097. DESY, 2006.

[AJ10] J.-M. André and P. Jonnard. "X-ray spontaneous emission control by 1-dimensional photonic bandgap structure". In: *Eur. Phys. J. D* 57.3 (2010), pp. 411–418.

[Ant+19] L. Antonelli, F. Barbato, D. Mancelli, J. Trela, G. Zeraouli, G. Boutoux, P. Neumayer, S. Atzeni, A. Schiavi, L. Volpe, V. Bagnoud, C. Brabetz, B. Zielbauer, P. Bradford, N. Woolsey, B. Borm, and D. Batani. "X-ray phase-contrast imaging for laser-induced shock waves". In: *EPL (Europhysics Letters)* 125.3 (2019), p. 35002. DOI: `10.1209/0295-5075/125/35002`.

[Bad09] N. Baddour. "Operational and convolution properties of two-dimensional Fourier transforms in polar coordinates". In: *J. Opt. Soc. Am. A* 26.8 (2009), pp. 1767–1777.

[BC15] N. Baddour and U. Chouinard. "Theory and operational rules for the discrete Hankel transform". In: *J. Opt. Soc. Am. A* 32.4 (2015), pp. 611–622. DOI: `10.1364/JOSAA.32.000611`.

[BS19] S. Bajt and C. G. Schroer. “Sub-micrometer Focusing and High-Resolution Imaging with Refractive Lenses and Multilayer Laue Optics”. In: *Synchrotron Light Sources and Free-Electron Lasers: Accelerator Physics, Instrumentation and Science Applications*. Ed. by E. Jaeschke, S. Khan, J. R. Schneider, and J. B. Hastings. Cham: Springer International Publishing, 2019, pp. 1–28. ISBN: 978-3-319-04507-8. DOI: `10.1007/978-3-319-04507-8_62-1`.

[Bal10] K. Balewski. “Commissioning of Petra III”. In: *Proceedings of 1st International Particle Accelerator Conference: IPAC*. Vol. 10. 2010.

[Bar+15a] M. Bartels, M. Krenkel, P. Cloetens, W. Möbius, and T. Salditt. “Myelinated mouse nerves studied by X-ray phase contrast zoom tomography”. In: *Journal of Structural Biology* 192.3 (2015), pp. 561–568. DOI: `10.1016/j.jsb.2015.11.001`.

[Bar+15b] M. Bartels, M. Krenkel, J. Haber, R. N. Wilke, and T. Salditt. “X-Ray Holographic Imaging of Hydrated Biological Cells in Solution”. In: *Phys. Rev. Lett.* 114 (4 2015), p. 048103. DOI: `10.1103/PhysRevLett.114.048103`.

[Bar+13] M. Bartels, V. H. Hernandez, M. Krenkel, T. Moser, and T. Salditt. “Phase contrast tomography of the mouse cochlea at microfocus x-ray sources”. In: *Applied Physics Letters* 103.8 (2013), p. 083703. DOI: `10.1063/1.4818737`.

[Bar+02] R. A. Bartels, A. Paul, H. Green, H. C. Kapteyn, M. M. Murnane, S. Backus, I. P. Christov, Y. Liu, D. Attwood, and C. Jacobsen. “Generation of Spatially Coherent Light at Extreme Ultraviolet Wavelengths”. In: *Science* 297.5580 (2002), pp. 376–378. DOI: `10.1126/science.1071718`.

[Bar+08] A. Barty, S. Boutet, M. J. Bogan, S. Hau-Riege, S. Marchesini, K. Sokolowski-Tinten, N. Stojanovic, R. Tobey, H. Ehrke, A. Cavalleri, S. Düsterer, M. Frank, S. Bajt, B. W. Woods, M. M. Seibert, J. Hajdu, R. Treusch, and H. N. Chapman. “Ultrafast single-shot diffraction imaging of nanoscale dynamics”. In: *Nature Photonics* 2.7 (2008), pp. 415–419. DOI: `10.1038/nphoton.2008.128`.

[Bee+09] A. Beerlink, M. Mell, M. Tolkiehn, and T. Salditt. “Hard x-ray phase contrast imaging of black lipid membranes”. In: *Applied Physics Letters* 95.20 (2009), p. 203703. DOI: `10.1063/1.3263946`.

[Beh16] R. Behling. *Modern diagnostic X-ray sources*. CRC Press, 2016.

[BFH18] S. Boutet, P. Fromme, and M. S. Hunter. *X-ray Free Electron Lasers: A Revolution in Structural Biology*. Springer, 2018. ISBN: 978-3-030-00551-1.

[BB00] R. N. Bracewell and R. Bracewell. *The Fourier Transform and Its Applications*. 3rd. Electrical engineering series. McGraw Hill, 2000. ISBN: 978-0-07-303938-1.

[Bre14] C. E. Brennen. *Cavitation and Bubble Dynamics*. New York: Cambridge University Press, 2014. ISBN: 978-1-107-64476-2.

[Bre15] C. E. Brennen. "Cavitation in medicine". In: *Interface Focus* 5.5 (2015), p. 20150022. DOI: `10.1098/rsfs.2015.0022`.

[BHL02] M. P. Brenner, S. Hilgenfeldt, and D. Lohse. "Single-bubble sonoluminescence". In: *Rev. Mod. Phys.* 74 (2 2002), pp. 425–484.

[Bro02] A. V. Bronnikov. "Theory of quantitative phase-contrast computed tomography". In: *JOSA A* 19.3 (2002), pp. 472–480. DOI: `10.1364/JOSAA.19.000472`.

[Bro95] S. D. Brorson. *Electromagnetic field mode density calculated via mode counting*. Boca Raton: CRC Press, 1995, pp. 151–187.

[Bro+04] P. J. Brown, A. G. Fox, E. N. Maslen, M. A. O'Keefe, and B. T. M. Willis. "Intensity of diffracted intensities". In: *International Tables for Crystallography Volume C: Mathematical, physical and chemical tables*. Ed. by E. Prince. International Tables for Crystallography. Dordrecht: Springer Netherlands, 2004, pp. 554–595. ISBN: 978-1-4020-5408-2. DOI: `10.1107/97809553602060000600`.

[BOM35] E. F. Burton, W. F. Oliver, and J. C. McLennan. "The crystal structure of ice at low temperatures". In: *Proceedings of the Royal Society of London. Series A - Mathematical and Physical Sciences* 153.878 (1935), pp. 166–172. DOI: `10.1098/rspa.1935.0229`.

[Bus+18] M. Busse, M. Müller, M. A. Kimm, S. Ferstl, S. Allner, K. Achterhold, J. Herzen, and F. Pfeiffer. "Three-dimensional virtual histology enabled through cytoplasm-specific X-ray stain for microscopic and nanoscopic computed tomography". In: *Proceedings of the National Academy of Sciences* 115.10 (2018), pp. 2293–2298. DOI: `10.1073/pnas.1720862115`.

[BK04] K.-T. Byun and H.-Y. Kwak. "A Model of Laser-Induced Cavitation". In: *Jpn. J. Appl. Phys.* 43.2R (2004), p. 621. DOI: `10.1143/JJAP.43.621`.

[CM17] C. Cairos and R. Mettin. “Simultaneous High-Speed Recording of Sonoluminescence and Bubble Dynamics in Multibubble Fields”. In: *Phys. Rev. Lett.* 118 (6 2017), p. 064301. DOI: `10.1103/PhysRevLett.118.064301`.

[Car+14] S. Cartier, A. Bergamaschi, R. Dinapoli, D. Greiffenberg, I. Johnson, J. H. Jungmann, D. Mezza, A. Mozzanica, B. Schmitt, X. Shi, M. Stampanoni, J. Sun, and G. Tinti. “Micron resolution of MÖNCH and GOTTHARD, small pitch charge integrating detectors with single photon sensitivity”. In: *J. Instrum.* 9.05 (2014), pp. C05027–C05027.

[Ced+17] A. Cedola, A. Bravin, I. Bukreeva, M. Fratini, A. Pacureanu, A. Mittone, L. Massimi, P. Cloetens, P. Coan, G. Campi, R. Spanò, F. Brun, V. Grigoryev, V. Petrosino, C. Venturi, M. Mastrogiacomo, N. Kerlero de Rosbo, and A. Uccelli. “X-Ray Phase Contrast Tomography Reveals Early Vascular Alterations and Neuronal Loss in a Multiple Sclerosis Model”. In: *Scientific Reports* 7.1 (2017), p. 5890. DOI: `10.1038/s41598-017-06251-7`.

[Cha+05] S.-L. Chang, Y. P. Stetsko, M.-T. Tang, Y.-R. Lee, W.-H. Sun, M. Yabashi, and T. Ishikawa. “X-Ray Resonance in Crystal Cavities: Realization of Fabry-Perot Resonator for Hard X Rays”. In: *Phys. Rev. Lett.* 94 (17 2005), p. 174801. DOI: `10.1103/PhysRevLett.94.174801`.

[Cha+06] H. N. Chapman et al. “Femtosecond diffractive imaging with a soft-X-ray free-electron laser”. In: *Nature Physics* 2.12 (2006), pp. 839–843. DOI: `10.1038/nphys461`.

[CGV97] E. J. Chapyak, R. P. Godwin, and A. Vogel. “Comparison of numerical simulations and laboratory studies of shock waves and cavitation bubble growth produced by optical breakdown in water”. In: *Laser-Tissue Interaction VIII*. Vol. 2975. International Society for Optics and Photonics, 1997, pp. 335–342. DOI: `10.1117/12.275497`.

[CHS15] H.-Y. Chen, S. Hoffmann, and T. Salditt. “X-ray beam compression by tapered waveguides”. In: *Appl. Phys. Lett.* 106.19 (2015), p. 194105. DOI: `10.1063/1.4921095`.

[Clo+99] P. Cloetens, W. Ludwig, J. Baruchel, D. Van Dyck, J. Van Landuyt, J. P. Guigay, and M. Schlenker. “Holotomography: Quantitative phase tomography with micrometer resolution using hard synchrotron radiation x rays”. In: *Appl. Phys. Lett.* 75.19 (1999), pp. 2912–2914. DOI: `10.1063/1.125225`.

[Clo+96] P. Cloetens, R. Barrett, J. Baruchel, J.-P. Guigay, and M. Schlenker. “Phase objects in synchrotron radiation hard x-ray imaging”. In: *Journal of Physics D: Applied Physics* 29.1 (1996), pp. 133–146. DOI: `10.1088/0022-3727/29/1/023`.

[Col48] R. H. Cole. *Underwater Explosions*. Princeton University Press, 1948. ISBN: 978-0-691-06922-7.

[DGK96] B. J. Dalton, E. S. Guerra, and P. L. Knight. “Field quantization in dielectric media and the generalized multipolar Hamiltonian”. In: *Phys. Rev. A* 54 (3 1996), pp. 2292–2313.

[Deb03] P. G. Debenedetti. “Supercooled and glassy water”. In: *J. Phys.: Condens. Matter* 15.45 (2003), R1669–R1726. DOI: `10.1088/0953-8984/15/45/R01`.

[Dep+15] A. Depresseux et al. “Table-top femtosecond soft X-ray laser by collisional ionization gating”. In: *Nature Photonics* 9.12 (2015), pp. 817–821. DOI: `10.1038/nphoton.2015.225`.

[Dra+14] A. Dragone, P. Caragiulo, B. Markovic, R. Herbst, B. Reese, S. C. Herrmann, P. A. Hart, J. Segal, G. A. Carini, C. J. Kenney, and G. Haller. “ePix: a class of architectures for second generation LCLS cameras”. In: *J. Phys.: Conf. Ser.* 493 (2014), p. 012012. DOI: `10.1088/1742-6596/493/1/012012`.

[DKS68] K. H. Drexhage, H. Kuhn, and F. P. Schäfer. “Variation of the Fluorescence Decay Time of a Molecule in Front of a Mirror”. In: *Ber. Bunsenges. Phys. Chem.* 72.2 (1968), pp. 329–329.

[DKK95] Y. I. Dudchik, F. F. Komarov, and Y. A. Kostantinov. “New application of x-ray waveguides in microfocus x-ray tubes”. In: *X-Ray and Ultraviolet Sensors and Applications*. Vol. 2519. International Society for Optics and Photonics. SPIE, 1995, pp. 50–59.

[Dys90] N. A. Dyson. *X-rays in Atomic and Nuclear Physics*. 2nd ed. Cambridge: Cambridge University Press, 1990. ISBN: 978-0-521-01722-0.

[Egg+16] E. Eggl, M. Dierolf, K. Achterhold, C. Jud, B. Günther, E. Braig, B. Gleich, and F. Pfeiffer. “The Munich Compact Light Source: initial performance measures”. In: *Journal of Synchrotron Radiation* 23.5 (2016), pp. 1137–1142. DOI: `10.1107/S160057751600967X`.

[Fel+15] C. Fella, A. Balles, S. Zabler, R. Hanke, R. Tjeung, S. Nguyen, and D. Pelliccia. “Laboratory x-ray microscopy on high brilliance sources equipped with waveguides”. In: *Journal of Applied Physics* 118.3 (2015), p. 034904. DOI: `10.1063/1.4927038`.

[Fen+93] Y. P. Feng, S. K. Sinha, H. W. Deckman, J. B. Hastings, and D. P. Siddons. “X-ray flux enhancement in thin-film waveguides using resonant beam couplers”. In: *Phys. Rev. Lett.* 71.4 (1993), pp. 537–540.

[FS05] D. J. Flannigan and K. S. Suslick. “Plasma formation and temperature measurement during single-bubble cavitation”. In: *Nature* 434 (2005), pp. 52–55. DOI: `10.1038/nature03361`.

[FKL13] W. Friedrich, P. Knipping, and M. Laue. “Interferenzerscheinungen bei Röntgenstrahlen”. In: *Annalen der Physik* 346.10 (1913), pp. 971–988. DOI: `https://doi.org/10.1002/andp.19133461004`.

[Fuc+15] M. Fuchs et al. “Anomalous nonlinear X-ray Compton scattering”. In: *Nature Physics* 11.11 (2015), pp. 964–970. DOI: `10.1038/nphys3452`.

[Gab48] D. Gabor. “A new microscopic principle”. In: *Nature* 161 (1948), pp. 777–778.

[GB49] D. Gabor and W. L. Bragg. “Microscopy by reconstructed wave-fronts”. In: *Proceedings of the Royal Society of London. Series A. Mathematical and Physical Sciences* 197.1051 (1949), pp. 454–487. DOI: `10.1098/rspa.1949.0075`.

[Gib05] P. Gibbon. *Short Pulse Laser Interactions With Matter: An Introduction*. World Scientific, 2005. ISBN: 978-1-911298-84-7.

[Gie+11] K. Giewekemeyer, S. P. Krüger, S. Kalbfleisch, M. Bartels, C. Beta, and T. Salditt. “X-ray propagation microscopy of biological cells using waveguides as a quasipoint source”. In: *Physical Review A* 83.2 (2011), p. 023804. DOI: `10.1103/PhysRevA.83.023804`.

[Gil52] F. R. Gilmore. “The Growth or Collapse of a Spherical Bubble in a Viscous Compressible Liquid”. In: *Hydrodanamics Laboratory California Institute of Technology, Report No. 26-4* (1952).

[God+09] J. P. Goddet, S. Sebban, J. Gautier, P. Zeitoun, C. Valentin, F. Tissandier, T. Marchenko, G. Lambert, M. Ribières, D. Douillet, T. Lefrou, G. Iaquaniello, F. Burgy, G. Maynard, B. Cros, B. Robillard, T. Mocek, J. Nejdl, M. Kozlova, and K. Jakubczak. "Aberration-free laser beam in the soft x-ray range". In: *Optics Letters* 34.16 (2009), pp. 2438–2440. DOI: `10.1364/OL.34.002438`.

[GWA86] D. E. Grider, A. Wright, and P. K. Ausburn. "Electron beam melting in microfocus X-ray tubes". In: *Journal of Physics D: Applied Physics* 19.12 (1986), pp. 2281–2292. DOI: `10.1088/0022-3727/19/12/008`.

[Gur03] T. E. Gureyev. "Composite techniques for phase retrieval in the Fresnel region". In: *Optics Communications* 220.1 (2003), pp. 49–58. DOI: `10.1016/S0030-4018(03)01353-1`.

[Hab+19] J. Haber, J. Gollwitzer, S. Francoual, M. Tolkiehn, J. Strempfer, and R. Röhlsberger. "Spectral Control of an X-Ray L-Edge Transition via a Thin-Film Cavity". In: *Phys. Rev. Lett.* 122 (12 2019), p. 123608.

[Hab+16] J. Haber, K. S. Schulze, K. Schlage, R. Loetzsch, L. Bocklage, T. Gurieva, H. Bernhardt, H.-C. Wille, R. Rüffer, I. Uschmann, G. G. Paulus, and R. Röhlsberger. "Collective strong coupling of X-rays and nuclei in a nuclear optical lattice". In: *Nat. Photonics* 10 (2016), pp. 445–449.

[Hab+20] J. Haber, A. Kaldun, S. W. Teitelbaum, A. Q. R. Baron, P. H. Bucksbaum, M. Fuchs, J. B. Hastings, I. Inoue, Y. Inubushi, D. Krebs, T. Osaka, R. Santra, S. Shwartz, K. Tamasaku, and D. A. Reis. "Nonlinear resonant X-ray Raman scattering". In: *arXiv:2006.14724* (2020).

[Hab+17] J. Haber, X. Kong, C. Strohm, S. Willing, J. Gollwitzer, L. Bocklage, R. Rüffer, A. Pálffy, and R. Röhlsberger. "Rabi oscillations of X-ray radiation between two nuclear ensembles". In: *Nature Photonics* 11.11 (2017), pp. 720–725. DOI: `10.1038/s41566-017-0013-3`.

[HTS18] J. Hagemann, M. Töpperwien, and T. Salditt. "Phase retrieval for near-field X-ray imaging beyond linearisation or compact support". In: *Appl. Phys. Lett.* 113.4 (2018). DOI: `10.1063/1.5029927`.

[Hag+21] J. Hagemann, M. Vassholz, H. Hoeppe, M. Osterhoff, J. M. Rosselló, R. Mettin, F. Seiboth, A. Schropp, J. Möller, J. Hallmann, C. Kim, M. Scholz, U. Boesenberg, R. Schaffer, A. Zozulya, W. Lu, R. Shayduk, A. Madsen, C. G. Schroer, and T. Salditt. "Single-pulse phase-contrast imaging at free-electron lasers in the hard X-ray regime". In: *J. Synchrotron Rad.* 28.1 (2021). DOI: `10.1107/S160057752001557X`.

[HS18] J. Hagemann and T. Salditt. "Coherence-resolution relationship in holographic and coherent diffractive imaging". In: *Optics Express* 26.1 (2018), pp. 242–253. DOI: `10.1364/OE.26.000242`.

[HS19] J. Hagemann and T. Salditt. *Cavitation Dynamics Studied by Time-Resolved High-Resolution X-Ray Holography*. 2019. DOI: `10.22003/XFEL.EU-DATA-002207-00`.

[HW13] H. Haken and H. C. Wolf. *Atom- und Quantenphysik: Einführung in die experimentellen und theoretischen Grundlagen*. Springer-Verlag, 2013.

[Hal+20] A. Halavanau, A. Benediktovitch, A. A. Lutman, D. DePonte, D. Cocco, N. Rohringer, U. Bergmann, and C. Pellegrini. "Population inversion X-ray laser oscillator". In: *Proc. Natl. Acad. Sci. U.S.A.* 117.27 (2020), pp. 15511–15516. DOI: `10.1073/pnas.2005360117`.

[Hay+16] K. Hayasaka, Y. Tagawa, T. Liu, and M. Kameda. "Optical-flow-based background-oriented schlieren technique for measuring a laser-induced underwater shock wave". In: *Exp. Fluids* 57.12 (2016), p. 179. DOI: `10.1007/s00348-016-2271-0`.

[Hay67] A. T. J. Hayward. "Compressibility equations for liquids: a comparative study". In: *Br. J. Appl. Phys.* 18.7 (1967), pp. 965–977. DOI: `10.1088/0508-3443/18/7/312`.

[Hee+15a] K. P. Heeg, C. Ott, D. Schumacher, H.-C. Wille, R. Röhlsberger, T. Pfeifer, and J. Evers. "Interferometric phase detection at x-ray energies via Fano resonance control". In: *Phys. Rev. Lett.* 114 (20 2015), p. 207401. DOI: `10.1103/PhysRevLett.114.207401`.

[Hee+15b] K. P. Heeg, J. Haber, D. Schumacher, L. Bocklage, H.-C. Wille, K. S. Schulze, R. Loetzsch, I. Uschmann, G. G. Paulus, R. Rüffer, R. Röhlsberger, and J. Evers. "Tunable Subluminal Propagation of Narrow-band X-Ray Pulses". In: *Physical Review Letters* 114.20 (2015), p. 203601. DOI: `10.1103/PhysRevLett.114.203601`.

[HOH03] O. Hemberg, M. Otendal, and H. M. Hertz. "Liquid-metal-jet anode electron-impact x-ray source". In: *Appl. Phys. Lett.* 83.7 (2003), pp. 1483–1485. DOI: `10.1063/1.1602157`.

[HS16] S. Hoffmann-Urlaub and T. Salditt. “Miniaturized beamsplitters realized by X-ray waveguides”. In: *Acta Cryst. A* 72.5 (2016), pp. 515–522.

[Hof+16] S. Hoffmann-Urlaub, P. Höhne, M. Kanbach, and T. Salditt. “Advances in fabrication of X-ray waveguides”. In: *Microelectronic Engineering* 164 (2016), pp. 135–138. DOI: `10.1016/j.mee.2016.07.010`.

[Hol10] J. Holzfuss. “Acoustic energy radiated by nonlinear spherical oscillations of strongly driven bubbles”. In: *Proceedings of the Royal Society A: Mathematical, Physical and Engineering Sciences* 466.2118 (2010), pp. 1829–1847.

[Hor+19] B. Hornberger, J. Kasahara, M. Gifford, R. Ruth, and R. Loewen. “A compact light source providing high-flux, quasi-monochromatic, tunable X-rays in the laboratory”. In: *Advances in Laboratory-based X-Ray Sources, Optics, and Applications VII*. Vol. 11110. International Society for Optics and Photonics, 2019, p. 1111003. DOI: `10.1117/12.2527356`.

[Ibr+15] S. Ibrahimkutty, P. Wagener, T. d. S. Rolo, D. Karpov, A. Menzel, T. Baumbach, S. Barcikowski, and A. Plech. “A hierarchical view on material formation during pulsed-laser synthesis of nanoparticles in liquid”. In: *Sci. Rep.* 5.1 (2015), pp. 1–11. DOI: `10.1038/srep16313`.

[Ino+16] I. Inoue, Y. Inubushi, T. Sato, K. Tono, T. Katayama, T. Kameshima, K. Ogawa, T. Togashi, S. Owada, Y. Amemiya, T. Tanaka, T. Hara, and M. Yabashi. “Observation of femtosecond X-ray interactions with matter using an X-ray–X-ray pump–probe scheme”. In: *Proceedings of the National Academy of Sciences* 113.6 (2016), pp. 1492–1497. DOI: `10.1073/pnas.1516426113`.

[Jac+90] C. Jacobsen, M. Howells, J. Kirz, and S. Rothman. “X-ray holographic microscopy using photoresists”. In: *JOSA A* 7.10 (1990), pp. 1847–1861. DOI: `10.1364/JOSAA.7.001847`.

[JD04] W. Jark and S. Di Fonzo. “Prediction of the transmission through thin-film waveguides for X-ray microscopy”. In: *J. Synchrotron Radiat.* 11.5 (2004), pp. 386–392.

[Jar+05] A. Jarre, C. Fuhse, C. Ollinger, J. Seeger, R. Tucoulou, and T. Salditt. “Two-Dimensional Hard X-Ray Beam Compression by Combined Focusing and Waveguide Optics”. In: *Phys. Rev. Lett.* 94.7 (2005), p. 074801.

[Jia15] Z. Jiang. “GIXSGUI: a MATLAB toolbox for grazing-incidence X-ray scattering data visualization and reduction, and indexing of buried three-dimensional periodic nanostructured films”. In: *J Appl Crystallogr* 48.3 (2015), pp. 917–926. DOI: `10.1107/S1600576715004434`.

[Jon+02] P. Jonnard, J.-M. André, C. Bonnelle, F. Bridou, and B. Pardo. “Modulation of x-ray line intensity emitted by a periodic structure under electron excitation”. In: *Appl. Phys. Lett.* 81.8 (2002), pp. 1524–1526.

[Jun+09] Y. C. Jun, R. M. Briggs, H. A. Atwater, and M. L. Brongersma. “Broadband enhancement of light emission in silicon slot waveguides”. In: *Opt. Express* 17.9 (2009), pp. 7479–7490.

[KS01] A. C. Kak and M. Slaney. *Principles of Computerized Tomographic Imaging*. SIAM, 2001. ISBN: 978-0-89871-494-4.

[KLS95] A. E. Kaplan, C. T. Law, and P. L. Shkolnikov. “X-ray narrow-line transition radiation source based on low-energy electron beams traversing a multilayer nanostructure”. In: *Phys. Rev. E* 52 (6 1995), pp. 6795–6808.

[Kap+11] V. V. Kaplin, V. V. Sohoreva, S. R. Uglov, O. F. Bulaev, A. A. Voronin, M. Piestrup, and C. Gary. “X-rays generated by relativistic electrons in a waveguide radiator mounted inside a betatron”. In: *Nucl. Instr. Meth. Phys. Res. B* 269 (2011), pp. 1518–1522.

[Kat+10] Y. Katayama, T. Hattori, H. Saitoh, T. Ikeda, K. Aoki, H. Fukui, and K. Funakoshi. “Structure of liquid water under high pressure up to 17 GPa”. In: *Phys. Rev. B* 81.1 (2010), p. 014109. DOI: `10.1103/PhysRevB.81.014109`.

[KHR97] P. K. Kennedy, D. X. Hammer, and B. A. Rockwell. “Laser-induced breakdown in aqueous media”. In: *Prog. Quantum. Electron.* 21.3 (1997), pp. 155–248. DOI: `10.1016/S0079-6727(97)00002-5`.

[Kfi+17] O. Kfir, S. Zayko, C. Nolte, M. Sivis, M. Möller, B. Hebler, S. S. P. K. Arekapudi, D. Steil, S. Schäfer, M. Albrecht, O. Cohen, S. Mathias, and C. Ropers. “Nanoscale magnetic imaging using circularly polarized high-harmonic radiation”. In: *Science Advances* 3.12 (2017), eaao4641. DOI: `10.1126/sciadv.aao4641`.

[Kim+20a] K. H. Kim, K. Amann-Winkel, N. Giovambattista, A. Späh, F. Perakis, H. Pathak, M. L. Parada, C. Yang, D. Mariedahl, T. Eklund, T. J. Lane, S. You, S. Jeong, M. Weston, J. H. Lee, I. Eom, M. Kim, J. Park, S. H. Chun, P. H. Poole, and A. Nilsson. "Experimental observation of the liquid-liquid transition in bulk supercooled water under pressure". In: *Science* 370.6519 (2020), pp. 978–982. DOI: `10.1126/science.abb9385`.

[Kim+20b] K. H. Kim, A. Späh, H. Pathak, C. Yang, S. Bonetti, K. Amann-Winkel, D. Mariedahl, D. Schlesinger, J. A. Sellberg, D. Mendez, G. van der Schot, H. Y. Hwang, J. Clark, O. Shigeki, T. Tadashi, Y. Harada, H. Ogasawara, T. Katayama, A. Nilsson, and F. Perakis. "Anisotropic X-Ray Scattering of Transiently Oriented Water". In: *Phys. Rev. Lett.* 125.7 (2020), p. 076002. DOI: `10.1103/PhysRevLett.125.076002`.

[Kim+20c] T. Kim, J. Liang, L. Zhu, and L. V. Wang. "Picosecond-resolution phase-sensitive imaging of transparent objects in a single shot". In: *Sci. Adv.* 6.3 (2020), eaay6200. DOI: `10.1126/sciadv.aay6200`.

[KB42] J. G. Kirkwood and H. A. Bethe. "The pressure wave produced by an underwater explosion". In: *Office of Scientific Research and Development, Report no. 588* (1942).

[Kla+19] I. Klačková, G. Blaj, P. Denes, A. Dragone, S. Göde, S. Hauf, F. Januschek, J. Joseph, and M. Kuster. "Characterization of the ePix100a and the FastCCd semiconductor detectors for the European XFEL". In: *Journal of Instrumentation* 14.01 (2019), pp. C01008–C01008. DOI: `10.1088/1748-0221/14/01/c01008`.

[KDH71] R. T. Knapp, J. W. Daily, and F. G. Hammit. "Cavitation". In: McGraw-Hill, New York, 1971, pp. 117–131.

[Koc+16] M. Koch, C. Lechner, F. Reuter, K. Köhler, R. Mettin, and W. Lauterborn. "Numerical modeling of laser generated cavitation bubbles with the finite volume and volume of fluid method, using OpenFOAM". In: *Comput. Fluids* 126 (2016), pp. 71–90.

[KLV35] W. Kossel, V. Loeck, and H. Voges. "Die Richtungsverteilung der in einem Kristall entstandenen charakteristischen Röntgenstrahlung". In: *Zeitschrift für Physik* 94.1 (1935), pp. 139–144.

[Krü+12] S. P. Krüger, H. Neubauer, M. Bartels, S. Kalbfleisch, K. Giewekemeyer, P. J. Wilbrandt, M. Sprung, and T. Salditt. "Sub-10 nm beam confinement by X-ray waveguides: design, fabrication and characterization of optical properties". In: *J. Synchrotron Radiat.* 19.2 (2012), pp. 227–236.

[LSK91] A. L'Huillier, K. J. Schafer, and K. C. Kulander. "Higher-order harmonic generation in xenon at 1064 nm: The role of phase matching". In: *Physical Review Letters* 66.17 (1991), pp. 2200–2203. DOI: `10.1103/PhysRevLett.66.2200`.

[Lag+97] S. Lagomarsino, A. Cedola, P. Cloetens, S. Di Fonzo, W. Jark, G. Soullie, and C. Riekel. "Phase contrast hard x-ray microscopy with submicron resolution". In: *Appl. Phys. Lett.* 71.18 (1997), pp. 2557–2559.

[LL91] L. D. Landau and E. M. Lifschitz. *Hydrodynamik*. Berlin: Akademie Verlag, 1991.

[Lau72] W. Lauterborn. "High-speed photography of laser-induced breakdown in liquids". In: *Appl. Phys. Lett.* 21.1 (1972), pp. 27–29. DOI: `10.1063/1.1654204`.

[LK10] W. Lauterborn and T. Kurz. "Physics of bubble oscillations". In: *Rep. Prog. Phys.* 73.10 (2010), p. 106501.

[LV13] W. Lauterborn and A. Vogel. "Shock Wave Emission by Laser Generated Bubbles". In: *Bubble Dynamics and Shock Waves*. Ed. by C. F. Delale. Berlin, Heidelberg: Springer Berlin Heidelberg, 2013, pp. 67–103.

[Lee+12] J. S. Lee, B. M. Weon, J. H. Je, and K. Fezzaa. "How Does an Air Film Evolve into a Bubble During Drop Impact?" In: *Physical Review Letters* 109.20 (2012), p. 204501. DOI: `10.1103/PhysRevLett.109.204501`.

[Len+05] B. Lengeler, C. G. Schroer, M. Kuhlmann, B. Benner, T. F. Günzler, O. Kurapova, F. Zontone, A. Snigirev, and I. Snigireva. "Refractive x-ray lenses". In: *J. Phys. D: Appl. Phys.* 38.10A (2005), A218–A222. DOI: `10.1088/0022-3727/38/10A/042`.

[Len+20] D. Lentrodt, K. P. Heeg, C. H. Keitel, and J. Evers. "Ab initio quantum models for thin-film x-ray cavity QED". In: *Phys. Rev. Research* 2 (2 2020), p. 023396. DOI: `10.1103/PhysRevResearch.2.023396`.

[Lid+95] D. R. Lide, G. Baysinger, S. Chemistry, L. I. Berger, R. N. Goldberg, and H. V. Kehiaian. *CRC Handbook of Chemistry and Physics: A Ready-reference Book of Chemical and Physical Data*. CRC Press, 1995. ISBN: 978-0-8493-0595-5.

[Lim+17] M. F. Limonov, M. V. Rybin, A. N. Poddubny, and Y. S. Kivshar. “Fano resonances in photonics”. In: *Nat. Photonics* 11.9 (2017), pp. 543–554. DOI: `10.1038/nphoton.2017.142`.

[LL03] O. Lindau and W. Lauterborn. “Cinematographic observation of the collapse and rebound of a laser-produced cavitation bubble near a wall”. In: *J. Fluid Mech.* 479 (2003), pp. 327–348. DOI: `10.1017/S0022112002003695`.

[Lip+18] N. Lipsman, Y. Meng, A. J. Bethune, Y. Huang, B. Lam, M. Masellis, N. Herrmann, C. Heyn, I. Aubert, A. Boutet, G. S. Smith, K. Hynynen, and S. E. Black. “Blood–brain barrier opening in Alzheimer’s disease using MR-guided focused ultrasound”. In: *Nat. Commun.* 9.1 (2018), p. 2336. DOI: `10.1038/s41467-018-04529-6`.

[Liu+03] W. Liu, O. Kosareva, I. S. Golubtsov, A. Iwasaki, A. Becker, V. P. Kandidov, and S. L. Chin. “Femtosecond laser pulse filamentation versus optical breakdown in H2O”. In: *Appl. Phys. B* 76.3 (2003), pp. 215–229. DOI: `10.1007/s00340-002-1087-1`.

[Loh+20] L. M. Lohse, A.-L. Robisch, M. Töpperwien, S. Maretzke, M. Krenkel, J. Hagemann, and T. Salditt. “A phase-retrieval toolbox for X-ray holography and tomography”. In: *J. Synchrotron Radiat.* 27.3 (2020), pp. 852–859. DOI: `10.1107/S1600577520002398`.

[Lor17] Lord Rayleigh. “On the pressure developed in a liquid during the collapse of a spherical cavity”. In: *London, Edinburgh, Dublin Philos. Mag. J. Sci.* 34.200 (1917), pp. 94–98.

[Luk05] D. R. Luke. “Relaxed averaged alternating reflections for diffraction imaging”. In: *Inverse Probl.* 21.1 (2005), pp. 37–50. DOI: `10.1088/0266-5611/21/1/004`.

[LBL02] D. R. Luke, J. V. Burke, and R. G. Lyon. “Optical Wavefront Reconstruction: Theory and Numerical Methods”. In: *SIAM Rev.* 44.2 (2002), pp. 169–224. DOI: `10.1137/S003614450139075`.

[MAT13] I. D. R. Mackinnon, J. A. Alarco, and P. C. Talbot. “Metal Hexaborides with Sc, Ti or Mn”. In: *Modeling and Numerical Simulation of Material Science* 3.4 (2013), pp. 158–169. DOI: `10.4236/mnsms.2013.34023`.

[Mad+21] A. Madsen, J. Hallmann, G. Ansaldi, T. Roth, W. Lu, C. Kim, U. Boesenberg, A. Zozulya, J. Möller, R. Shayduk, M. Scholz, A. Bartmann, A. Schmidt, I. Lobato, K. Sukharnikov, M. Reiser, K. Kazarian, and I. Petrov. “Materials Imaging and Dynamics (MID) instrument at the European X-ray Free-Electron Laser Facility”. In: *J Synchrotron Rad* 28.2 (2021). DOI: `10.1107/S1600577521001302`.

[Mad+13] A. Madsen, J. Hallmann, T. Roth, and G. Ansaldi. *Technical Design Report: Scientific Instrument MID*. Tech. rep. XFEL.EU TR-2013-005. E, 2013, pp. 1–191. DOI: `10.3204/XFEL.EU/TR-2013-005`.

[MW14] E. Maire and P. J. Withers. “Quantitative X-ray tomography”. In: *International Materials Reviews* 59.1 (2014), pp. 1–43. DOI: `10.1179/1743280413Y.0000000023`.

[McP+87] A. McPherson, G. Gibson, H. Jara, U. Johann, T. S. Luk, I. A. McIntyre, K. Boyer, and C. K. Rhodes. “Studies of multiphoton production of vacuum-ultraviolet radiation in the rare gases”. In: *JOSA B* 4.4 (1987), pp. 595–601. DOI: `10.1364/JOSAB.4.000595`.

[MS17] L. Melchior and T. Salditt. “Finite difference methods for stationary and time-dependent X-ray propagation”. In: *Opt. Express* 25 (2017), pp. 32090–32109. DOI: `10.1364/OE.25.032090`.

[Mel09] M. Mell. “Phase Contrast Imaging of Lipid Bilayer Model Membranes using Hard X-Rays”. Diplomarbeit. Germany: Georg-August-Universität, Göttingen, 2009.

[Men+19] M. H. Mendenhall, L. T. Hudson, C. I. Szabo, A. Henins, and J. P. Cline. “The molybdenum K-shell x-ray emission spectrum”. In: *J. Phys. B* 52.21 (2019), p. 215004. DOI: `10.1088/1361-6455/ab45d6`.

[Mia+99] J. Miao, P. Charalambous, J. Kirz, and D. Sayre. “Extending the methodology of X-ray crystallography to allow imaging of micrometre-sized non-crystalline specimens”. In: *Nature* 400.6742 (1999), pp. 342–344. DOI: `10.1038/22498`.

[MCW84] O. Mishima, L. D. Calvert, and E. Whalley. "'Melting ice' I at 77 K and 10 kbar: a new method of making amorphous solids". In: *Nature* 310.5976 (1984), pp. 393–395. DOI: `10.1038/310393a0`.

[MS98] O. Mishima and H. E. Stanley. "The relationship between liquid, supercooled and glassy water". In: *Nature* 396.6709 (1998), pp. 329–335. DOI: `10.1038/24540`.

[Mom+96] A. Momose, T. Takeda, Y. Itai, and K. Hirano. "Phase–contrast X–ray computed tomography for observing biological soft tissues". In: *Nature Medicine* 2.4 (1996), pp. 473–475. DOI: `10.1038/nm0496-473`.

[MCY97] W. C. Moss, D. B. Clarke, and D. A. Young. "Calculated Pulse Widths and Spectra of a Single Sonoluminescing Bubble". In: *Science* 276.5317 (1997), pp. 1398–1401. DOI: `10.1126/science.276.5317.1398`.

[Nac+14] F. Nachtrab, M. Firsching, N. Uhlmann, C. Speier, P. Takman, T. Tuohimaa, C. Heinzl, J. Kastner, D. H. Larsson, A. Holmberg, G. Berti, M. Krumm, and C. Sauerwein. "NanoXCT: development of a laboratory nano-CT system". In: *Developments in X-Ray Tomography IX*. Vol. 9212. International Society for Optics and Photonics, 2014, p. 92120L. DOI: `10.1117/12.2061752`.

[NV96] K. Nahen and A. Vogel. "Plasma formation in water by picosecond and nanosecond Nd:YAG laser pulses. II. Transmission, scattering, and reflection". In: *IEEE J. Sel. Top. Quantum Electron.* 2.4 (1996), pp. 861–871. DOI: `10.1109/2944.577308`.

[Neu+14] H. Neubauer, S. Hoffmann, M. Kanbach, J. Haber, S. Kalbfleisch, S. P. Krüger, and T. Salditt. "High aspect ratio x-ray waveguide channels fabricated by e-beam lithography and wafer bonding". In: *Journal of Applied Physics* 115.21 (2014), p. 214305. DOI: `10.1063/1.4881495`.

[NM12] R. Neutze and K. Moffat. "Time-resolved structural studies at synchrotrons and X-ray free electron lasers: opportunities and challenges". In: *Current Opinion in Structural Biology* 22.5 (2012), pp. 651–659. DOI: `10.1016/j.sbi.2012.08.006`.

[Neu+00] R. Neutze, R. Wouts, D. van der Spoel, E. Weckert, and J. Hajdu. "Potential for biomolecular imaging with femtosecond X-ray pulses". In: *Nature* 406.6797 (2000), pp. 752–757. DOI: `10.1038/35021099`.

[Nic+17] J.-D. Nicolas, M. Bernhardt, M. Krenkel, C. Richter, S. Luther, and T. Salditt. "Combined scanning X-ray diffraction and holographic imaging of cardiomyocytes". In: *J Appl Cryst* 50.2 (2017), pp. 612–620. DOI: `10.1107/S1600576717003351`.

[NP20] A. Nilsson and F. Perakis. "X-Ray Studies of Water". In: *Synchrotron Light Sources and Free-Electron Lasers: Accelerator Physics, Instrumentation and Science Applications*. Ed. by E. J. Jaeschke, S. Khan, J. R. Schneider, and J. B. Hastings. Cham: Springer International Publishing, 2020, pp. 1935–1988. ISBN: 978-3-030-23201-6. DOI: `10.1007/978-3-030-23201-6_69`.

[NP15] A. Nilsson and L. G. M. Pettersson. "The structural origin of anomalous properties of liquid water". In: *Nature Communications* 6.1 (2015), p. 8998. DOI: `10.1038/ncomms9998`.

[NV99] J. Noack and A. Vogel. "Laser-induced plasma formation in water at nanosecond to femtosecond time scales: calculation of thresholds, absorption coefficients, and energy density". In: *IEEE J. Quantum Electron.* 35.8 (1999), pp. 1156–1167. DOI: `10.1109/3.777215`.

[NW06] J. Nocedal and S. Wright. *Numerical optimization*. Springer Science & Business Media, 2006.

[NGS06] E. Nováková, K. Giewekemeyer, and T. Salditt. "Structure of two-component lipid membranes on solid support: An x-ray reflectivity study". In: *Physical Review E* 74.5 (2006), p. 051911. DOI: `10.1103/PhysRevE.74.051911`.

[ODG94] A. V. Okhulkov, Y. N. Demianets, and Y. E. Gorbaty. "X-ray scattering in liquid water at pressures of up to 7.7 kbar: Test of a fluctuation model". In: *J. Chem. Phys.* 100.2 (1994), pp. 1578–1588. DOI: `10.1063/1.466584`.

[Ost+21] M. Osterhoff, M. Vassholz, H. P. Hoeppe, J. M. Rosselló, R. Mettin, J. Hagemann, J. Möller, J. Hallmann, M. Scholz, R. Schaffer, U. Boesenberg, C. Kim, A. Zozulya, W. Lu, R. Shayduk, A. Madsen, and T. Salditt. "Nanosecond timing and synchronization scheme for holographic pump–probe studies at the MID instrument at European XFEL". In: *J. Synchrotron Rad.* 28 (2021). DOI: `10.1107/S1600577521003052`.

[Ote+08] M. Otendal, T. Tuohimaa, U. Vogt, and H. M. Hertz. “A 9 keV electron-impact liquid-gallium-jet x-ray source”. In: *Rev. Sci. Instrum.* 79.1 (2008), p. 016102. DOI: `10.1063/1.2833838`.

[Pag+02] D. Paganin, S. C. Mayo, T. E. Gureyev, P. R. Miller, and S. W. Wilkins. “Simultaneous phase and amplitude extraction from a single defocused image of a homogeneous object”. In: *J. Microsc.* 206.1 (2002), pp. 33–40. DOI: `10.1046/j.1365-2818.2002.01010.x`.

[Pag06] D. Paganin. *Coherent X-Ray Optics*. Oxford University Press, 2006.

[Par54] L. G. Parratt. “Surface Studies of Solids by Total Reflection of X-Rays”. In: *Phys. Rev.* 95.2 (1954), pp. 359–369.

[Pas08] R. Paschotta. *Encyclopedia of laser physics and technology*. 1st ed. Wiley-VCH, 2008. ISBN: 978-3-527-40828-3.

[Per+17] F. Perakis, K. Amann-Winkel, F. Lehmkühler, M. Sprung, D. Mariedahl, J. A. Sellberg, H. Pathak, A. Späh, F. Cavalca, D. Schlesinger, A. Ricci, A. Jain, B. Massani, F. Aubree, C. J. Benmore, T. Loerting, G. Grübel, L. G. M. Pettersson, and A. Nilsson. “Diffusive dynamics during the high-to-low density transition in amorphous ice”. In: *PNAS* 114.31 (2017), pp. 8193–8198. DOI: `10.1073/pnas.1705303114`.

[Pfe+02] F. Pfeiffer, C. David, M. Burghammer, C. Riekel, and T. Salditt. “Two-Dimensional X-ray Waveguides and Point Sources”. In: *Science* 297.6 (2002), pp. 230–234. DOI: `10.1126/science.1071994`.

[Pfe+00] F. Pfeiffer, T. Salditt, P. Høghøj, I. Anderson, and N. Schell. “X-ray waveguides with multiple guiding layers”. In: *Physical Review B* 62.24 (2000), pp. 16939–16943. DOI: `10.1103/PhysRevB.62.16939`.

[PP77] M. S. Plesset and A. Prosperetti. “Bubble Dynamics and Cavitation”. In: *Ann. Rev. Fluid Mech.* 9 (1977), pp. 145–85.

[PGW97] A. Pogany, D. Gao, and S. W. Wilkins. “Contrast and resolution in imaging with a microfocus x-ray source”. In: *Review of Scientific Instruments* 68.7 (1997), pp. 2774–2782. DOI: `10.1063/1.1148194`.

[PS78] A. Prosperetti and G. Seminara. “Linear stability of a growing or collapsing bubble in a slightly viscous liquid”. In: *The Physics of Fluids* 21.9 (1978), pp. 1465–1470. DOI: `10.1063/1.862408`.

[Pur46] E. M. Purcell. “Spontaneous emission probabilities at radio frequencies”. In: *Phys. Rev.* 69 (1946), p. 681.

[Pus02] W. A. Pusey. “Cases of Sarcoma and of Hodgkin’s Disease Treated by Exposures to X-rays — A Preliminary Report.” In: *Journal of the American Medical Association* XXXVIII.3 (1902), pp. 166–169. DOI: `10.1001/jama.1902.62480030024001h`.

[Ram+17] M. Ramilli, A. Bergamaschi, M. Andrae, M. Brückner, S. Cartier, R. Dinapoli, E. Fröjdh, D. Greiffenberg, T. Hutwelker, C. Lopez-Cuenca, D. Mezza, A. Mozzanica, M. Ruat, S. Redford, B. Schmitt, X. Shi, G. Tinti, and J. Zhang. “Measurements with MÖNCH, a 25 μm pixel pitch hybrid pixel detector”. In: *J. Instrum.* 12 (2017), pp. C01071–C01071. DOI: `10.1088/1748-0221/12/01/c01071`.

[Rei+00] C. Reich, P. Gibbon, I. Uschmann, and E. Förster. “Yield Optimization and Time Structure of Femtosecond Laser Plasma Kα Sources”. In: *Physical Review Letters* 84.21 (2000), pp. 4846–4849. DOI: `10.1103/PhysRevLett.84.4846`.

[Rei+01] C. Reich, P. Gibbon, I. Uschmann, and E. Förster. “Numerical studies on the properties of femtosecond laser plasma Kα sources”. In: *Laser and Particle Beams* 19.1 (2001), p. 147.

[RW57] M. H. Rice and J. M. Walsh. “Equation of State of Water to 250 Kilobars”. In: *J. Chem. Phys.* 26.4 (1957), pp. 824–830. DOI: `10.1063/1.1743415`.

[RAH47] J. M. Richardson, A. B. Arons, and R. R. Halverson. “Hydrodynamic Properties of Sea Water at the Front of a Shock Wave”. In: *J. Chem. Phys.* 15.11 (1947), pp. 785–794. DOI: `10.1063/1.1746334`.

[Rid88] S. Ridah. “Shock waves in water”. In: *J. Appl. Phys.* 64.1 (1988), pp. 152–158. DOI: `10.1063/1.341448`.

[Roc99] J. J. Rocca. “Table-top soft x-ray lasers”. In: *Review of Scientific Instruments* 70.10 (1999), pp. 3799–3827. DOI: `10.1063/1.1150041`.

[Roh20] A. Rohatgi. *Webplotdigitizer: Version 4.4.* 2020. URL: `https://automeris.io/WebPlotDigitizer`.

[Röh+05] R. Röhlsberger, K. Schlage, T. Klein, and O. Leupold. “Accelerating the Spontaneous Emission of X Rays from Atoms in a Cavity”. In: *Phys. Rev. Lett.* 95 (9 2005), p. 097601.

[Röh+10] R. Röhlsberger, K. Schlage, B. Sahoo, S. Couet, and R. Rüffer. “Collective Lamb Shift in Single-Photon Superradiance”. In: *Science* 328.5983 (2010), pp. 1248–1251.

[Röh+12] R. Röhlsberger, H.-C. Wille, K. Schlage, and B. Sahoo. "Electromagnetically induced transparency with resonant nuclei in a cavity". In: *Nature* 482 (2012), pp. 199–203.

[RE21] R. Röhlsberger and J. Evers. "Quantum Optical Phenomena in Nuclear Resonant Scattering". In: *Modern Mössbauer Spectroscopy: New Challenges Based on Cutting-Edge Techniques*. Ed. by Y. Yoshida and G. Langouche. Topics in Applied Physics. Singapore: Springer, 2021, pp. 105–171. DOI: `10.1007/978-981-15-9422-9_3`.

[RES20] R. Röhlsberger, J. Evers, and S. Shwartz. "Quantum and Nonlinear Optics with Hard X-Rays". In: *Synchrotron Light Sources and Free-Electron Lasers: Accelerator Physics, Instrumentation and Science Applications*. Ed. by E. J. Jaeschke, S. Khan, J. R. Schneider, and J. B. Hastings. Cham: Springer International Publishing, 2020, pp. 1399–1431. ISBN: 978-3-030-23201-6. DOI: `10.1007/978-3-030-23201-6_32`.

[Roh17] N. Rohringer. "Photoionisation Inner-shell X-ray Lasers". In: *X-Ray Free Electron Lasers: Applications in Materials, Chemistry and Biology*. Ed. by U. Bergman, V. K. Yachandra, and J. Yano. Royal Society of Chemistry, 2017. ISBN: 978-1-84973-100-3.

[Roh+12] N. Rohringer, D. Ryan, R. A. London, M. Purvis, F. Albert, J. Dunn, J. D. Bozek, C. Bostedt, A. Graf, R. Hill, S. P. Hau-Riege, and J. J. Rocca. "Atomic inner-shell X-ray laser at 1.46 nanometres pumped by an X-ray free-electron laser". In: *Nature* 481.7382 (2012), pp. 488–491. DOI: `10.1038/nature10721`.

[Rön49] W. C. Röntgen. "Aus dem Bericht der III. Sitzung vom 23. Januar 1896". In: *Über Eine Neue Art von Strahlen*. Ed. by W. C. Röntgen. Berlin, Heidelberg: Springer, 1949, pp. 1–1. ISBN: 978-3-662-13247-0. DOI: `10.1007/978-3-662-13247-0_1`.

[Rou+94] A. Rousse, P. Audebert, J. P. Geindre, F. Falliès, J. C. Gauthier, A. Mysyrowicz, G. Grillon, and A. Antonetti. "Efficient Kα x-ray source from femtosecond laser-produced plasmas". In: *Physical Review E* 50.3 (1994), pp. 2200–2207. DOI: `10.1103/PhysRevE.50.2200`.

[RS16] A. Ruhlandt and T. Salditt. "Three-dimensional propagation in near-field tomographic X-ray phase retrieval". In: *Acta Crystallographica Section*

A: Foundations and Advances 72.2 (2016), pp. 215–221. DOI: `10.1107/S2053273315022469`.

[Ruh+17] A. Ruhlandt, M. Töpperwien, M. Krenkel, R. Mokso, and T. Salditt. "Four dimensional material movies: High speed phase-contrast tomography by backprojection along dynamically curved paths". In: *Scientific Reports* 7.1 (2017), p. 6487. DOI: `10.1038/s41598-017-06333-6`.

[Sac91] C. A. Sacchi. "Laser-induced electric breakdown in water". In: *J. Opt. Soc. Am. B, JOSAB* 8.2 (1991), pp. 337–345. DOI: `10.1364/JOSAB.8.000337`.

[SSY00] E. Saldin, E. V. Schneidmiller, and M. V. Yurkov. *The Physics of Free Electron Lasers*. Advanced Texts in Physics. Berlin Heidelberg: Springer-Verlag, 2000. ISBN: 978-3-540-66266-2. DOI: `10.1007/978-3-662-04066-9`.

[Sal+15a] T. Salditt, S. Hoffmann, M. Vassholz, J. Haber, M. Osterhoff, and J. Hilhorst. "X-Ray Optics on a Chip: Guiding X Rays in Curved Channels". In: *Phys. Rev. Lett.* 115 (2015), p. 203902.

[Sal+15b] T. Salditt, M. Osterhoff, M. Krenkel, R. Wilke, M. Priebe, M. Bartels, S. Kalbfleisch, and M. Sprung. "Compound focusing mirror and X-ray waveguide optics for coherent imaging and nano-diffraction". In: *J. Synchrotron Radiat.* 22.4 (2015), pp. 867–878. DOI: `10.1107/S1600577515007742`.

[Sal+03] T. Salditt, F. Pfeiffer, H. Perzl, A. Vix, U. Mennicke, A. Jarre, A. Mazuelas, and T. H. Metzger. "X-ray waveguides and thin macromolecular films". In: *Physica B: Condensed Matter*. Proceedings of the Seventh International Conference on Surface X-ray and Neutron Scattering 336.1 (2003), pp. 181–192. DOI: `10.1016/S0921-4526(03)00288-6`.

[Sal15] F. Salvat. "PENELOPE-2014: A Code System for Monte Carlo Simulation of Electron and Photon Transport". In: *OECD NEA Data Bank, NEA/NSC/DOC(2015)3* (2015).

[Sal+02] D. Salzmann, C. Reich, I. Uschmann, E. Förster, and P. Gibbon. "Theory of Kα generation by femtosecond laser-produced hot electrons in thin foils". In: *Physical Review E* 65.3 (2002), p. 036402. DOI: `10.1103/PhysRevE.65.036402`.

[Sch+13] S. Schaffert, B. Pfau, J. Geilhufe, C. M. Günther, M. Schneider, C. v. K. Schmising, and S. Eisebitt. “High-resolution magnetic-domain imaging by Fourier transform holography at 21 nm wavelength”. In: *New Journal of Physics* 15.9 (2013), p. 093042. DOI: `10.1088/1367-2630/15/9/093042`.

[Sch+12] D. Schanz, B. Metten, T. Kurz, and W. Lauterborn. “Molecular dynamics simulations of cavitation bubble collapse and sonoluminescence”. In: *New J. Phys.* 14.11 (2012), p. 113019.

[Sch+95] G. Schmahl, D. Rudolph, P. Guttmann, G. Schneider, J. Thieme, and B. Niemann. “Phase contrast studies of biological specimens with the x-ray microscope at BESSY (invited)”. In: *Review of Scientific Instruments* 66.2 (1995), pp. 1282–1286. DOI: `10.1063/1.1145955`.

[Sch+11] T. Schoonjans, A. Brunetti, B. Golosio, M. Sanchez del Rio, V. A. Solé, C. Ferrero, and L. Vincze. “The xraylib library for X-ray–matter interactions. Recent developments”. In: *Spectrochim. Acta B* 66.11 (2011), pp. 776–784. DOI: `10.1016/j.sab.2011.09.011`.

[Sch+01] C. G. Schroer, B. Lengeler, B. Benner, T. F. Guenzler, M. Kuhlmann, A. S. Simionovici, S. Bohic, M. Drakopoulos, A. A. Snigirev, I. Snigireva, and W. H. Schroeder. “Microbeam production using compound refractive lenses: beam characterization and applications”. In: *X-Ray Micro- and Nano-Focusing: Applications and Techniques II*. Vol. 4499. International Society for Optics and Photonics, 2001, pp. 52–63. DOI: `10.1117/12.450222`.

[Sch+15] A. Schropp, R. Hoppe, V. Meier, J. Patommel, F. Seiboth, Y. Ping, D. G. Hicks, M. A. Beckwith, G. W. Collins, A. Higginbotham, J. S. Wark, H. J. Lee, B. Nagler, E. C. Galtier, B. Arnold, U. Zastrau, J. B. Hastings, and C. G. Schroer. “Imaging Shock Waves in Diamond with Both High Temporal and Spatial Resolution at an XFEL”. In: *Sci. Rep.* 5.1 (2015), p. 11089. DOI: `10.1038/srep11089`.

[Sch+18] K. M. Schulz, D. Jalas, A. Y. Petrov, and M. Eich. “Reciprocity approach for calculating the Purcell effect for emission into an open optical system”. In: *Opt. Express* 26.15 (2018), pp. 19247–19258. DOI: `10.1364/OE.26.019247`.

[Sei+11] M. M. Seibert et al. “Single mimivirus particles intercepted and imaged with an X-ray laser”. In: *Nature* 470.7332 (2011), pp. 78–81. DOI: `10.1038/nature09748`.

[Sei+20] F. Seiboth, D. Brückner, M. Kahnt, M. Lyubomirskiy, F. Wittwer, D. Dzhigaev, T. Ullsperger, S. Nolte, F. Koch, C. David, J. Garrevoet, G. Falkenberg, and C. G. Schroer. “Hard X-ray wavefront correction via refractive phase plates made by additive and subtractive fabrication techniques”. In: *J Synchrotron Rad* 27.5 (2020), pp. 1121–1130. DOI: `10.1107/S1600577520007900`.

[Sei+18] F. Seiboth et al. “Simultaneous 8.2 keV phase-contrast imaging and 24.6 keV X-ray diffraction from shock-compressed matter at the LCLS”. In: *Appl. Phys. Lett.* 112.22 (2018), p. 221907. DOI: `10.1063/1.5031907`.

[Sei+17a] F. Seiboth, A. Schropp, M. Scholz, F. Wittwer, C. Rödel, M. Wünsche, T. Ullsperger, S. Nolte, J. Rahomäki, K. Parfeniukas, S. Giakoumidis, U. Vogt, U. Wagner, C. Rau, U. Boesenberg, J. Garrevoet, G. Falkenberg, E. C. Galtier, H. Ja Lee, B. Nagler, and C. G. Schroer. “Perfect X-ray focusing via fitting corrective glasses to aberrated optics”. In: *Nature Communications* 8.1 (2017), p. 14623. DOI: `10.1038/ncomms14623`.

[Sei+17b] F. Seiboth, A. Schropp, M. Scholz, F. Wittwer, C. Rödel, M. Wünsche, T. Ullsperger, S. Nolte, J. Rahomäki, K. Parfeniukas, S. Giakoumidis, U. Vogt, U. Wagner, C. Rau, U. Boesenberg, J. Garrevoet, G. Falkenberg, E. C. Galtier, H. J. Lee, B. Nagler, and C. G. Schroer. “Perfect X-ray focusing via fitting corrective glasses to aberrated optics”. In: *Nat. Commun.* 8 (2017), p. 14623.

[Sel+14] J. A. Sellberg et al. “Ultrafast X-ray probing of water structure below the homogeneous ice nucleation temperature”. In: *Nature* 510.7505 (2014), pp. 381–384. DOI: `10.1038/nature13266`.

[Sen03] N. Senn. “Case of spleno-medullary leukemia successfully treated by use of roentgen ray”. In: *Medical Record New York* 63 (1903), pp. 281–282.

[Shv+10] Y. V. Shvyd’ko, S. Stoupin, A. Cunsolo, A. H. Said, and X. Huang. “High-reflectivity high-resolution X-ray crystal optics with diamonds”. In: *Nat. Phys.* 6.3 (2010), pp. 196–199.

[Shv+03] Y. V. Shvyd'ko, M. Lerche, H.-C. Wille, E. Gerdau, M. Lucht, H. D. Rüter, E. E. Alp, and R. Khachatryan. “X-Ray Interferometry with Microelectronvolt Resolution”. In: *Phys. Rev. Lett.* 90 (1 2003), p. 013904. DOI: `10.1103/PhysRevLett.90.013904`.

[Sin+19] G. Sinibaldi, A. Occhicone, F. J. A. Pereira, D. Caprini, L. Marino, F. Michelotti, and C. Casciola. “Laser induced cavitation: Plasma generation and breakdown shockwave”. In: *Phys. Fluids* 31 (2019), p. 103302. DOI: `10.1063/1.5119794`.

[Ski+14] L. B. Skinner, C. J. Benmore, J. C. Neuefeind, and J. B. Parise. “The structure of water around the compressibility minimum”. In: *J. Chem. Phys.* 141.21 (2014), p. 214507. DOI: `10.1063/1.4902412`.

[Sni+95] A. Snigirev, I. Snigireva, V. Kohn, S. Kuznetsov, and I. Schelokov. “On the possibilities of x-ray phase contrast microimaging by coherent high-energy synchrotron radiation”. In: *Review of Scientific Instruments* 66.12 (1995), pp. 5486–5492. DOI: `10.1002/9781119998365`.

[SR00] A. K. Soper and M. A. Ricci. “Structures of High-Density and Low-Density Water”. In: *Phys. Rev. Lett.* 84.13 (2000), pp. 2881–2884. DOI: `10.1103/PhysRevLett.84.2881`.

[SS74] E. Spiller and A. Segmüller. “Propagation of x rays in waveguides”. In: *Appl. Phys. Lett.* 24.2 (1974), pp. 60–61.

[Sta+02] M. Stampanoni, G. Borchert, P. Wyss, R. Abela, B. Patterson, S. Hunt, D. Vermeulen, and P. Rüegsegger. “High resolution X-ray detector for synchrotron-based microtomography”. In: *Nuclear Instruments and Methods in Physics Research Section A: Accelerators, Spectrometers, Detectors and Associated Equipment* 491.1 (2002), pp. 291–301. DOI: `10.1016/S0168-9002(02)01167-1`.

[Sta+16] C. A. Stan, D. Milathianaki, H. Laksmono, R. G. Sierra, T. A. McQueen, M. Messerschmidt, G. J. Williams, J. E. Koglin, T. J. Lane, M. J. Hayes, S. A. H. Guillet, M. Liang, A. L. Aquila, P. R. Willmott, J. S. Robinson, K. L. Gumerlock, S. Botha, K. Nass, I. Schlichting, R. L. Shoeman, H. A. Stone, and S. Boutet. “Liquid explosions induced by X-ray laser pulses”. In: *Nat. Phys.* 12.10 (2016), pp. 966–971. DOI: `10.1038/nphys3779`.

[Str+06] T. Strässle, A. M. Saitta, Y. L. Godec, G. Hamel, S. Klotz, J. S. Loveday, and R. J. Nelmes. "Structure of Dense Liquid Water by Neutron Scattering to 6.5 GPa and 670 K". In: *Phys. Rev. Lett.* 96.6 (2006), p. 067801. DOI: `10.1103/PhysRevLett.96.067801`.

[Tag+16] Y. Tagawa, S. Yamamoto, K. Hayasaka, and M. Kameda. "On pressure impulse of a laser-induced underwater shock wave". In: *Journal of Fluid Mechanics* 808 (2016), pp. 5–18. DOI: `10.1017/jfm.2016.644`.

[Tok+09] G. Toker, V. Bulatov, T. Kovalchuk, and I. Schechter. "Micro-dynamics of optical breakdown in water induced by nanosecond laser pulses of 1064nm wavelength". In: *Chem. Phys. Lett.* 471.4 (2009), pp. 244–248. DOI: `10.1016/j.cplett.2009.02.044`.

[Töp+18] M. Töpperwien, F. van der Meer, C. Stadelmann, and T. Salditt. "Three-dimensional virtual histology of human cerebellum by X-ray phase-contrast tomography". In: *Proc. Natl. Acad. Sci. U.S.A.* 115.27 (2018), pp. 6940–6945. DOI: `10.1073/pnas.1801678115`.

[Tsc+17] T. Tschentscher, C. Bressler, J. Grünert, A. Madsen, A. P. Mancuso, M. Meyer, A. Scherz, H. Sinn, and U. Zastrau. "Photon Beam Transport and Scientific Instruments at the European XFEL". In: *Appl. Sci.* 7 (2017). DOI: `10.3390/app7060592`.

[Tum+09] R. S. Tummidi, R. M. Pafchek, K. Kim, and T. L. Koch. "Modification of spontaneous emission rates in shallow ridge 8.3 nm erbium doped silica slot waveguides". In: *2009 6th IEEE International Conference on Group IV Photonics*. 2009, pp. 226–228.

[Vag+19] P. Vagovič, T. Sato, L. Mikeš, G. Mills, R. Graceffa, F. Mattsson, P. Villanueva-Perez, A. Ershov, T. Faragó, J. Uličný, H. Kirkwood, R. Letrun, R. Mokso, M.-C. Zdora, M. P. Olbinado, A. Rack, T. Baumbach, J. Schulz, A. Meents, H. N. Chapman, and A. P. Mancuso. "Megahertz x-ray microscopy at x-ray free-electron laser and synchrotron sources". In: *Optica* 6.9 (2019), pp. 1106–1109.

[Van+15] V. Van Nieuwenhove, J. De Beenhouwer, F. De Carlo, L. Mancini, F. Marone, and J. Sijbers. "Dynamic intensity normalization using Eigen flat fields in X-ray imaging". In: *Opt. Express* 23.21 (2015), pp. 27975–27989.

[Vas+21] M. Vassholz, H. P. Hoeppe, J. Hagemann, J. M. Rosselló, M. Osterhoff, R. Mettin, T. Kurz, A. Schropp, F. Seiboth, C. G. Schroer, M. Scholz, J. Möller, J. Hallmann, U. Boesenberg, C. Kim, A. Zozulya, W. Lu, R. Shayduk, R. Schaffer, A. Madsen, and T. Salditt. "Pump-Probe X-Ray Holographic Imaging of Laser-Induced Cavitation Bubbles with Femtosecond FEL Pulses". In: *Nature Communications* 12.1 (2021), p. 3468. DOI: `10.1038/s41467-021-23664-1`.

[Vas+16] M. Vassholz, B. Koberstein-Schwarz, A. Ruhlandt, M. Krenkel, and T. Salditt. "New X-Ray Tomography Method Based on the 3D Radon Transform Compatible with Anisotropic Sources". In: *Physical Review Letters* 116.8 (2016), p. 088101. DOI: `10.1103/PhysRevLett.116.088101`.

[VS21] M. Vassholz and T. Salditt. "Observation of electron-induced characteristic x-ray and bremsstrahlung radiation from a waveguide cavity". In: *Science Advances* 7.4 (2021), eabd5677. DOI: `10.1126/sciadv.abd5677`.

[Vey+18] D. Veysset, U. Gutiérrez-Hernández, L. Dresselhaus-Cooper, F. De Colle, S. Kooi, K. A. Nelson, P. A. Quinto-Su, and T. Pezeril. "Single-bubble and multibubble cavitation in water triggered by laser-driven focusing shock waves". In: *Physical Review E* 97.5 (2018), p. 053112. DOI: `10.1103/PhysRevE.97.053112`.

[Vey+16] D. Veysset, A. A. Maznev, T. Pezeril, S. Kooi, and K. A. Nelson. "Interferometric analysis of laser-driven cylindrically focusing shock waves in a thin liquid layer". In: *Scientific Reports* 6.1 (2016), p. 24. DOI: `10.1038/s41598-016-0032-1`.

[Vir+20] P. Virtanen et al. "SciPy 1.0: fundamental algorithms for scientific computing in Python". In: *Nat. Methods* 17.3 (2020), pp. 261–272. DOI: `10.1038/s41592-019-0686-2`.

[VBP96] A. Vogel, S. Busch, and U. Parlitz. "Shock wave emission and cavitation bubble generation by picosecond and nanosecond optical breakdown in water". In: *J. Acoust. Soc. Am.* 100.1 (1996), pp. 148–165.

[Vog+96] A. Vogel, K. Nahen, D. Theisen, and J. Noack. "Plasma formation in water by picosecond and nanosecond Nd:YAG laser pulses. I. Optical breakdown at threshold and superthreshold irradiance". In: *IEEE J. Sel. Top. Quantum Electron.* 2.4 (1996), pp. 847–860. DOI: `10.1109/2944.577307`.

[Vog+99] A. Vogel, J. Noack, K. Nahen, D. Theisen, S. Busch, U. Parlitz, D. X. Hammer, G. D. Noojin, B. A. Rockwell, and R. Birngruber. “Energy balance of optical breakdown in water at nanosecond to femtosecond time scales”. In: *Appl. Phys. B* 68.2 (1999), pp. 271–280.

[VSY99] V. Q. Vuong, A. J. Szeri, and D. A. Young. “Shock formation within sonoluminescence bubbles”. In: *Phys. Fluids* 11.1 (1999), pp. 10–17. DOI: `10.1063/1.869920`.

[Wal+14] S. M. Walker, D. A. Schwyn, R. Mokso, M. Wicklein, T. Müller, M. Doube, M. Stampanoni, H. G. Krapp, and G. K. Taylor. “In Vivo Time-Resolved Microtomography Reveals the Mechanics of the Blowfly Flight Motor”. In: *PLOS Biology* 12.3 (2014), e1001823. DOI: `10.1371/journal.pbio.1001823`.

[Wan+12] T. Wang et al. “Femtosecond Single-Shot Imaging of Nanoscale Ferromagnetic Order in Co/Pd Multilayers Using Resonant X-Ray Holography”. In: *Physical Review Letters* 108.26 (2012), p. 267403. DOI: `10.1103/PhysRevLett.108.267403`.

[Wan+08] Y. Wang, E. Granados, F. Pedaci, D. Alessi, B. Luther, M. Berrill, and J. J. Rocca. “Phase-coherent, injection-seeded, table-top soft-X-ray lasers at 18.9 nm and 13.9 nm”. In: *Nature Photonics* 2.2 (2008), pp. 94–98. DOI: `10.1038/nphoton.2007.280`.

[Wec+09] G. Weck, J. Eggert, P. Loubeyre, N. Desbiens, E. Bourasseau, J.-B. Maillet, M. Mezouar, and M. Hanfland. “Phase diagrams and isotopic effects of normal and deuterated water studied via x-ray diffraction up to 4.5 GPa and 500 K”. In: *Phys. Rev. B* 80.18 (2009), p. 180202. DOI: `10.1103/PhysRevB.80.180202`.

[Wil+17] F. Willems, C. von Korff Schmising, D. Weder, C. M. Günther, M. Schneider, B. Pfau, S. Meise, E. Guehrs, J. Geilhufe, A. E. D. Merhe, E. Jal, B. Vodungbo, J. Lüning, B. Mahieu, F. Capotondi, E. Pedersoli, D. Gauthier, M. Manfredda, and S. Eisebitt. “Multi-color imaging of magnetic Co/Pt heterostructures”. In: *Structural Dynamics* 4.1 (2017), p. 014301. DOI: `10.1063/1.4976004`.

[Wil03] F. H. Williams. *The Roentgen rays in medicine and surgery as an aid in diagnosis and as a therapeutic agent*. New York: Macmillan, 1903.

[Wit+09] Y. D. Witte, M. Boone, J. Vlassenbroeck, M. Dierick, and L. V. Hoorebeke. “Bronnikov-aided correction for x-ray computed tomography”. In: *JOSA A* 26.4 (2009), pp. 890–894. DOI: `10.1364/JOSAA.26.000890`.

[WR93] C. C. Wu and P. H. Roberts. “Shock-wave propagation in a sonoluminescing gas bubble”. In: *Phys. Rev. Lett.* 70 (22 1993), pp. 3424–3427. DOI: `10.1103/PhysRevLett.70.3424`.

[WL04] X. Wu and H. Liu. “A new theory of phase-contrast x-ray imaging based on Wigner distributions”. In: *Medical Physics* 31.9 (2004), pp. 2378–2384. DOI: `https://doi.org/10.1118/1.1776672`.

[WL07] X. Wu and H. Liu. “Clarification of aspects in in-line phase-sensitive x-ray imaging”. In: *Medical Physics* 34.2 (2007), pp. 737–743. DOI: `https://doi.org/10.1118/1.2431475`.

[You+10] L. Young et al. “Femtosecond electronic response of atoms to ultra-intense X-rays”. In: *Nature* 466.7302 (2010), pp. 56–61. DOI: `10.1038/nature09177`.

[YKL16] W. Yun, J. Kirz, and S. J. Y. Lewis. “Structured targets for x-ray generation”. US20160064175A1. 2016.

[Zwa+99] M. J. Zwanenburg, J. F. Peters, J. H. H. Bongaerts, S. A. de Vries, D. L. Abernathy, and J. F. van der Veen. “Coherent Propagation of X Rays in a Planar Waveguide with a Tunable Air Gap”. In: *Phys. Rev. Lett.* 82.8 (1999), pp. 1696–1699.

Author contributions

Author contributions chapter 2: The author contributions of chapter 2 are detailed at the end of the chapter on page 39.

Author contributions chapter 3: The author contributions of chapter 3 are detailed at the end of the chapter on page 62.

Contributions of collaborators chapter 4: M. Vassholz, H.P. Hoeppe, J.M. Rosselló, J. Hagemann, and M. Osterhoff prepared the experiment from the user side, with support and advice from T. Salditt, and R. Mettin. J. Möller, M. Scholz, U. Boesenberg, J. Hallmann, C. Kim, A. Zozulya, W. Lu, R. Shayduk, led by A. Madsen (MID team) prepared and contributed instrumentation and experimental technology of the beamline, complemented by synchronisation and integration work by M. Osterhoff, M. Vassholz, and H.P. Hoeppe. M. Vassholz, H.P. Hoeppe, J. Hagemann, J.M. Rosselló, M. Osterhoff, and T. Salditt performed the XFEL experiment with the MID team. M. Vassholz analyzed the WAXS data with input from T. Salditt, M. Osterhoff, J. Hagemann, and H.P. Hoeppe. J. Hagemann analyzed the holography data in close discussion with M. Vassholz, M. Osterhoff, H.P. Hoeppe, and T. Salditt. The manuscript was written by M. Vassholz with input from T. Salditt, J. Hagemann, M. Osterhoff, H.P. Hoeppe, and A. Madsen. T. Salditt and J. Hagemann authored the proposal of the XFEL experiment with help from M. Osterhoff, T. Kurz, and R. Mettin.

List of publications

---

1. On incoherent diffractive imaging. L. M. Lohse, M. Vassholz, and T. Salditt. In: *Acta Crystallographica Section A: Foundations and Advances*, 77(5):480–496, 2021. DOI: `10.1107/S2053273321007300`.
2. Pump-probe X-ray holographic imaging of laser-induced cavitation bubbles with femtosecond FEL pulses. M. Vassholz, H. P. Hoeppe, J. Hagemann, J. M. Rosselló, M. Osterhoff, R. Mettin, T. Kurz, A. Schropp, F. Seiboth, C. G. Schroer, M. Scholz, J. Möller, J. Hallmann, U. Boesenberg, C. Kim, A. Zozulya, W. Lu, R. Shayduk, R. Schaffer, A. Madsen, and T. Salditt. In: *Nature Communications*, 12(1):3468, 2021. DOI: `10.1038/s41467-021-23664-1`.
3. In-line holography with hard X-rays at sub-15 nm resolution. J. Soltau, M. Vassholz, M. Osterhoff, and T. Salditt. In: *Optica*, 8(6):818–823, 2021. DOI: `10.1364/OPTICA.420060`.
4. Nanosecond timing and synchronization scheme for holographic pump–probe studies at the MID instrument at European XFEL. M. Osterhoff, M. Vassholz, H. P. Hoeppe, J. M. Rosselló, R. Mettin, J. Hagemann, J. Möller, J. Hallmann, M. Scholz, R. Schaffer, U. Boesenberg, C. Kim, A. Zozulya, W. Lu, R. Shayduk, A. Madsen, and T. Salditt. In: *Journal of Synchrotron Radiation*, 28 (3):987–994, 2021. DOI: `10.1107/S1600577521003052`.
5. Observation of electron-induced characteristic x-ray and bremsstrahlung radiation from a waveguide cavity. M. Vassholz and T. Salditt. In: *Science Advances*, 7(4):eabd5677, 2021. DOI: `10.1126/sciadv.abd5677`.
6. Röntgenquelle mit strukturiertem Target zur gerichteten Emission in Wellenleitermoden. M. Vassholz and T. Salditt *Deutsches Patent- und Markenamt*, Patent No. DE10 2020 109 906.1 (pending), 2020.
7. Single-pulse phase-contrast imaging at free-electron lasers in the hard X-ray regime. J. Hagemann, M. Vassholz, H. Hoeppe, M. Osterhoff, J. M. Rosselló, R. Mettin, F. Seiboth, A. Schropp, J. Möller, J. Hallmann, C. Kim, M. Scholz, U. Boesenberg, R. Schaffer, A. Zozulya, W. Lu, R. Shayduk, A. Madsen,

C. G. Schroer, and T. Salditt. In: *Journal of Synchrotron Radiation*, 28(1), 2021. DOI: `10.1107/S160057752001557X`.

8. SPECTRAL μCT WITH AN ENERGY RESOLVING AND INTERPOLATING PIXEL DETECTOR. L. M. Lohse, M. Vassholz, M. Töpperwien, T. Jentschke, A. Bergamaschi, S. Chiriotti, and T. Salditt. In: *Optics Express*, 28(7):9842–9859, 2020. DOI: `10.1364/OE.385389`.
9. PROPAGATION-BASED PHASE-CONTRAST X-RAY TOMOGRAPHY OF COCHLEA USING A COMPACT SYNCHROTRON SOURCE. M. Töpperwien, R. Gradl, D. Keppeler, M. Vassholz, A. Meyer, R. Hessler, K. Achterhold, B. Gleich, M. Dierolf, F. Pfeiffer, T. Moser, and T. Salditt. In: *Scientific Reports*, 8(1):4922, 2018. DOI: `10.1038/s41598-018-23144-5`.
10. TOMOGRAPHY WITH EXTENDED SOURCES: THEORY, ERROR ESTIMATES, AND A RECONSTRUCTION ALGORITHM. L. M. Lohse, M. Vassholz, and T. Salditt. In: *Physical Review A*, 96(6):063804, 2017. DOI: `10.1103/PhysRevA.96.063804`.
11. TECHNIK ZUR TOMOGRAFISCHEN BILDERFASSUNG. T. Salditt, M. Vassholz, and B. Koberstein-Schwarz. *Deutsches Patent- und Markenamt*, Patent No. DE10 2015 215 323.1 (pending), 2017.
12. NEW X-RAY TOMOGRAPHY METHOD BASED ON THE 3D RADON TRANSFORM COMPATIBLE WITH ANISOTROPIC SOURCES. M. Vassholz, B. Koberstein-Schwarz, A. Ruhlandt, M. Krenkel, and T. Salditt. In: *Physical Review Letters*, 116(8):088101, 2016. DOI: `10.1103/PhysRevLett.116.088101`.
13. X-RAY OPTICS ON A CHIP: GUIDING X RAYS IN CURVED CHANNELS. T. Salditt, S. Hoffmann, M. Vassholz, J. Haber, M. Osterhoff, and J. Hilhorst. In: *Physical Review Letters*, 115(20):203902, 2015. DOI: `10.1103/PhysRevLett.115.203902`.
14. SEMI-TRANSPARENT CENTRAL STOP IN HIGH-RESOLUTION X-RAY PTYCHOGRAPHY USING KIRKPATRICK–BAEZ FOCUSING. R. N. Wilke, M. Vassholz, and T. Salditt. In: *Acta Crystallographica Section A: Foundations of Crystallography*, 69(5):490–497, 2013. DOI: `10.1107/S0108767313019612`.

Acknowledgements

Diese Arbeit wäre nicht möglich gewesen ohne die großartige Unterstützung vieler Personen. An dieser Stelle, sowie in den separaten Danksagungen am Ende der Kapitel 2, 3 und 4, möchte ich mich herzlichen bei all diesen Personen für ihre Hilfsbereitschaft und aufgewendete Zeit bedanken.

Zuallererst möchte ich mich ganz besonders bei Tim Salditt bedanken, durch den diese Arbeit erst möglich wurde. Seine Begeisterung und sein Vertrauen bildeten die Grundlage für viele neue Ideen und Konzepte, die mit seiner Unterstützung und umfangreichen Expertise erfolgreich ausgereift und umgesetzt werden konnten. Seine durchweg positive Einstellung motivierte stets experimentelle Hürden zu bewältigen.

Des Weiteren möchte ich mich herzlich bei Claus Ropers für die gute Co-Betreuung und die interessanten Diskussionen, sowie für die Bereitschaft zum Erstellen des Zweitgutachtens dieser Arbeit bedanken. Zudem bedanke ich mich bei Alexander Egner, Hans Hofsäss, Robert Mettin und Andreas Tilgner für die Beteiligung an meiner Prüfungskomission.

Bei meinen Kollegen Johannes Hagemann, Hannes Hoeppe, Sarah Hoffmann-Urlaub, Leon Lohse, Markus Osterhoff, Jakob Soltau und Mareike Töpperwien möchte ich mich sehr für die vielen fachlichen Diskussionen und die gute Zusammenarbeit bei gemeinsamen Projekten bedanken, die entscheidend zur Qualität dieser Arbeit beigetragen haben.

Zudem möchte ich mich bei Sarah Hoffmann-Urlaub für die Herstellung der Wellenleiterstruktur bedanken, sowie bei Mike Kanbach und Jochen Herbst für die Unterstützung bei der Probenpräparation.

Die Kavitationsexperimente wären nicht möglich gewesen ohne die langjährige und umfangreiche Expertise von Robert Mettin und Juan M. Rosselló für dessen Unterstützung und sehr gute Zusammenarbeit ich mich auch ganz besonders bedanken möchte.

Ebenfalls für die ausgezeichnete Zusammenarbeit bei den XFEL Experimenten und in der Planung im Vorfeld möchte ich mich bei Anders Madsen sowie dem gesamten MID Team bedanken.

Mein besonderer Dank gilt auch Jan Goemann und Markus Osterhoff für die großartige Arbeit an der IT Infrastruktur, ohne die das Lagern und Bezwingen der dutzenden Terabytes an Daten nicht möglich gewesen wäre.

Für die Unterstützung bei allen fein- und teilweise auch grobmechanischen Angelegenheiten möchte ich mich herzlich bei Bastian Hartmann, Peter Nieschalk und ganz besonders bei Peter Luley bedanken.

Für das kritische Lesen dieser Arbeit bedanke ich mich herzlich bei Jakob Soltau, Hannes Hoeppe, Johannes Hagemann, Markus Osterhoff, Karlo Komorowski, Leon Lohse, Jasmin Pape, Maria Kamper und Mareen Vaßholz.

Dem gesamten Institut für Röntgenphysik möchte ich für die ausgezeichnete Arbeitsatmosphäre und freundschaftliche Stimmung danken.

Zuletzt möchte ich mich ganz besonders bei meiner Familie bedanken, die mich immer unterstützt und mir stets zur Seite steht.